Investigation of nonlinear dynamics in and via femtosecond filaments in gases

Von der Fakultät für Mathematik und Physik
der Gottfried Wilhelm Leibniz Universität Hannover

zur Erlangung des akademischen Grades

Doktor der Naturwissenschaften
- Dr. rer. nat. -

genehmigte Dissertation von

M.Sc. Christoph Jusko

2022

Referent:	Prof. Dr. Milutin Kovačev
Korreferent:	Prof. Dr. Uwe Morgner
Korreferent:	Associate Prof. Dr. Cord L. Arnold
Tag der Promotion:	04.07.2022

Abstract

Christoph Jusko

Investigation of nonlinear dynamics in and via femtosecond filaments in gases

Intense, ultrashort laser pulses are required for the study of many nonlinear optical effects and are of utmost relevance for various applications from ultrafast X-ray radiography in medicine up to remote sensing of the atmosphere. Increasing their intensity while interacting with matter eventually leads to the generation of laser-induced plasma. This plasma has fascinating optical properties such as a negative refractive index contribution proportional to the free electron density or the lack of a damage threshold, giving the prospect of a multitude of new applications based on the manipulation of light with plasma. The realization of such plasma-based applications requires a precise knowledge of its properties and temporal evolution, as the plasma remains for much longer than its generation event. A method to generate and investigate ultrashort laser pulses as well as laser-induced plasma is femtosecond filamentation. It represents the formation of an intense self-guided light channel in a medium for distances much longer than the Rayleigh range of the same beam focused in vacuum. It is formed by a dynamic balance of Kerr-induced self-focusing and plasma-induced defocusing. In this thesis, it is demonstrated that femtosecond filamentation can be employed as a tool to investigate the temporal evolution of laser-induced plasma. The study is realized in various atomic and molecular gas atmospheres via measuring the temporal evolution of the enhancement of third harmonic radiation generated by a femtosecond filament which is intercepted by a laser-induced plasma spot. Significant differences for the lifetime of the plasma in atomic and molecular gas atmospheres are found. Further, a novel method for the complete spatio-temporal characterization of a femtosecond filament along its length is presented. It is based on controlled filament termination at various positions along its length in combination with spatio-temporal pulse characterization and numerical backpropagation of the filament pulses to the termination point. The capabilities of the method are illustrated by revealing complex spatio-temporal dynamics and couplings during filament propagation.

Key words: femtosecond filamentation, laser-induced plasma, plasma lifetime, filament pulse characterization

Contents

Acronyms and symbols

Acronyms

Notation	Description
ADK	Ammosov-Delone-Krainov
ATI	above-threshold ionization
BBO	beta barium borate
CCD	charge-coupled device
CPA	chirped pulse amplification
d-scan	dispersion scan
DCMs	double-chirped mirrors
DFG	difference frequency generation
EEDF	electron energy distribution function
ELI	Extreme Light Infrastructure
FFT	fast Fourier transform
FROG	frequency-resolved optical gating
FTS	Fourier transform spectroscopy
FWHM	full width at half maximum
GD	group delay
GDD	group delay dispersion
HHG	high-order harmonic generation

Notation	Description
IAPs	isolated attosecond pulses
LIDAR	light detection and ranging
MIR	mid-infrared radiation
MPI	multi-photon ionization
ND	neutral density
NEE	Nonlinear Envelope Equation
NIR	near-infrared radiation
NLSE	Nonlinear Schrödinger Equation
OAP	off-axis paraboloid
OPCPA	optical parametric chirped pulse amplification
PG	polarization-gate
PPT	Peremolov-Popov-Terent'ev
RHHG	relativistic high-order harmonic generation
SD	self-diffraction
SFG	sum frequency generation
SHG	second harmonic generation
SIGC	semi-infinite gas cell
SNR	signal-to-noise ratio

Notation	Description
SPM	self-phase modulation
SRFTS	spatially resolved Fourier transform spectrometry
SRSI	self-referenced spectral interferometry
STCs	spatio-temporal couplings
STFT	short-time Fourier transform
SVEA	slowly varying envelope approximation
TBC	two-beam coupling
TG	transient-grating
TH	third harmonic
THG	third harmonic generation
TI	tunnel ionization
TOD	third-order dispersion
TS	Thomson scattering
UPPE	unidirectional pulse propagation equation
UV	ultra violet
XPW	crossed-polarized wave
XUV	extreme ultra violet
YI	Yudin and Ivanov

Symbols

Notation	Description
A	heavy particle
A^*	excited heavy particle
A^+	positively charged ion
A_{cross}	cross correlation signal term of the SRFTS method
a_0	Bohr radius
β	fraction of incident beam for the reference
c	speed of light
c_{3body}	rate factor of three-body electron-ion collisions
D	dispersion operator
D_{beam}	collimated beam diameter
d	relative filament position
E	scalar electric field
$\boldsymbol{E}$	vectorial electric field
E'	reference corrected electric field
E^*	complex conjugated electric field
E_{at}	atomic field strength
E_{av}	average electron energy
E_{in}	incident pulse energy

Notation	Description
E_{kin}	kinetic energy
E_{out}	output pulse energy
E_{pulse}	incident pulse energy
E_{ref}	reference electric field
E_{TF}	spectrogram in the time-frequency analysis
E_{tot}	total free electron energy
$\boldsymbol{\mathcal{E}}$	vectorial electric field
e	mathematical constant
e_{c}	elementary charge
e^{-}	electron
ε_0	vacuum permittivity
$\mathcal{FT}$	Fourier transform
f	focal length
ϕ	phase
ϕ_{mirror}	mirror curvature phase
ϕ_{ref}	phase of the reference electric field
ϕ_{SPM}	phase contribution by self-phase modulation
$\Delta\phi_{\mathrm{disp}}$	wedge phase contribution

Notation	Description
$\Delta\phi_\mathrm{p}$	plasma phase contribution
G	sliding window function
γ	Keldysh parameter
h	Planck constant
I	intensity
I_at	required intensity for the atomic field strength
I_clamp	clamping intensity
I_p	ionization potential
i	imaginary number
K	number of photons
K_disp	wavenumber including dispersion
K_z	Fourier optics plane wave propagator
k	wavenumber
$\boldsymbol{k}$	wave vector
k_0	central wavenumber
k_B	Boltzmann constant
k_x	Reciprocal coordinate perpendicular to the propagation direction
k_y	Reciprocal coordinate perpendicular to the propagation direction

Notation	Description
L_{c}	nonlinear focal length
$L_{\mathrm{c,f}}$	effective nonlinear focal length
λ_0	central wavelength
λ_c	central wavelength
M	molar mass
m_{e}	electron mass
μ	minimization parameter
N_{A}	Avogadro constant
N_{crit}	critical free electron density
N_{e}	free electron density
N_{nt}	number density
N_{pixel}	required amount of pixels for interference pattern recording
n	refractive index
n_0	linear refractive index
n_2	nonlinear refractive index
Δn_{Kerr}	nonlinear refractive index contribution
n_{p}	refractive index of plasma
Δn_{p}	refractive index change due to plasma

Notation	Description
η	scaling parameter
P	scalar polarization
$\boldsymbol{P}$	vectorial polarization
P_{crit}	critical peak power
P_{L}	linear polarization
P_{NL}	nonlinear polarization
P_{peak}	peak power
p	pressure
p_{pixel}	required amount of pixels for fringe resolvement at the beam edge
ρ_{m}	mass density
π	mathematical constant
r	spatial coordinate perpendicular to the propagation direction
$\boldsymbol{r}$	spatial coordinate vector perpendicular to the propagation direction
S	spectral density function
S_{meas}	measured d-scan trace
S_{sim}	simulated d-scan trace
σ_0	geometrical atomic cross section

Notation	Description
σ_{K}	absorption cross section for K photons
T	space-time focusing operator
T_{e}	free electron temperature
T_{p}	moving time frame of the optical pulse
t	temporal coordinate
τ_{p}	pulse duration
θ_{con}	cone angle
U_{p}	ponderomotive potential
v	probability
v_{g}	group velocity
v_{ph}	phase velocity
W	probability
W_{MPI}	multi-photon ionization rate
w_0	waist radius
ω	angular frequency
ω_0	central angular frequency
ω_{L}	angular laser frequency
ω_{p}	plasma frequency

Notation	Description
$\Delta\omega$	induced angular frequency contribution
$\Delta\omega_\mathrm{p}$	induced angular frequency contribution of plasma
x	Cartesian coordinate perpendicular to the propagation direction
x_c	Beam center along the Cartesian coordinate x
χ	susceptibility
y	Cartesian coordinate perpendicular to the propagation direction
y_c	Beam center along the Cartesian coordinate y
z	Cartesian coordinate in propagation direction
z_crit	critical length
z_R	Rayleigh range/length
z_ter	Filament termination position
Δz	propagated distance

CHAPTER 1

Introduction

Since the development of lasers in the 1960's, pulsed lasers have enabled the study of nonlinear light-matter interaction due to their achievable high intensity as well as the study of ultrafast processes up to the attosecond regime ($1\,\mathrm{as} = 10^{-18}\,\mathrm{s}$) due to their short duration [Bra00; Cor07; Kra09]. By applying pump-probe schemes, fundamental physical processes and concepts can be studied with a temporal resolution in the range of the applied pulsed laser's duration [Sto92; Hen01; Lea10]. The femtosecond-resolved pump-probe spectroscopy studies of chemical reactions, called "femtochemistry", led by Ahmed Zewail [Zew00], were rewarded with the Noble Prize in Chemistry in 1999. Via the development of sophisticated amplification concepts such as the Noble-Prize-awarded chirped pulse amplification (CPA) [Str85; Mai88] or optical parametric chirped pulse amplification (OPCPA) [Dub92; Ros97] techniques, the achievable peak power of pulsed laser systems could be continuously increased over the last decades. Peak powers of GW [Hen00; Rot09] to TW [Tak06; Her09] are reached in present-day table-top laboratory systems and even up to PW in large-scale facilities such as the Extreme Light Infrastructure (ELI) [Wil20], with pulse durations in the fs-regime. In this way, extremely high intensities of $10^{18}\,\mathrm{W/cm^2}$ up to $10^{23}\,\mathrm{W/cm^2}$ can be achieved [Hen00; Yam02; Dor20]. With such intensity levels, many nonlinear process can be driven efficiently until, for high enough intensities, ionization of the respective medium takes place, leading to the generation of laser-induced plasma, i.e. free charges. With intensities above 10^{13}-$10^{14}\,\mathrm{W/cm^2}$, in combination with pulse durations in the fs-range, practically only gaseous media can be studied, as dense media already ionize [Gam02]. The generation of free electrons in femtosecond laser-induced plasma, via the processes of multi-photon ionization (MPI)

or tunnel ionization (TI), counteracts nonlinear processes such as self-focusing, that would otherwise continuously increase the intensity in the focus of an intense laser beam, by leading to plasma absorption and plasma defocusing. Plasma defocusing is based on the presence of free electrons that alter the refractive index of the medium: the higher the free electron density, the lower is the refractive index of the medium. Controlling the spatial distribution and the amount of the free electron density paves the way for "plasma photonics", the manipulation of light with plasma. Due to the fact that plasma is based on ionized matter, it has a unique property for the realization of optics: it has no damage threshold. Hence, it is well suited to be used for beam manipulation in environments with very high light intensities of the order of TW/cm^2 or higher, making it also an ideal candidate for the development of future laser systems. Schemes for plasma-based lenses [Kat09], gratings [Liu10; Dur11], holograms [Leb17], waveplates based on plasma gratings [Mic14; Tur16] and mirrors [Kap91; Dro04] were already realized, leading to applications such as the generation of relativistic high-order harmonic generation (RHHG) [Edw14; Edw20], a potential tool towards very bright extreme ultraviolet radiation sources. Further, laser-induced plasma forms the basis of laser-based accelerator schemes [Taj79; Esa09; Fau18] and can be used for broadening pulse spectra [Fou10; Aug12], generate new frequencies up to intense mid-infrared radiation [Nie18] or enhance existing radiation [Har08]. From the moment of its creation, laser-induced plasma inherently is a transient phenomenon. Its constituents of opposite charge, negatively charged free electrons and positively charged ions, have the tendency to form neutral matter via recombination processes eventually. Therefore, it is fundamentally important to know the characteristic decay time of the plasma of interest, also referred to as "plasma lifetime". This knowledge can improve many applications in which a temporally delayed beam interacts with the laser-induced plasma, e.g. in the case of plasma gratings in which an incident beam shall be diffracted from laser-induced grating structure consisting of plasma.

A fundamental nonlinear propagation phenomenon that combines nonlinear processes such as self-focusing and laser-induced ionization, is femtosecond filamentation [Bra95; Cou07]. It describes the formation of an intense light channel in gaseous or dense media for distances much longer than the Rayleigh range of the same laser pulse

focused in vacuum. It is formed by a dynamic balance between the aforementioned self-focusing due to the Kerr effect, a nonlinear effect of third order, defocusing due to usual beam diffraction and laser-induced ionization of the medium, leaving a weakly ionized plasma column in its wake. Filament lengths between millimeters [Yua13] up to hundreds of meters [Fon99a; Béj07; Dur13] were realized. Due to the high intensity in the center or "core" of the filament, about $50\,\mathrm{TW/cm^2}$ for a femtosecond filament in air [Kas00], many nonlinear effects such as the generation of the third harmonic (TH) of the fundamental driving field are induced along its length [Sun09; Liu11]. Due to their combination of high intensities with laser-induced ionization, femtosecond filaments cover a wide range of applications such as atmospheric light detection and ranging (LIDAR) techniques by white-light continuum [Rai00; Kas03], guiding of electric discharges in laboratory [Tzo01b] and atmospheric environments [Kas08], generation of down to sub-1.5-cycle pulses [Ste12] or the generation of new frequencies such as THz-radiation [DAm07; DAm08], the aforementioned TH radiation [Liu19] or high-order harmonics [Ste11b]. Furthermore, their intrinsic dynamic balance of nonlinear focusing and defocusing effects makes them a key candidate for the investigation of nonlinear pulse propagation phenomena. Filaments are fascinating as, on the one hand, they are a tool to study nonlinear effects and laser-induced plasma and, on the other hand, they can be utilized for applications based on their intrinsic nonlinear effects. For instance, high order harmonics can be generated directly from a filament [Ste11b], without the need of a capillary [Run98], gas cell [Tak02], semi-infinite gas cell (SIGC) [Pap01; Ste09a; App21] or gas jet [Sal97]. Further, ultrashort pulses can be generated directly from a filament [Ste12], instead of employing gas-filled hollow-core fibers [Nis96; Böh14], multi-plates [Lu14; Che16] or multi-pass cells [Sch16; Bal20] for that purpose. However, due to the interplay of the nonlinear effects in a filament, spatio-temporal couplings (STCs), acting on the filament pulse properties in a non-trivial way, occur [Fac05]. Therefore, filaments need to be completely, i.e. in terms of amplitude and phase, and spatio-temporally characterized so that the pulse properties can be tailored for any application.

1.1 Motivation for the present work

This work targets on showing the potential of femtosecond filaments as a tool to study nonlinear effects by the example of direct plasma lifetime studies in various gases via third harmonic enhancement as well as providing a new method for the investigation of nonlinear propagation effects in filamentation itself, able to resolve complex STCs, via a complete spatio-temporal characterization along its length. Furthermore, this work aims at revealing that there is still plenty of potential at deepening the understanding and control of femtosecond filaments, thereby expanding their application range, as well as expanding the fundamental knowledge about the temporal evolution of femtosecond laser-induced plasma for the improvement and expansion of methods in the field of plasma optics.

To the best of the author's knowledge, existing methods for the determination of femtosecond laser-induced plasma lifetimes are all indirect, requiring certain assumptions or additional measurements before the temporal decay of the plasma can be determined. The method presented in this work, based on filament-assisted TH enhancement, is the first method that enables a direct analysis of the temporal plasma evolution by studying the temporal evolution of the enhancement of TH radiation from a filament by laser-induced plasma. Previous works have shown, that the TH from a filament can be enhanced, whenever the filament core is disturbed by an obstacle [Akö02; Liu15]. When the obstacle is formed by laser-induced plasma, the temporal evolution of the TH enhancement maps the temporal evolution of the plasma [Sun09; Sun10]. In this work, plasma lifetime studies in atomic gas plasmas (helium, argon and xenon), in molecular gas plasmas (nitrogen and carbon dioxide), and in the mostly molecular gas plasma of air, are shown. Possible parameter dependencies of the laser-induced plasma are investigated and characteristic differences between the plasma lifetimes of atomic and molecular gas plasmas as well as differences in between the decays of plasmas of atomic or molecular gases are analyzed and discussed.

In this work, to the best of the author's knowledge, the first complete spatio-temporal pulse characterization of a femtosecond filament along its length is realized, by providing a new comprehensive method for femtosecond filamentation analysis.

The method is based on defined termination of a filament at different lengths, a complete spatio-temporal characterization with a combination of spatially resolved Fourier transform spectrometry (SRFTS) [Mir14; Gal14] and the dispersion scan (d-scan) technique [Mir12a; Mir12b], and a numerical backpropagation of the characterized pulses to the termination point. Measurement results, revealing STCs and nonlinear effects in the filament are presented and analyzed, demonstrating the potential of the method for filamentation analysis and paving the way for a precise tailoring of filaments pulses for any application of interest.

This thesis is structured into four parts. In Chapter 2, the fundamentals about laser filamentation, the basic concepts of nonlinear optics, ionization and recombination as well as key properties of laser-induced plasma, STCs, and the used pulse characterization techniques are introduced. These concepts are required to understand the presented experiments in the following two chapters. In Chapter 3, the experiment about the determination of plasma lifetimes via TH enhancement in various gas plasmas is presented and the results are analyzed and discussed. In Chapter 4, the new complete spatio-temporal characterization of a femtosecond filament along its length is displayed and its capabilities on revealing complex nonlinear propagation, via a four-dimensional tracing of nonlinear propagation dynamics, are demonstrated in one-, two- and three-dimensional pulse representations. In the final Chapter 5, this work is summarized and an outlook on further potential investigations is given.

CHAPTER 2

Fundamentals

In this chapter, the fundamentals, necessary for the understanding of the experiments presented in this thesis, are provided. At the beginning, a description of laser filamentation is given, followed by a basic introduction into nonlinear optics effects, such as Kerr effect and self-phase modulation, as well as into the theory of laser-induced plasma. Subsequently, filamentation models are described. All these basics support the understanding of femtosecond filamentation, which is the central topic of this thesis. A special focus is given to third-harmonic generation in filaments as well as to the enhancement of that radiation. The last section then introduces methods for the spatio-temporal as well as the pure temporal characterization of femtosecond laser pulses.

2.1 Laser filamentation

Laser filamentation is a nonlinear optical phenomenon in which a beam propagates with high intensity for much longer than the Rayleigh length of the same beam focused in vacuum without any external guiding mechanism, while creating a thin plasma channel along its propagation path. The focused light channel is formed by a dynamic balance of the nonlinear focusing and defocusing effects "self-focusing" due to the Kerr effect and "plasma-induced defocusing", being described in more detail in Sec. 2.2.1 and Sec. 2.3.1 later in this chapter. A schematic view of laser filamentation is shown in Fig. 2.1. The laser beam self-focuses until it ionizes the medium which leads to plasma-induced defocusing. Several such focusing-defocusing cycles can take place subsequently during laser filamentation, forming the intense and focused light channel that is called filament. More details on the filamentation dynamics are given in Sec. 2.4.

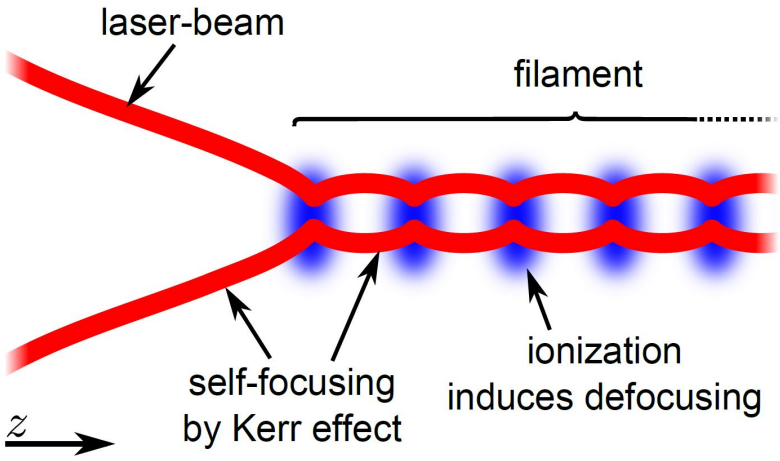

Figure 2.1: Schematic view of laser filamentation, showing self-focusing of the laser beam due to the Kerr and subsequent plasma-induced defocusing. Several such focusing-defocusing cycles can take place, forming the filament. Reprinted from [Ste11a].

Filamentation exists in solids, liquids, and gases [Cou07] with propagation lengths reaching from a few mm [Yua13] up to several hundreds of m [Fon99a; Béj07; Dur13], generated from laser beams with pulse energies from hundreds of nJ [Liu03] up to several Joule [Béj07; Toc19] and pulse durations from sub-10 fs [Mat18] up to ps [Toc19]. Hence, laser filamentation covers a broad parameter space with numerous intrinsic nonlinear effects.

While filamentation exists in all states of matter with very different propagation lengths, generated from laser beams with a broad range of pulse parameters, the basic concept always remains the same. This principle also applies to spatial profile of a filament, presented in more detail in the following.

2.1.1 Spatial profile of the filament

The spatial profile of the filament consists of three different elements which are, from the center to the outer edge: the core, the reservoir and the conical emission. They are presented in more detail in the following. An illustration of the different spatial segments is shown in Fig. 2.2.

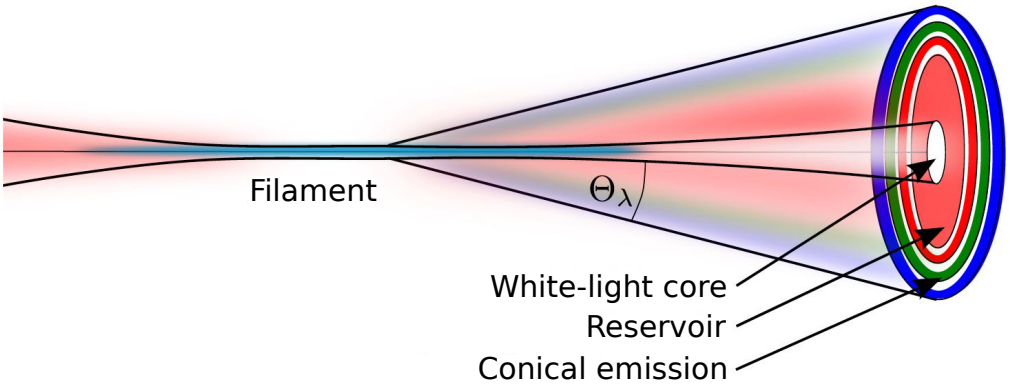

Figure 2.2: Schematic representation of the spatial profile of a femtosecond filament. The center is formed by the white-light core, surrounded by the reservoir. The conical emission is emitted as a cone of colored rings around the reservoir with different angles Θ_λ for the individual wavelengths of the filament spectrum. Adapted from [Sch12].

The core

In the center of the filament is the core. Typically, it has a diameter of about 55 - 100 µm, for a filament in air [Thé06], depending on the external focusing conditions and the pressure. In liquid water the core diameter was measured to be roughly 60 µm [Dub03] and in fused silica the core diameter is in between 10 to 40 µm [Tzo01c]. Note that for very loose focusing conditions core diameters up to the mm range were observed for air [Fon99a; Chi02; Méc04]. However, such large diameters comprise a special filamentation regime in which the ionization threshold is not reached and balance between focusing and defocusing is only given by the Kerr effect and beam diffraction. The core inhibits all the nonlinear dynamics and the high intensities of TW/cm^2, mentioned earlier. Whereas the core diameter is slightly different for filaments in the three different states of matter, the clamping intensity is similar for gases and solids [Kas00; Cou07], i.e. the clamping intensity for glass is around 50 TW/cm^2 [Sme12], equal to the clamping intensity of air [Kas00]. Similar clamping intensities in gases and solids originate from the balance between the Kerr-induced self-focusing with the plasma-induced defocusing and natural beam diffraction. In solids, the particle density N_{nt} is roughly three orders of magnitude higher than the particle density of gases at ambient pressure and room temperature. This higher

density directly leads, in a linear dependence, to a higher free electron density N_e, thus a denser plasma (see Sec. 2.3.1). However, also the nonlinear refractive indices of solids are much higher than in gases, leading to stronger self-focusing. The much stronger plasma defocusing balances the significantly stronger self-focusing, resulting in a similar clamping intensity in gases and solids. The same principle, applies for the clamping intensity in liquids with free electron densities and nonlinear refractive indices in between gases and solids. A denser plasma is also connected to stronger plasma absorption, though, which leads to very short filaments of only a few cm in solids [Phi05] compared to lengths of several 10^2 m for gas filaments (see Sec. 2.1)). The core has a self-cleaning property, meaning an arbitrary beam profile during the onset of filamentation is becoming more similar to a Gaussian ground mode during propagation. This property is related to the spatio-temporal focusing behaviour of the filament. The Kerr-induced self-focusing and the plasma-induced focusing are stronger for higher pulse intensities and therefore favour Gaussian spatial pulse shapes which have better focusing properties than non-Gaussian beam shapes, suppressing non-intense parts of the pulse that are diffracted out of the pulse.

The reservoir

The reservoir is a ring with a diameter of 5 - 10 times the core diameter [Liu05a] that is comparable in size to the incident beam during the onset of filamentation, sometimes even exceeding the initial beam diameter [Cou07]. The reservoir is the energy storage of the filament since it contains around 50 % of its total energy (see Sec. 2.4.2). Whereas a filament can continue to propagate when the core of the filament is disturbed or blocked (see Sec. 2.1.2), the filament is immediately terminated when the reservoir is blocked [Bro97; Liu05a; Liu05b]. The reservoir is in a dynamic interaction with the core, supplying it with energy. Around the reservoir is a wavelength-dependent radiation called “conical emission” that is explained in the following.

Conical emission

The conical emission surrounds the reservoir and the core, forming a cone of rings with a characteristic angles θ_{con} for every color in the cone spectrum. The relationship

between the angle and the color for the conicial emission is inversely to normal beam diffraction: red light has the smallest angle, whereas blue light the biggest angle. The origin of the conical emission is not completely understood yet and different explanations exist [Cou07]. One explanation is the appearance of a Cherenkov process in the filament [Gol90; Nib96]. In this explanation, the different angles for different colours are explained by $\cos(\theta_{\mathrm{con}}) = v_{\mathrm{ph}}/v_{\mathrm{g}}$ with the different ratios between their phase and group velocity. Other explanations are based on X-waves [Con03; Tra03; Fac06], plasma-induced broadening [Blo73; Kos97], or four-wave mixing [Xin93; Lut94; Thé08]. Fig. 2.3 shows a measurement of the spatial profile of a femtosecond filament in argon atmosphere, presented in [Sch12].

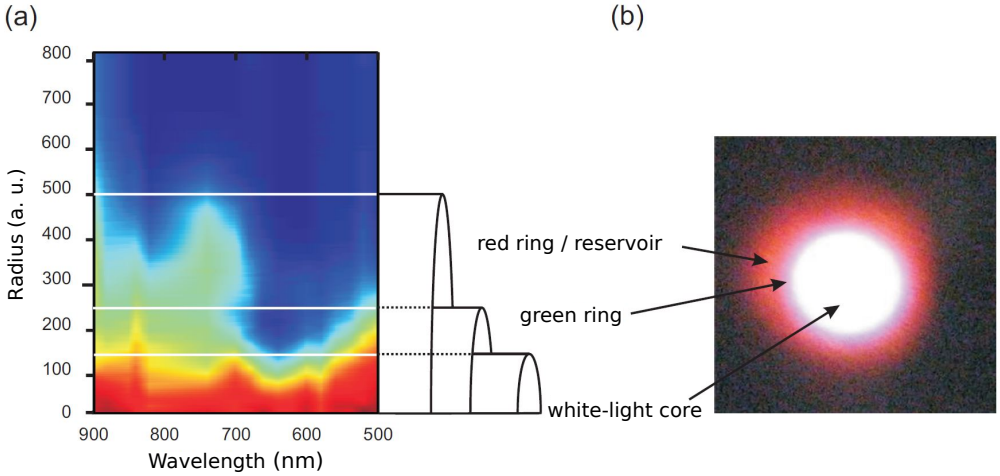

Figure 2.3: Spatial profile of a femtosecond filament in argon atmosphere. (a) spectral distribution as a function of the beam radius. The spectra are normalized for each wavelength and smoothed along the wavelength axis. The radii for the filament core and the surrounding ring structure formed by the conical emission and the reservoir are marked by horizontal white lines. (b) image of the corresponding beam profile of the filament taken after the end of the filament with labels for the different spatial elements. Adapted from [Sch12].

In the following, the effects of self-healing and self-cleaning are briefly described. They are both caused by a dynamic interaction of the filament core and the reservoir.

2.1.2 Self-healing and self-cleaning

Interestingly, a filament can self-reconstruct, if the core is blocked by any obstacle. The phenomenon has been observed first for gas filaments propagating through

water droplets in a fog chamber [Cour03], as well as for water filaments blocked by solid beam stopper [Dub04a; Dub04b]. This effect can be explained by the dynamical interaction of the filament core with the reservoir. The reservoir sustains and resupplies the core with energy before and after the obstacle. According to [Dub04a], multiphoton absorption plays a key role in the filament propagation and beam reshaping. Due to the plasma-induced nonlinear losses in the core during propagation, the pulse in the filament receives a conical component, shaping it into a more Bessel-like beam. This Bessel shape connects the beam in the core to the reservoir. From the reservoir, it can self-reconstruct into the core via self-focusing due to the Kerr effect. The universal self-reconstruction property of a filament makes it a very interesting tool for atmospheric applications such as remote sensing applications like LIDAR, where the beam can be disturbed by water droplets, ice crystals, or aeorosols. Due to the self-healing property, the propagation of the beam can be assured over long distances despite a lot of possible disturbances by microparticles in between.

Closely connected to the pulse dynamics leading to the self-healing phenomenon is the effect of self-cleaning, self-spatial mode filtering, or spatial mode cleaning [Liu07; Chi07; Akt07]. It describes the effect of a significant improvement of beam quality for an optical pulse undergoing filamentation and is very interesting for any application requiring a very clean beam profile in combination with a high intensity.

So far, single filaments were described which can exist for a broad range of laser beam parameters. However, i.e. the pulse energy cannot be increased limitlessly to remain in that regime. Above a certain threshold, the filament breaks up into a manifold structure consisting of many single filaments. This phenomenon is called multifilamentation and is described briefly in the following.

2.1.3 Multifilamentation

If the peak power of the filament driving pulse strongly exceeds the critical peak power P_{crit}, described in more detail in Sec. 2.2.1, the single filament breaks up into multiple hot spots forming multiple single filaments and one enters the regime of multifilamentation [Ber04; Méc04; Fib04]. Every single filament in the multifilamentation regime has a peak power which is roughly 2.5 times the critical peak power

[Bes66; Ber03; Ber04]. The multifilamentation regime is chaotic, i.e. it cannot be predicted where in the spatial profile the filament channels will be formed. Further, the channels are prone to slightest modulations of the spatial distribution of the beam intensity leading to channel break-up which creates a constantly changing pattern of multiple filaments. Multifilamentation can be avoided by reducing the peak power of the driving laser pulse and cleaning its beam profile.

The last filament property that is introduced in this section, is its scaling invariance to the beam input parameters and filamentation parameters. The description of scaling invariance is based on [Zho14; Hey16].

2.1.4 Scale invariance of filaments

Many nonlinear optical effects are scale-invariant, that means by carefully upscaling or downscaling certain parameters or dimensions the scalable nonlinear effect can take place in the same way. This principle even applies to highly complex nonlinear phenomena such as HHG and filamentation in gases. In order to introduce the principle of scale invariance, one needs to introduce a dimensionless scaling parameter η. Filamentation in gases is scale-invariant to the Gaussian beam parameters z_R and w_0 with the scaling $z_\mathrm{R} \to \eta^2 z_\mathrm{R}$ and $w_0 \to \eta w_0$ and the incident pulse energy E_pulse with $E_\mathrm{pulse} \to \eta^2 E_\mathrm{pulse}$ whereas it is scale-invariant to the gas pressure p with $p \to p/\eta^2$. This scaling means, e.g. if one tunes the energy of the pulse up by η the filamentation properties will stay the same if also the beam size is scaled by $\sqrt{\eta}$ and the pressure by $1/\eta$. Furthermore, filamentation's scale-invariant nature allows to rescale also the output parameters P_crit (the critical peak power) and z_crit, the critical length after which an initially collimated beam would collapse due to self-focusing, with the scaling $P_\mathrm{crit} \to \eta^2 P_\mathrm{crit}$ and $z_\mathrm{crit} \to \eta^2 z_\mathrm{crit}$. Furthermore, the output pulse energy E_out can be rescaled with $E_\mathrm{out} \to \eta^2 E_\mathrm{out}$. The rescaling relations to these output parameters imply that, e.g. when the input pulse energy is increased by η, while keeping all other parameters constant, the filament will react to this higher input power by scaling up the length of the filament (proportional to z_crit) and the output power by η. In that way the filament propagation dynamics remain the same for all pulse energies. The very fundamental principle of scale invariance for gas filaments is fascinating, underlining the universality of this complex nonlinear

propagation phenomenon. It shows that filamentation can be realized on a small scale with high repetition laser sources with low pulse energies in the µJ as well as on high-power laser systems in the J range.

The introduction into the scale invariance of filaments completes the introduction into femtosecond filamentation, the major keystone of this thesis, being part of all presented experiments. In the following, the basics of nonlinear optics and laser-induced plasma are introduced. The nonlinear optical processes and laser-induced plasma presented in Sec 2.2 and Sec. 2.3 are fundamental for the understanding of laser filamentation and its complex pulse propagation dynamics and effects described in Sec. 2.4.

2.2 Basics of nonlinear optics

In linear optics, the interaction of a (vectorial) light field $\boldsymbol{E}(\omega)$, dependent on the angular frequency ω, with matter can be described via the polarization density $\boldsymbol{P}(\omega)$ of the medium:

$$\boldsymbol{P}(\omega) = \varepsilon_0 \chi^{(1)}(\omega) \boldsymbol{E}(\omega), \tag{2.1}$$

with ε_0 the dielectric constant and $\chi^{(1)}(\omega)$ the first-order susceptibility. The polarization describes the resulting dipole moment that is created between the positive center of charge and the negative center of charge due to the displacement of the electrons from the equilibrium position by the incident light field. If the incident light field is relatively weak, the displacement of the electrons depends linearly on the field strength with the proportionality factor $\chi^{(1)}$. Throughout the thesis, only linearly polarized light is considered, since that is the polarization of the light sources used for the experiments described in Chapter 3 and Chapter 4. Hence, in the following only the scalar representations of $\boldsymbol{P}(\omega)$ and $\boldsymbol{E}(\omega)$, $P(\omega)$ and $E(\omega)$, are being used. The linear susceptibility is connected with the linear refractive index $n_0(\omega)$ via:

$$\chi^{(1)}(\omega) = n_0^2(\omega) - 1 \tag{2.2}$$

which shows that when the susceptibility is frequency-dependent, the material is dispersive. If the strength of the incident light field increases, the displacement of the

electrons becomes very large and shows a nonlinear dependence on the field strength so that Eq. 2.1 is not valid anymore. The susceptibility $\chi(\omega)$ needs to be expanded in a pertubative approach by applying higher-order terms via a Taylor series around $E = 0$ which describe the nonlinear behaviour of the medium with respect to the field strength:

$$P(\omega) = \varepsilon_0 \left[\chi^{(1)}(\omega)E(\omega) + \chi^{(2)}(\omega)E^2(\omega) + \chi^{(3)}(\omega)E^3(\omega) + \cdots\right] \tag{2.3}$$

with the terms $\chi^{(n>1)}(\omega)$ describing the nonlinear dependency of the medium with respect to an intense light field. Hence, Eq. 2.3 can also be expressed as $P(\omega_0) = P_{\mathrm{L}}(\omega) + P_{\mathrm{NL}}(\omega)$ with $P_{\mathrm{L}}(\omega)$ containing the linear polarization and $P_{\mathrm{NL}}(\omega)$ containing all nonlinear polarization contributions with $\chi^{(n>1)}(\omega)$. The lowest nonlinear susceptibility, the second order susceptibility $\chi^{(2)}(\omega)$, is related to nonlinear effects such as second harmonic generation (SHG), sum frequency generation (SFG) and difference frequency generation (DFG) or the electro-optic effect [Boy08]. In centrosymmetric media, such as the atomic noble gases, air, nitrogen (N_2) and carbon dioxide, even orders of the nonlinear susceptibilities $\chi^{(n>1)}(\omega)$ vanish and only the uneven orders remain [Boy08]. Hence, the lowest-order nonlinear susceptibility in centrosymmetric media is the third-order $\chi^{(3)}(\omega)$, that is related to many nonlinear effects such as self-phase modulation (SPM), third harmonic generation (THG) and self-focusing. The higher the order of a nonlinear effect, the higher needs to be the intensity of the light field to significantly drive it. Therefore, the third-order effects are the most relevant nonlinear effects in centrosymmetric media. SPM and self-focusing are connected via the so-called “Kerr effect”, described in the following, and play a crucial role in femtosecond filamentation.

2.2.1 Kerr effect

Analog to the linear polarization of a medium, the Kerr effect describes the expansion of the refractive index $n_0(\omega)$ with an intensity-dependent nonlinear refractive contribution Δn_{Kerr} for intense incident light fields (omitting the frequency dependency):

$$n(\boldsymbol{r},t) = n_0 + \Delta n_{\mathrm{Kerr}} = n_0 + n_2 I(\boldsymbol{r},t), \tag{2.4}$$

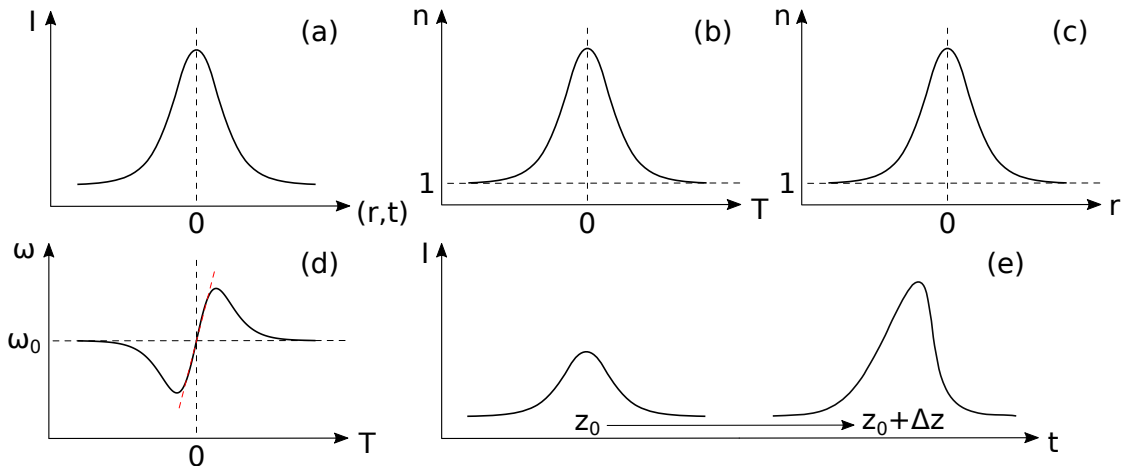

Figure 2.4: Effects of the Kerr effect, induced by an intense laser pulse. (a) intensity profile of the optical pulse in space and time with a peak power around the critical peak P_{crit} for self-focusing. (b) Kerr-induced temporal refractive index profile in a moving time frame $T_{\text{p}} = t - z/v_{\text{g}}$ with the optical pulse, with the linear refractive index $n_0 \approx 1$ for a gaseous medium (horizontal dashed line). (c) Kerr-induced refractive index profile along the transversal beam axis. (d) Kerr-induced self-phase modulation (SPM) leading to a change of the instantaneous frequency around the central frequency ω_0 of the pulse, adding new frequencies to the optical pulse. Around the peak of the pulse the frequency change is approximately linear (red dashed line). (e) after a propagation distance Δz in the Kerr medium, the Kerr effect leads to an increase of the intensity and to self-steepening of the optical pulse where the trailing part catches up with the leading part creating an asymmetric pulse profile with a steep pulse edge.

with $I(\boldsymbol{r},t)$ denoting the intensity of the incident light field in space and time and n_2 being the nonlinear refractive index. This nonlinear factor depends on the third order susceptibility as:

$$n_2 = \frac{3\chi^{(3)}}{4n_0^2\varepsilon_0 c}. \tag{2.5}$$

In gases, the Kerr nonlinearity $\chi^{(3)}(\omega)$ is proportional to the pressure [Chi10] and inversely proportional to the temperature of the medium [Boy08], making the nonlinear refractive index a conveniently tunable variable. Since the intensity of the light field has a spatial and a temporal dependency, a direct consequence is that also the refractive index is dependent on the spatial and temporal properties of the beam. If one assumes a Gaussian distribution in space and time of the incident beam, which

are valid approximations for an ultrashort laser pulse, the refractive index follows this distribution as well, which means that the refractive index is the highest in the center of the beam and decreases rapidly towards the edges. This index distribution acts like a focusing lens, since the phase velocity of the wavefronts in the center of the beam is smaller than at the edges. If the peak power of the beam equals or exceeds the critical peak power P_{crit} [Mar75]:

$$P_{\mathrm{crit}} = \frac{3.77\pi c^2}{2n_0 n_2 \omega_0^2}, \tag{2.6}$$

with ω_0 representing the central angular frequency of the optical field, i.e. the angular carrier frequency, c being the speed of light in vacuum and 3.77 a factor which takes into account the Gaussian distribution of the beam [Cou07], the focusing of the beam due to the Kerr effect overcomes its natural diffraction and the beam self-focuses. Self-focusing decreases the beam diameter, which leads to a higher beam intensity, hence increasing again the refractive index. The increased refractive index causes an additional increase of the self-focusing. Thus, self-focusing is a self-enhancing effect, that theoretically would lead to a beam that focuses into a singularity in space after a length L_c given by this semi-empirical equation [Mar68; Mar75]:

$$L_c = \frac{0.367 z_{\mathrm{R}}}{\left(\sqrt{P_{\mathrm{peak}}/P_{\mathrm{crit}}} - 0.852\right)^2 - 0.0219}, \tag{2.7}$$

where z_{R} is the Rayleigh range of the beam and P_{peak} is its peak power. L_{c} is often called "nonlinear focus" and for a convergent beam, L_{c} is situated before the geometrical focus f, leading to the effective focal length $L_{\mathrm{c,f}}$ [Cou07]:

$$\frac{1}{L_{\mathrm{c,f}}} = \frac{1}{L_{\mathrm{c}}} + \frac{1}{f}. \tag{2.8}$$

In reality, the ongoing self-focusing is stopped by other nonlinear effects such as the generation of plasma which defocuses the beam. The details about plasma generation are given in Sec. 2.3. Fig. 2.4 gives an overview of the Kerr-induced effects on an intense optical pulse, including the effects of self-phase modulation and self-steepening introduced in the following Sections 2.2.1 and 2.2.2 respectively.

Self-phase modulation

The refractive index $n(\boldsymbol{r},t)$ is a time-dependent quantity due to the temporal variation of the beam intensity $I(\boldsymbol{r},t)$ and follows its variation quasi-instantaneously [Chi10]. This variation of the refractive index in time leads to a temporal modulation of the pulse phase, imprinting the additional time-dependent phase ϕ_{SPM} on the pulse along its propagation direction z [She71]:

$$\phi_{\mathrm{SPM}}(z,t) = \frac{n_2 I(\boldsymbol{r},t)\omega_0}{c}\Delta z, \tag{2.9}$$

Eq. 2.9 shows that the phase increases with increasing propagation distance z. The temporal phase variation is directly connected to the generation of new frequencies in the pulse due to an alteration of the instantaneous frequency $\omega(t)$ via:

$$\omega(t) = \omega_0 + \Delta\omega(t), \tag{2.10}$$

with:

$$\Delta\omega(t) = -\frac{\partial\phi_{\mathrm{SPM}}}{\partial t} = -\frac{n_2\omega_0 z}{c}\frac{\partial I(\boldsymbol{r},t)}{\partial t}. \tag{2.11}$$

The generation of new frequencies is proportional to the slope of the intensity $I(\boldsymbol{r},t)$. The steeper the slope, the broader the generated spectrum. Hence, this effect becomes more and more significant the shorter the pulse duration. Furthermore, due to the negative sign in Eq. 2.11, red frequencies are generated at the rising slope whereas blue frequencies are generated at the falling slope of the intensity. Since the nonlinear phase modulation of the pulse is caused by its own temporal intensity variation this effect is called "self-phase modulation". For a symmetric pulse shape, the broadening is symmetric with respect to the center frequency. SPM is the fundamental mechanism behind several techniques to broaden the spectrum of an ultrashort laser pulse, such as hollow-core fibers [Deb19], multi-plate media [Che16] or laser filamentation [Cou07]. These processes enable the generation of ultrashort laser pulses up to the single cycle regime from typical multi-cycle pulses, around 25 fs to 40 fs, from a laser amplifier in combination with pulse compression [Böh14].

2.2.2 Self-steepening

The initial broadening due to SPM is symmetric for symmetric pulse profiles such as a pulse with Gaussian shape. However, with ongoing propagation of an ultrashort laser pulse in a Kerr medium, the peak of the pulse is slowed down more and more with respect to its trailing edge, since it experiences a higher nonlinear refractive index. Therefore, the trailing edge catches up with the pulse peak leading to an asymmetric pulse shape with a very steep trailing edge compared to the leading edge. This asymmetry in the pulse shape converts into an asymmetric broadening. The generation of blue frequencies in the trailing edge of the pulse is enhanced as the slope is steepened and the generation of red frequencies in the leading edge is weakened since the slope becomes less steep. Consequently, the pulse spectrum shows a strong blue shift with ongoing propagation. Along with the broadening due to SPM, the blue-shift due to self-steepening leads to the typical filament spectra with a low-intense blue tail extending up to the ultraviolet, observed by several experiments [Akö01; Akö06; Cou07; Chi10; Ste12], including the one in Chapter 4.

Nonlinear effects such as the Kerr effect or self-steepening strongly influence the interaction of short laser pulses with the medium and are fundamental for the understanding of filamentation. Above the critical peak power, Kerr-induced self-focusing eventually leads to ionization of the medium generating laser-induced plasma, which is described in the following section.

2.3 Femtosecond laser-induced plasma

The term “plasma” describes a very broad range of mixtures between ionized and neutral particles with orders of magnitude different pressure ranges in very different environments such as stars [Ada63], interstellar dust [Dra79], atmospheric lightning [Sil19], gas discharge lamps [Lis04], or laser-induced plasma [Cap04; Ion15; Gia17] to name a few. It is not possible to describe all forms of plasma here. Therefore, in this thesis, the term plasma is only used in the sense of femtosecond laser-induced plasma from gases, if not stated otherwise. The mechanisms of ionization and recombination of this plasma, play a key role in the understanding of the experiments presented in this thesis. It will be shown in this section, that the process of femtosecond

filamentation is highly influenced by the free electron density ρ_e in the medium, whereas the plasma lifetime is mainly determined by the recombination of the plasma. Throughout this thesis, plasma lifetime is defined as the time it takes for the plasma to decay from its maximum density to $1/e$. In the following, a comprehensive introduction into the main aspects of the ionization, recombination and properties of laser-induced plasma is given.

2.3.1 Plasma parameters

The properties of femtosecond laser-induced plasma are mainly determined by two main parameters: the free electron density N_e and the distribution of the free electron temperature T_e. Both are described in the following.

Free electron density

The free electron density $N_e(\boldsymbol{r},t)$ describes the amount of free electrons per unit volume, usually expressed in [cm^{-3}]. Since free electrons are unbound by definition, they follow the electric field of a laser pulse instantaneously [Kan03; Wah12]. The plasma frequency ω_p represents the maximal frequency of an optical field, the free electrons can possibly follow, it is defined by [Boy09]:

$$\omega_p = \sqrt{\frac{e_c^2 N_e}{m_e \varepsilon_0}}, \tag{2.12}$$

with e_c the elementary charge and m_e the electron mass. Plasma is transmittive for electromagnetic waves when their angular frequency is greater than the plasma frequency or, in an alternative description, if the free electron density is smaller than the critical free electron density N_{crit} given by [Cou07]:

$$N_{crit} = \frac{\varepsilon_0 m_e \omega_0^2}{e_c^2}. \tag{2.13}$$

Since ε_0, m_e and e_c are natural constants, one can also rewrite Eq. 2.13 as:

$$N_{crit} = 1.1 \times 10^{21} \left(\frac{\lambda_0}{1\,\mu m}\right)^{-2} [cm^{-3}], \tag{2.14}$$

with $\lambda_0 = \frac{2\pi c}{\omega_0}$ being the central wavelength of an optical pulse (in µm). Above the critical free electron density, the plasma becomes opaque for electromagnetic waves with the frequency $\omega_0 < \omega_\mathrm{p}$ and these waves are reflected from the plasma.

Since free electrons are always generated from initially neutral particles, the free electron density that is induced by an optical field is linked to the neutral particle density or simply "number density" N_nt for which holds that $N_\mathrm{nt} = \frac{N_\mathrm{A}}{M}\rho_\mathrm{m}$ with N_A being the Avogadro constant, M the molar mass, and ρ_m the mass density. In gases, at a pressure of 1 bar, the number density is about three orders of magnitude smaller than the number density in solids [Chi10]. The generated free electrons alter the refractive index of a medium. The refractive index of plasma, assuming $\omega_\mathrm{p} \ll \omega_0$, is [Pfe06]:

$$n_\mathrm{p}(\boldsymbol{r},t) = \sqrt{1 - \frac{\omega_\mathrm{p}^2}{\omega_0^2}} \approx 1 - \frac{\omega_\mathrm{p}^2}{2\omega_0^2} = 1 - \frac{e_\mathrm{c}^2 N_\mathrm{e}(\boldsymbol{r},t)}{2m_\mathrm{e}\varepsilon_0\omega_0^2} = 1 - \frac{N_\mathrm{e}(\boldsymbol{r},t)}{2N_\mathrm{crit}}. \tag{2.15}$$

Hence, the refractive index of plasma is smaller than 1 and for the change of the refractive index of the medium due to plasma it holds that [LHu91; Bra95; Pfe06]:

$$\Delta n_\mathrm{p} = -\frac{N_\mathrm{e}(\boldsymbol{r},t)}{2N_\mathrm{crit}}, \tag{2.16}$$

which has the effect that the plasma acts like a defocusing lens to an incident light field because the free electron density distribution in space follows the spatial intensity distribution of the light field. Therefore, the plasma refractive index contribution acts inversely to the nonlinear refractive index contribution due to the Kerr effect, thus prohibiting the beam collapse due to ongoing self-focusing. As it will be shown in Sec. 2.1, the balance of self-focusing due to the Kerr effect and defocusing due to plasma generation is the basis of filamentation dynamics. The free electron density, and hence also n_p, only build up during the interaction of an optical pulse with a medium. Plasma recombination, decreasing the free electron density, takes place over much longer periods of time than the fs-regime as it is shown in Chapter 3. Similar to SPM, in which the build up of the pulse intensity generates new frequencies around the central frequency of the pulse, the temporal build up of the plasma also leads to

the generation of new frequencies, due to the additional nonlinear phase shift $\Delta\phi_\mathrm{p}$ [Kan03]:

$$\Delta\phi_\mathrm{p}(t,z) = -\frac{e_\mathrm{c}^2 N_\mathrm{e}(t)}{2m_\mathrm{e}\varepsilon_0\omega_0 c}\Delta z = \frac{N_\mathrm{e}(t)\omega_0}{2N_\mathrm{crit}c}\Delta z. \tag{2.17}$$

Deriving this phase shift with respect to time gives the plasma-induced frequency shift $\Delta\omega_\mathrm{p}$ [Kan03]:

$$\Delta\omega_\mathrm{p} = \frac{\partial\Delta\phi_\mathrm{p}(t,z)}{\partial t} = \frac{\omega_0\Delta z}{2N_\mathrm{crit}c}\frac{\partial N_\mathrm{e}(t)}{\partial t} \tag{2.18}$$

A significant difference to SPM is given by the fact that plasma-induced broadening is asymmetric, since the plasma density monotonously increases during the interaction of the pulse with the medium. As the broadening is proportional to the positive slope of temporal change of the free electron density, it blue-shifts the spectrum, adding up to the blue-shift due to self-steeping.

Free electron temperature distribution

The free electron temperature T_e is an important parameter to describe the collision dynamics in a laser-induced plasma. As such, it mainly describes the recombination, since the ionization happens on the fs-timescale during the pulse-matter interaction [Chi10] whereas plasma dynamics happen on longer timescales [Boy09] from picoseconds [Jar14; Rey18] to nanoseconds [Cou07; Chi10; Ale16]. It is very important to distinguish between the free electron temperature distribution and other temperature distributions, such as the ion temperature distribution. As electrons are much lighter than their parent ions, in good approximation, their response to an external electric field is instantaneous, as explained in Sec 2.3.1. Furthermore, elastic electron-electron collisions, in which free electrons can exchange energy, are very efficient in the typical conditions of a laser-induced plasma [Gia17]. In consequence, the free electron energy distribution has a strong propensity for reaching thermal equilibrium, i.e. a Maxwellian temperature distribution, rapidly [Cap00]. During the ionization, the electrons are heated up much more than the ions since they reach a far greater kinetic energy E_kin. In a typical filament plasma the electrons have a temperature T_e of a few eV for a driving laser with a central wavelength of $\lambda_c = 800\,\mathrm{nm}$ [Kar15], whereas the ions are at room temperature [Ale16]. The average electron energy E_av, the average over the energy distribution of all free electrons, is connected to the free

electron temperature T_e via [Gia17]:

$$E_{av} = \frac{3}{2} k_B T_e \tag{2.19}$$

with k_B the Boltzmann constant set to 1 and the free electron temperature T_e in eV. The total energy of the free electrons E_{tot} is defined as [Gia17]:

$$E_{tot} = N_e E_{av} \tag{2.20}$$

The total energy of the free electrons is an important parameter to describe the recombination of laser-induced plasma and needs to be distinguished from the average electron energy.

The concept of free electron temperature is interconnected with the concept of free electron temperature distribution, due to the multi-particle nature of plasma. This temperature distribution strongly influences the plasma dynamics [Cap00] and recombination [Gia17]. Since the free electron temperature is directly linked to the kinetic energy via Eq. 2.19, plasma dynamics are typically described by means of the (free) electron energy distribution function (EEDF). For a laser-induced plasma, one usually assumes an EEDF with Maxwellian form shortly after the ionization event [Fli10]:

$$W(v) = 4\pi \left(\frac{m_e}{2\pi k_B T_e} \right)^{\frac{3}{2}} v^2 \exp\left(-\frac{m_e v^2}{2 k_B T_e} \right) \tag{2.21}$$

with $W(v)$ being the probability to find a free electron with the velocity v. For this distribution holds by definition that $\int_0^\infty W(v)\mathrm{d}v = 1$. As mentioned earlier, in elastic electron-electron collisions the free electrons can exchange energy and in that way redistribute the EEDF [Gia17]. These collisions are very efficient for a laser-induced plasma [Gia17]. For an ionization degree greater than 10^{-4}, a condition that is fulfilled in a filament plasma (ionization degree of about 10^{-3} [Sch99; Tzo99]), the electron collisions are the dominant process in the plasma [Cri13]. By the electron-electron collisions, the EEDF always rearranges quickly into an Maxwellian shape after any event that affects the distribution.

2.3.2 Ionization

Ionization of a medium by ultrashort laser pulses can take place via the two main processes: multiphoton ionization and tunnel ionization. The dominant process is mainly determined by the intensity of the pulse compared to the atomic field strength of the medium $E_{\mathrm{at}} = e_{\mathrm{c}}/\left(4\pi\varepsilon_0 a_0^2\right) \approx 5 \times 10^9\,\mathrm{V/cm}$ [Boy08], with the Bohr radius $a_0 = \varepsilon_0 h/\left(\pi m_{\mathrm{e}} e_{\mathrm{c}}^2\right) \approx 50\,\mathrm{pm}$ and h being the Planck constant. This atomic field strength is directly connected to the required intensity I_{at} for an optical pulse to reach it [Boy08]:

$$I_{\mathrm{at}} = \frac{1}{2}\varepsilon_0 c\,|E_{\mathrm{at}}|^2 \approx 10^{16}\,\mathrm{W/cm^2}. \tag{2.22}$$

If the intensity is in the range of I_{at}, the perturbative approach for the material response to the optical field, shown in Eq. 2.3, cannot be applied anymore and the response needs to treated fully quantum-mechanically [Kur13]. If the intensity of the pulse is in the range of $10^{13}\,\mathrm{W/cm^2}$-$10^{14}\,\mathrm{W/cm^2}$, the laser-induced ionization is dominated by MPI for a driving laser with a central wavelength of $\lambda_c = 800\,\mathrm{nm}$ [Mul10]. Above $\approx 10^{14}\,\mathrm{W/cm^2}$, TI becomes the dominant ionization process [Amm86] and the ionization takes place in the "strong-field regime". An approach to determine the dominant ionization process is the dimensionless Keldysh parameter γ [Kel65]:

$$\gamma = \sqrt{\frac{I_{\mathrm{p}}}{2U_{\mathrm{p}}}}, \tag{2.23}$$

with I_{p} being the ionization potential of the medium and U_{p} the so-called "ponderomotive potential" or "ponderomotive energy" defined by:

$$U_{\mathrm{p}} = \frac{e_{\mathrm{c}}^2 E^2(\boldsymbol{r},t)}{4m_{\mathrm{e}}\omega^2} = \frac{e_{\mathrm{c}}^2}{4m_{\mathrm{e}}\omega_0\left(\pi c\right)^3} I\lambda^2. \tag{2.24}$$

The ponderomotive potential is the mean kinetic energy of the free electrons oscillating in the electrical field of the pulse [Cou07]. Eq. 2.24 shows that the mean kinetic energy is proportional to the intensity of the light field and to the square of the laser wavelength. Hence, using a driving laser with a longer central wavelength, such as when going from the near-infrared radiation (NIR) range at 0.75 µm - 1.4 µm

to the mid-infrared radiation (MIR) at 3 µm - 8 µm, significantly increases the ponderomotive potential by more than one order of magnitude. In the case of a weak driving field, the ponderomotive potential is much smaller than the ionization potential, so that $\gamma \gg 1$. This case describes the range where MPI is the dominant ionization process. In MPI, multiple photons of the energy $h\nu < I_\mathrm{p}$, with $\nu = \omega/(2\pi)$ being the frequency of the driving field, are absorbed by the medium at the same time, if the sum of their energies exceeds the ionization potential. If more photons are absorbed at the same time than are needed to overcome the ionization potential, the process is called above-threshold ionization (ATI). The MPI rate scales with [Cou07]:

$$W_\mathrm{MPI} = \sigma_\mathrm{K} I^\mathrm{K}, \tag{2.25}$$

with K being the number of photons needed to ionize the medium and σ_K denoting the cross section for absorbing K photons. For $\gamma \ll 1$, the strong-field regime applies and tunnel ionization is the dominant ionization process. In a semi-classical picture, the driving field is assumed to bend the atomic potential during ionization. The potential barrier of a bound electron is therefore reduced, leading to a high probability for the electron to be released into the continuum via the tunnel effect. The tunnel ionization rate W_tunnel can be calculated via the Ammosov-Delone-Krainov (ADK) model [Amm86; Cor93] which is an approximation of the Peremolov-Popov-Terent'ev (PPT) model [Per66]. The probability for ionization scales nonlinearly with the instantaneous field strength of the driving field with the maximum probability for ionization being at the maximum of the electric field [Ste11a]. The free electron density N_e is connected to the ionization rates W_MPI and W_tunnel via rate equations, with the assumption that its temporal derivative $\partial N_\mathrm{e}/\partial t$ can be expressed as $\partial N_\mathrm{e}/\partial t = W(I)(N_\mathrm{nt} - N_\mathrm{e})$ with N_nt being the number density of the neutral particles [Kre16]. For the free electron density then follows:

$$N_\mathrm{e}(t) = N_\mathrm{nt}(0) - N_\mathrm{nt}(t) = N_\mathrm{nt}(0)\left(1 - \exp\left(-\int_{-\infty}^{t} W(t')dt'\right)\right). \tag{2.26}$$

Ionization rate models that are able to describe the ionization dynamics for $\gamma \ll 1$ up to $\gamma \gg 1$ are the Keldysh theory itself, the PPT model and the Yudin and Ivanov (YI) model [Kre16].

The ionization describes the generation of plasma and, in that way, the build-up of a certain free electron density. For any statement about plasma dynamics after ionization it is important to know, how the free electron density decreases over time. The decrease of the free electron density over time is driven by the process of recombination which is introduced in the following section.

2.3.3 Recombination

The recombination of the free electrons with the ionic cores happens after the interaction of an ultrashort optical pulse with the medium. Hence, the description of the process does not involve any external field and the dynamics originate from the plasma itself. In the case of laser-induced plasma, there are three main mechanisms: radiative, three-body-electron-ion and dissociative recombination. However, the dissociative recombination channel only exists for molecular gases and is considered to be too slow to explain the recombination of femtosecond laser-induced plasma [Jar14]. In the radiative (electron-ion) recombination it holds that $e^- + A^+ \rightarrow A + h\nu$ [Fri11], where e^- is a free electron, A^+ is the ionic core and A the recombined neutral atom or molecule. Therefore, in the radiative recombination an ionic core recombines with a free electron, releasing the kinetic energy plus the binding energy of the electron as a photon. However, its cross section is rather small [Fri11] so that this recombination channel can be neglected for fs laser-induced plasma. Directly after the laser-induced ionization, the plasma is dominated by three-body electron-ion recombination [Gia10; Gia17]. Furthermore, this recombination channel is considered to be the dominant one for a plasma temperature of $T_\mathrm{e} > 1\,\mathrm{eV}$ [Fri11], a condition that is fulfilled in laser-induced plasmas with electron temperatures of typically a few eV [Cap00; Kar15]. Three-body electron-ion recombination describes the process $e^- + e^- + A^+ \rightarrow A^* + e^-$, where A^* is an excited atom or molecule after the recombination. It is a step-wise process, in which, initially, an ion captures a free electron in a three-body interaction involving another free electron. Then, the excited atom or molecule releases its excitation energy by further free electron impacts. The last step of de-excitation usually involves a radiative decay [Fri11]. This recombination channel is also possible with the slight variation of another ion, atom or molecule substituting the non-colliding second electron in the process. However, this

variation has a very small cross-section and can therefore be neglected [Fri11]. Along with the direct recombining processes, there are also non-recombining processes that contribute to the overall plasma dynamics by energy transfer between the interaction partners. The two most important processes are elastic electron-electron collisions and inelastic electron-ion or electron-atom collisions. In the first process, free electrons can transfer kinetic energy to another free electron with the sum of the energy of both electrons remaining the same, i.e. $e^- + e^- \rightarrow e^- + e^-$. In the inelastic collisions a free electron interacts with a heavy particle A, i.e. $A + e^- \leftrightarrow A^* + e^-$. The two-sided arrow indicates that the process can happen in both directions: from left to right, the heavy particle A gains energy by the collision with the free electron, while from right to left the electron gains energy by the impact with an excited heavy particle A^*. The elastic electron-electron collision process is crucial for the overall recombination dynamics because it has a very high cross section in laser-induced plasma [Gia17]. Furthermore, its cross section is temperature-dependent and increases for a decreasing electron temperature T_e [Fri11]. For femtosecond laser-induced plasma, with the assumption that three-body electron-ion collisions dominate, the rate equation for the free electron density N_e is given by [Cap00]:

$$\frac{\partial N_\mathrm{e}}{\partial t} = -c_{3\mathrm{body}} N_\mathrm{e}^3. \tag{2.27}$$

The rate factor $c_{3\mathrm{body}}$ is defined as [Fri11]:

$$c_{3\mathrm{body}} = 10^{-14} \frac{\sigma_0}{I_\mathrm{p}} \left(\frac{I_\mathrm{p}}{T_\mathrm{e}} \right)^{4.5} \tag{2.28}$$

with σ_0 being the geometrical atomic cross section and free electron temperature T_e in eV and $c_{3\mathrm{body}}$ having the unit [cm^6/s]. Eq. 2.27 and Eq. 2.28 show, that the recombination heavily depends on the free electron density with a cubic dependency and on the inverse of the free electron temperature with a factor of 4.5. Hence, the recombination is faster, the higher the free electron density and the lower the free electron temperature. With the assumption of an initial Maxwellian shape for the EEDF, the recombination leads to a reduction of free electrons with a low kinetic energy because their recombination cross section is significantly higher than

the recombination cross section of free electrons from the high energy side of the distribution [Gia17]. In principal, this reduction would lead to a non-Maxwellian EEDF and a higher average free electron energy E_{av}. Thus, free electron energy would increase, since $E_{\mathrm{av}} \propto T_{\mathrm{e}}$. However, due to the high efficiency of electron-electron collisions in laser-induced plasma, the deviation from the Maxwellian EEDF is quickly undone as the decrease in the total free electron E_{tot} takes place faster than the increase of the average free electron energy. The absolute cross section for any recombination process involving ions, atoms or molecules is material-dependent, which can lead to drastically different recombination times of the ionized media as it is shown in the experimental analysis of determination of temporal plasma evolution via TH enhancement presented in Sec. 3.3.

The section about laser-induced plasma is concluded with a brief overview on methods to determine the free electron density.

2.3.4 Experimental methods for the determination of the free electron density

Since the recombination dynamics of laser-induced plasma take place on a much longer time scale than the optical pulse, the plasma column maintains well after the passage of the pulse. Applications of laser-induced plasma such as plasma gratings or plasma-based lenses require precise knowledge of the spatial and temporal properties of the free electron density. Therefore, it is crucial to investigate the lifetime of laser-induced plasma and the origin of its decay. In this thesis, a novel method to determine the lifetime of fs laser-induced plasma, directly from third harmonic enhancement in a filament, is introduced. While this method cannot determine the absolute free electron density, several methods for the quantitative determination of the free electron density are also able to determine its temporal evolution. Nevertheless, the third harmonic enhancement method has the strong advantage that temporal plasma evolution is directly imprinted in the temporal trend of the enhancement, whereas the other methods can only reconstruct the plasma density and its temporal trend indirectly with certain assumptions. The existing methods comprise interferometric measurements of plasma-induced phase shifts [Rey18], the analysis of Thomson scattering emission [Dzi10] or the measurement of plasma-induced beam diffraction [Dur12; Jar14] and are briefly described in the following.

Interferometric measurements of plasma-induced phase shifts

In the interferometric method, a pump-probe scheme is used to determine the free electron density [Rey18]. A strong pump ignites the plasma channel and a weak probe is sent through that plasma channel with tunable temporal overlap. After the probe passed the plasma channel, it enters a wavefront interferometer. The plasma causes a phase-shift of the probe that can be determined by the interferogram measured with the interferogram relay imaged on a charge-coupled device (CCD). By scanning the delay of the probe versus the pump, the phase shift can be determined temporally and spatially resolved along the radial profile of the beam. From an Abel transformation [Ma08], applied to the spatio-temporally resolved phase shift data, while correcting for the angle between the pump and the probe beam [Kre93], the change in refractive index caused by the plasma can be determined. This change is directly connected to the absolute free electron density, i.e. the temporal and spatial distribution of the free electron density inside the pump can be determined quantitatively from the measured phase information. In this method, one measures the density from the creation for a maximal time window of a few ns [Rey18].

Thomson scattering

The detection of Thomson scattering (TS) emission by laser-induced plasma can be used to investigate the temporal evolution of the free electron density for larger delays of several hundred of ns up to µs. In this method, one typically uses two laser pulses with a pulse duration of a few ns with an adjustable temporal delay to each other. Whereas the first beam generates the plasma, the weaker second beam, below the breakdown threshold of the investigated material, is used to create the TS emission. The TS signal is recorded by a spectrometer for variable delays between the two and fitted with the spectral density function $S(\boldsymbol{k},\Delta\omega)$ with $\Delta\omega = \omega - \omega_\mathrm{L}$, ω_L being the angular laser frequency and $\boldsymbol{k}$ the wave vector [Dzi06]. From the fit, the free electron density can be determined quantitatively. In that way, by scanning the delay between the two pulses and recording the TS signal for every delay, one can determine the temporal trend of the absolute free electron density of the plasma generated by the first beam. However, according to Dzierżęga *et al.* [Dzi10], the method is limited delays $> 150\,\mathrm{ns}$, because otherwise the TS signal becomes very

broad in the spectral dimension and cannot be distinguished from the background continuous plasma fluorescence signal anymore.

Measurement of plasma-induced beam diffraction

Motivated by studies on the formation of "plasma gratings," Durand *et al.* [Dur12] and Jarnac *et al.* [Jar14] determined the temporal density evolution of laser-induced plasma in several atomic and molecular gases formed by two spatially and temporally overlapping femtosecond filaments. In their approach, the free electron density is determined by measuring the plasma-induced diffraction of a weak probe beam propagating through the intersection point of two filaments in an orthogonal orientation. From the diffraction signal, one derives a fringe pattern, which originates from the laser-induced plasma that changes the spatial distribution of the refractive index in the intersection point. The plasma-induced phase change of the probe pulse is retrieved from a fit of the experimentally determined diffraction pattern. As already mentioned in Sec. 2.3.4, this phase is connected to the free electron density which, in that way, can be estimated from the measured probe diffraction pattern.

The description of laser-induced this section completes the introduction all fundamentals required to understand filamentation models and pulse propagation effects that are described in the following.

2.4 Filamentation models and pulse propagation effects

In this section, a basic insight into common filamentation models that encompass descriptions of central pulse effects and dynamics is given. Furthermore, the Nonlinear Envelope Equation is introduced with which a large variety of nonlinear propagation dynamics of a femtosecond filament can be calculated. Subsequently, characteristic nonlinear filament pulse propagation effects are described.

2.4.1 Moving focus model

In the moving focus model [Lug68; She84; Bro97], a filament describes a series of nonlinear foci, related to different weakly coupled time slices of the temporal pulse with a peak power higher than the critical peak power P_{crit}, that travel through the medium along with the temporal pulse, with the pulse peak having the shortest

nonlinear focal distance. In this model, the filament does not extend further than the geometrical focus. This model property is in contradiction with many observations from experiments with fs laser pulses [Cou07]. Furthermore, the moving focus model completely neglects the influence of plasma to the filament propagation and needs to be severely modified, if the influence of plasma shall be included into the analysis [Cou03].

2.4.2 Self-guiding model

The self-guiding model [Bra95] is an extension of the "self-trapping"-model [Chi64], in which the filament is described as an equilibrium between self-focusing and defocusing due to natural beam diffraction. However, an equilibrium of self-focusing and beam diffraction is considered unstable [Cou07] and will either loose the balance towards diffraction of the whole beam or catastrophic self-focusing [She84]. The self-guiding model extends the self-trapping model by introducing plasma defocusing, due to an envelope-intensity-dependent spatial distribution of the free electron density, in addition to defocusing by beam diffraction. The term "self-guiding" is derived from the idea that a filament beam creates its own guiding channel, balancing self-focusing, plasma defocusing and beam diffraction. Therefore, the beam remains focused for a long propagation distance without the need of an external guiding mechanism. The equilibrium condition can be expressed as [Cou07]:

$$n_2 I = \frac{N_\mathrm{e}(I)}{2N_\mathrm{crit}} + \frac{(1.22\lambda_0)^2}{8\pi n_0 w_0^2}, \tag{2.29}$$

where the term on the left side of the equation describes the nonlinear focusing, the first term on the right side of the equation the plasma defocusing, the last term the defocusing by beam diffraction, with w_0 being the minimal beam radius at the focus. In this model, the filament is built by many focusing-defocusing cycles that form a dynamic balance and, overall, create a long self-guided light channel in the propagation medium. Due to the balance between the two intensity- and spatially-dependent effects, self-focusing due to the Kerr effect and the defocusing due to plasma generation, the beam reaches a so-called "clamping intensity". If one models the free electron density with MPI to $N_\mathrm{e}(I) = \sigma_\mathrm{K} I^\mathrm{K} \left(N_\mathrm{nt} - N_\mathrm{e}(I)\right) \tau_\mathrm{p}$, with

τ_p being the pulse duration, the clamping intensity can be defined as [Cou07]:

$$I_\mathrm{clamp} \approx \left(\frac{0.76 n_2 N_\mathrm{crit}}{\sigma_\mathrm{K} N_\mathrm{nt} \tau_\mathrm{p}} \right)^{\frac{1}{K-1}} . \tag{2.30}$$

Eq. 2.30 gives a clamping intensity of ca. 39 TW/cm^2 for argon at atmospheric pressure with a pulse of $\tau_\mathrm{p} = 30$ fs duration at a central wavelength of 800 nm [Kre16]. The clamping intensity from this model needs to be regarded as an estimate, since it neglects any nonlinear effects on the temporal shape of the pulse or spatial dynamics of the intensity. In this model, the filament is terminated when, due to energy loss by multiphoton absorption and MPI, there is not enough energy anymore to reach a balance between focusing and defocusing effects. However, it can extend further than the predicted termination point, with an energy imbalance of some degree: the core of the filament, where all nonlinear interaction takes place, is surrounded by the so-called "reservoir", an energy hull, that supplies the filament core with energy [Nib96], containing up to 50 % of the total energy [Liu05a].

2.4.3 Dynamic spatial replenishment model

The dynamic spatial replenishment model [Mle98] is an extension of the self-guiding and the moving focus models [Mle99] for high pulse intensities. It additionally takes into account spatio-temporal pulse dynamics during filament propagation. In this model, the ionization takes place on the leading part of the pulse after self-focusing. The generated plasma remains as a thin, ionized channel by which the trailing part of the pulse is defocused while the leading part is decreased due to multiphoton absorption. As a consequence, the beam can self-focus again, leading other focusing-defocusing cycles, as described in the self-guiding model, until the power of the pulse is not sufficient anymore for another cycle and the filamentation process stops.

2.4.4 Summary of the filamentation models

Overall it can be summarized, that the filamentation dynamics can become very complex due to the involved nonlinear effects. Therefore it is difficult to choose a single model that covers all existing phenomena. Moreover, the experimental access for the validation of the theoretical models remains a challenging task due to the high

intensities of around 10^{13}-$10^{14}\,\mathrm{W/cm^2}$ reached in a filament - an intensity regime, in connection with the respective fluence, which is at or above the damage threshold of solid state optics [Gam02]. Hence, the presented models only cover aspects of the filamentation process. In fact, its dynamics are still an active research topic, experimentally as well as theoretically. As the filamentation process consists of spatial and temporal dynamics as well as couplings between the two, comprehensive models need to describe spatio-temporal dynamics. In the following, the Nonlinear Envelope Equation (NEE) [Bra97] is described briefly which is used for modeling the dynamic spatial replenishment model. With the NEE, a large variety of the spatial and temporal dynamics as well as spatio-temporal couplings of the filament pulse propagation of few-cycle laser pulses can be calculated numerically.

2.4.5 Nonlinear Envelope Equation

The NEE is a generalization of the Nonlinear Schrödinger Equation (NLSE), for short laser pulses in the fs-regime with a broad spectrum, without the NLSE's slowly varying envelope approximation (SVEA). The model for NEE presented here is based on a model having been developed by Skupin *et al.* and Brée *et al.* [Sku06; Bré09; Bré10]. The NEE is derived from the Maxwell equations. A complete derivation can be found in [Bré12]. This brief description is based on that work. The final NEE equation is given by:

$$\begin{aligned}\frac{\partial}{\partial z}\boldsymbol{\mathcal{E}} = &\underbrace{\frac{i}{2k_0}T^{-1}\vec{\nabla}_\perp^2\boldsymbol{\mathcal{E}}}_{\text{(a)}} + \underbrace{iD\boldsymbol{\mathcal{E}}}_{\text{(b)}} + \underbrace{i\frac{\omega_0}{c}n_2 T\left|\boldsymbol{\mathcal{E}}\right|^2\boldsymbol{\mathcal{E}}}_{\text{(c)}} \\ &\underbrace{-i\frac{k_0}{2N_\mathrm{crit}}T^{-1}N_\mathrm{e}\boldsymbol{\mathcal{E}} - \frac{\sigma_\mathrm{col}}{2}N_\mathrm{e}\boldsymbol{\mathcal{E}} - \frac{I_\mathrm{p}W(I)\left(N_\mathrm{nt}-N_\mathrm{e}\right)}{2I}\boldsymbol{\mathcal{E}}}_{\text{(d)}},\end{aligned} \tag{2.31}$$

with $\boldsymbol{\mathcal{E}}$ the (vectorial) electric field of the pulse, the operator $T = 1 + (i\omega_0)\,\frac{\partial}{\partial t}$ and the operator D with its Fourier transform given by $\tilde{D}(\omega) = k(\omega) - k_0 - (\omega - \omega_0)\,\frac{\partial k}{\partial \omega}\big|_{\omega=\omega_0}$ and σ_col being the cross section for collisional ionization. The NEE, shown in Eq. 2.31, consists of many terms that can be subdivided into four main groups (a),(b),(c),(d) and are explained in the following. Group (a) is related to the diffraction of the

beam. Group (b) is related to the dispersion, with the operator D represented in the Fourier domain as $\tilde{D}$. Part (c) is related to the nonlinear polarization $\boldsymbol{P}_{\mathrm{NL}}$ and, hence, the influence of the Kerr effect. With the operator T, space-time focusing as well as self-steepening are taken into account, enabling the validity of the model in the few-cycle regime. The inverse operator T^{-1}, in group (a) and (d), is treated in the Fourier domain. The last group (d) is connected to the current density $\boldsymbol{J}$ and hence to the influence of plasma by the free electron density N_{e}. The first term in group (d) is related to the defocusing effect due to N_{e}. The second term describes the generation of free electrons due to collisional ionization and the third term due to field ionization processes. The free electron density N_{e}, in this numerical model, is calculated via the following rate equation:

$$\frac{\partial N_{\mathrm{e}}}{\partial t} = W(I)\,(N_{\mathrm{nt}} - N_{\mathrm{e}}) + \frac{\sigma_{\mathrm{col}}}{I_{\mathrm{p}}} I N_{\mathrm{e}} \tag{2.32}$$

In the NEE model the ionization rate $W(I)$ is modelled via the PPT theory. Simulations with the NEE accurately show nonlinear filamentation propagation phenomena such as self-compression and pulse splitting. These phenomena are presented in the following.

2.4.6 Self-compression

It has been already shown theoretically [Hau04; Cou05; Cou06], as well as experimentally [Hau04; Cou06; Kre14], that an incident pulse can self-compress in a filament. Couairon *et al.* [Cou05; Cou06] predicted and Kretschmar *et al.* [Kre14] proofed experimentally, that nearly single-cycle pulses with less than 5 fs can be generated directly from a filament [Cou07]. Self-compression can be understood by taking into consideration the intra-pulse dynamics during filament propagation. As the front of the pulse is self-focused, it generates plasma when the intensity is high enough. The plasma defocuses the trailing part of the pulse. However, the front can continue to self-focus, leading to the effect of self-steepening, inducing a strong spectral broadening. During subsequent propagation, the trailing part of the pulse can self-focus again, leading to a formation of two peaks, i.e. a pulse splitting event. With ongoing propagation the front part of the two-peak structure decreases, while

a short pulse in the back of the structure remains [Chi10]. The self-compression effect requires a careful balance between the Kerr effect, the ionization and the gas pressure in order to take place at certain positions along the length of the filament [Cou07]. With a good balance, and terminating the filament at the right position, compression factors of up to a factor of 10 have been shown experimentally [Kre14]. Furthermore, at some positions in the filament, the pulse has a broad spectrum but not a flat spectral phase so that the pulse is not in its Fourier limit. By then applying pulse compression techniques, like double-chirped mirrors (DCMs), the chirp can be compensated and pulse durations close to the single-cycle regime can be achieved [Hau04; Cou06]. Therefore, filamentation serves as an alternative to other pulse compression techniques, requiring not more than a gas cell for the filamentation medium and a lens to focus an intense beam into the cell for generating the filament inside. Self-compressed filament pulses are ideally suited to be used for extreme ultra violet (XUV) experiments as a driving laser source, first demonstrated in [Lan98] for high-order harmonic generation (HHG). In [Zaï07], the self-compression technique was applied to a two-stage filamentation setup with DCM chirp compensation generating sub-10 fs after the first stage and sub-5 fs after the second stage, enabling HHG after both stages. Simulations predict that self-compressed filament pulses can even be used for the generation of isolated attosecond pulses (IAPs) [Cha06; Cou08] and experiments showed already that the filament pulses can be used to generate continuous XUV spectra [Lee09; Ste09b; Ste11b]. Furthermore, it has already been shown that HHG can be generated directly from certain positions inside a filament [Voc12; Ste11a; Ste11b; Kre16]. In the following, pulse splitting is described in more detail.

2.4.7 Pulse splitting and intensity spikes

The formation of pulse splitting is closely connected to self-compression in filamentation, discussed in the previous Section 2.4.6. As already mentioned, the balance between Kerr-induced self-focusing and plasma-induced defocusing, along with beam diffraction, is dynamic. Hence, the clamping intensity can be exceeded during the filament propagation, leading to very high intensity spikes, as theoretically predicted by [Gaa09; Kre16] and experimentally found by [Ste11b], investigating HHG spectra directly from the filament. In the case of [Kre16], the intensity spikes are predicted to be created with very short driving pulses of 5 fs in the filament but the reason

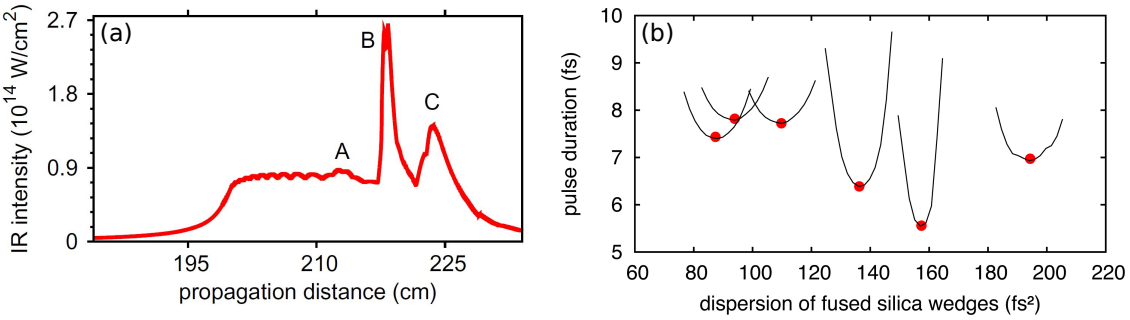

Figure 2.5: Intensity spiking and pulse splitting in femtosecond filaments. (a) simulated intensity evolution of a measured femtosecond filament in argon atmosphere [Ste11b]. A, B and C indicate positions at which high harmonics where measured. A distinct intensity spike occurs at position B. Adapted from [Ste11b] under the CC BY-NC-SA 3.0 license. (b) reconstructed individual sub-pulses (red dots) generated by a pulse splitting event in a femtosecond filament in argon atmosphere originating from a single driving pulse [Ste12]. The sub-pulses show an individual dependency on the pulse chirp as displayed by their calculated pulse durations for certain dispersion settings (black lines), a clear indication of a nonlinear pulse splitting event. Adapted with permission from [Ste12] © The Optical Society.

for the formation of the spikes is not entirely clear. In case of [Gaa09; Ste11b], the intensity spikes are created by an interplay of intra-pulse dynamics. The plasma generation on the leading part of the pulse defocuses its trailing part, which is spatially separated from the main pulse, i.e. a pulse splitting event occurs. The trailing part can self-focus again onto the optical axis during further propagation [Ste11a]. In this refocusing event, the trailing part of the pulse merges again with the leading part which remained on-axis. This merge creates a very strong local change of the filament intensity that is not compensated by plasma defocusing or beam divergence, due to the short time frame of that dynamical event. Along with the intensity spike during that merge, very short sub-pulses in the range of one optical cycle are generated [Gaa09]. Another possibility to exceed the clamping intensity is to use a tight focusing for filament generation. In that way the clamping intensity could be exceeded by more than one order of magnitude [Pre10]. Fig. 2.5(a) shows an example for intensity spikes in a measured filament in argon atmosphere [Ste11b] and Fig. 2.5(b) for a pulse splitting event in another filament in argon atmosphere [Ste12].

The high intensities present in a filament also efficiently drive the generation of new frequencies such as THz- or XUV-radiation via the nonlinear susceptibilities of the filament medium. The lowest frequency of nonlinear order that is generated inside the filament is the TH which is used to probe the laser-induced temporal plasma evolution in [Jus19], the details of that experiment are presented in Section 3. Due to its importance for the understanding of those experimental results, the details of THG inside a filament are described in the following.

2.4.8 Third harmonic generation

Since the TH is the lowest nonlinear radiation inside the filament, it is also generated with the highest efficiency. The polarization of the medium for THG is defined as:

$$P^{(3)}(\omega) = \frac{\varepsilon_0}{4}\chi^{(3)}(3\omega : \omega,\omega,\omega)E(\omega)E(\omega)E(\omega) \tag{2.33}$$

For a high conversion efficiency of THG, the fundamental wave and the third harmonic wave need to be phase-matched. However, due to the Gouy phase shift at the geometrical focus [Boy80], most TH generated in the first half of the filament is reconverted into the fundamental in the second half [Akö02; Thé05; Liu11]. The Gouy phase is a fundamental effect of Gaussian beams. It describes a phase shift of a Gaussian beam that appears at its focus where the wavefronts of the beam change their sign. It is defined by [Fen01]:

$$\phi_{\mathrm{Gouy}}(z) = \arctan\left(\frac{z}{z_{\mathrm{R}}}\right) \tag{2.34}$$

with $z_{\mathrm{R}} = (\pi w_0^2)/\lambda$ being the Rayleigh length of the beam. Eq. 2.34 shows that most of the Gouy phase shift takes place around the focus of the beam but the largest Gouy phase difference exists between $z \ll -z_{\mathrm{R}}$ and $z \gg z_{\mathrm{R}}$ with $\Delta\phi_{\mathrm{Gouy}} = \pi$. Any radiation generated before the focus would have a π-phase shift with respect to radiation generated after the focus, so that they cancel each other. A filament does have a modified Gouy phase shift that differs from the standard shift defined for a Gaussian beam in having a less steep slope than the corresponding beam in vacuum with linear focusing conditions [Bai12]. Nonetheless, the general statement

of cancellation remains valid. With increasing intensity, other nonlinear effects reincrease the TH efficiency [Akö01; Akö02]. Hence, a net TH can remain at the end of the filament. The mechanism for efficient THG in a filament is still an open research topic [Liu19]. One suggested explanation is that the Kerr effect and the plasma-reduced refractive index lead to improved phase matching up to even phase locking between the fundamental and the third harmonic wave [Liu19]. Due to the underlying spatial conditions for phase matching, the optimal phase is reached on a cone around the core of the filament, that contains 90 % of the total TH energy, whereas the on-axis TH only inhibits 10 % of the total energy [Thé05]. The very low efficiency of THG on axis renders this TH radiation impractical for a lot of applications. However, several methods to severely enhance the on-axis TH in a filament via perturbing the filament propagation by an obstacle exist and are presented in the following.

Principle of TH enhancement

TH enhancement describes the increase of net TH energy on axis at the end of a filament by means of a perturbation in comparison to an undisturbed filament. The source of the perturbation can, in principle, be any object, transparent or not, with a size comparable to the filament core (around 100 µm in diameter for an air filament at ambient pressure [Cou07]), that introduces a disturbance in the filament spatial profile. If the object is bigger than the filament core, it needs to be transparent for the TH emission. Very different objects inserted into the filament have already shown to significantly enhance the TH. Among these are: water droplets [Xi09], metallic wires [Zha10], thin metal plates followed by a pressure gradient [Sch11b], glass wedges [Yao12], laser-induced plasma [Sun09; Sun10; Liu11; Gry17] or the interaction of two filaments [Liu11; Yao12]. Enhancements up to two orders of magnitude in the case of plasma-induced enhancement and up to three orders of magnitude by a sharp pressure gradient [Sch11b] have been achieved. In the plasma-induced enhancement, the THG process is shown to reach an efficiency of up to 0.1 % [Liu19] and the temporal trend of the TH is directly connected to and follows the temporal free electron density evolution [Sun09; Sun10]. A thorough experimental study and analysis for an explanation of TH enhancement in filaments was performed in [Liu11;

Liu19]. By measuring the generated TH energy of an air filament propagating through self-drilled holes in thin metal foil, a TH enhancement dependent on the foil position in the filament was observed [Liu19]. There is a maximum of TH yield, when the filament is terminated in its middle and a symmetric decrease of TH yield towards a termination at the beginning or end. This observation led to the conclusion that the TH enhancement is caused by the partial termination of further filament development, which arrests the large cancellation of THG by introducing a symmetry break [Xi09; Zha10]. As mentioned in Sec. 2.4.8, due to the Gouy phase shift in the filament focus, the TH generated in the first and second half have opposite phase. Hence, the TH yield builds up during the first half and then decreases after the focus as TH energy as the TH before and after the focus cancel each other so that the TH energy is reconverted to the fundamental, from that point. Thus, the obstacle in the beam path suspends the back conversion of the TH energy to the fundamental and enhances the TH yield severely [Liu11]. This explanation is supported by observations made in [Liu11]: a thin metal foil with a pre-drilled hole of 100 µm diameter was placed in the filament beam at different positions behind the focus. When the beam was additionally crossed by a plasma spot from a strong pump pulse around the focus position, it showed a significantly weaker decrease in TH yield compared to the undisturbed filament. However, it was found out that the TH conversion process and enhancement are even more complex, making the statement about the reconversion to the fundamental in the center of the filament only true for some parameter configurations [Liu19]. The TH conversion and enhancement are strongly influenced by the focusing conditions of the beam forming the filament, the pulse energy and also the gas pressure. Further, when no reconversion to the fundamental took place, the TH cannot be enhanced at all. Nonetheless, if a TH enhancement for the given experimental parameters is possible and the enhancement is plasma-induced, the principle that the temporal evolution of the TH enhancement follows the temporal evolution of the plasma remains correct.

The interesting aspect about using plasma for TH enhancement is its transparency for both the fundamental and third harmonic radiation and the tunability of the plasma density and thus the TH enhancement. Furthermore, the plasma density, as it is shown later experimentally, is a time-dependent quantity. By knowing precisely the

decay of the plasma, the TH signal strength can be controlled in time, if the plasma generation is temporally tuned with respect to the filament pulse. Additionally, plasma has no damage threshold since it is already composed of an ionized medium. As such, it is ideal to scale the TH enhancement process to very high intensities or pulse energies, interesting for any application requiring a high-intense and ultrashort ultra violet (UV) laser pulse such as micromachining [Bék03].

The next important aspect of this thesis that is presented, is the pulse characterization of optical laser pulses in the fs range and of filament pulses in particular. The pulse characterization of a filament is a challenging task due to the high intensities reached in the core, as well as the drastic changes in the pulse properties along the filament length. Hence, there is a striking need for a complete spatio-temporal characterization of a filament along its length, which is the key motivation behind the experiment presented in Chapter 4. For this experiment, it is important to understand common spatio-temporal and temporal pulse characterization techniques, as well as possible spatio-temporal couplings of ultrashort laser pulses, which are presented in the following.

2.5 Spatio-temporal characterization of ultrashort laser pulses

The spatial and temporal properties of an optical pulse can be coupled to each other, i.e. the electric field of the pulse cannot be described anymore as a product of its spatial and temporal properties. In this case it holds that [Akt10]:

$$E(x,y,t) \neq E_x(x)E_y(y)E_t(t) \tag{2.35}$$

with x and y being the transverse spatial coordinates of the pulse and $E_x(x)$, $E_y(y)$ representing the electric field along these coordinates as well as $E_t(t)$ describing the temporal properties of the pulse. Eq. 2.35 specifies the presence of one or more spatio-temporal couplings (STCs) in an optical pulse. During nonlinear pulse propagation, the temporal and spatial properties of an optical pulse can even couple dynamically which is referred to as spatio-temporal dynamics. Femtosecond filaments in gaseous media inhibit strong spatio-temporal dynamics, as introduced in the previous Section 2.1. For a complete understanding of their dynamics, a spatio-temporal

pulse characterization method is needed. In general, every pulse characterization technique has advantages and disadvantages and it always needs to be evaluated, which method suits best the experiment that is carried out. In this section, the general aspects of STCs in ultrashort laser pulses are described in detail and different techniques to characterize an ultrashort laser pulse spatio-temporally are explained. This description includes the technique that is chosen for the experiment described in Chapter 4: spatially resolved Fourier transform spectrometry. In the following, STCs are introduced.

2.5.1 Spatio-temporal couplings

Eq. 2.35 shows that if an optical pulse inhibits a spatio-temporal coupling, the pulse needs to be described or characterized in the spatio-temporal domain to obtain a complete picture of its properties. A solely temporal or spectral pulse characterization is blind for STCs as it cannot resolve the coupling of the domains. However, STCs widely occur in both linear and nonlinear pule propagation, e.g. already when an ultrashort laser pulse propagates through a prism. In that case, the output beam experiences angular dispersion, i.e. the different colors of the pulse spectrum travel in different directions, and pulse front tilt, i.e. the wavefront of the pulse is tilted with respect to the propagation direction by the prism. These two effects result in spatial chirp over the beam profile after propagation. Even the propagation of an ultrashort pulse through a circular shaped aperture can already cause a STC [Akt10]. The concept of STCs was introduced in [Bor89a; Bor89b; Bor92]. An comprehensive overview on STCs can be found in [Jol20] and [Akt10], while here only their main features are reported. In general, the impact of STCs increases the shorter, due to dispersion, and the more intense, due to nonlinear propagation effects, a laser pulse is. There are four equivalent domains in which the spatio-temporal properties of an ultrashort laser pulse can be described, namely the (x,t)-, the (x,ω)-, the (k_x,t)-, and the (k_x,ω)-domain. An STC is by definition present in at least two domains, hence it also needs to be described in two out of the four coordinates t, ω, x and k_x (note that only using x and k_x is a simplification, the other Cartesian coordinates y and z as well as the reciprocal coordinates k_y and k_z apply as well). In first order, all four domains have one complex-valued coupling term, can be used

interchangeably and are connected via Fourier transforms. The real part of the respective coupling term is related to intensity effects, whereas the imaginary part of the coupling term is related to phase effects [Rho17]. Since there are four domains with one complex-valued coupling term for each, in total there are eight couplings or first-order STCs, four intensity and four phase couplings, with only two of the couplings being independent from each other. Although all domains are equivalent descriptions of a STC, it can be useful to choose a certain domain for the description of a coupling because its impact on the pulse can be much clearer in a particular domain than in another one. Tab. 2.1 shows an overview of all first-order STCs acting on the intensity and phase of an ultrashort laser pulse.

Table 2.1: Overview of the first-order spatio-temporal couplings acting on the intensity and phase of the pulse.

Domain	**Intensity coupling**	**Phase coupling**
(x, t)	Pulse front tilt	Wavefront rotation
(x, ω)	Spatial chirp	Wavefront tilt dispersion
(k_x, t)	Time versus angle	Angular temporal chirp
(k_x, ω)	Angular dispersion	Angular spectral chirp

Any intensity coupling generates a contribution to the phase coupling of the connected Fourier domain. Pulse characterization techniques can usually measure very well pulse intensities so that intensity-sensitive couplings can be detected well. Phase-sensitive couplings are usually harder to measure directly. However, due to the connections between the different domains, phase couplings can be expressed in terms of intensity couplings, providing an indirect way for their detection. Since only two out of the eight possible couplings are independent, it is possible to express any STC by a combination of two other STCs. An important consequence for the experimental characterization of STCs is that only two different STCs need to be measured so that all other couplings can be reconstructed, if the beam and pulse parameters are determined additionally [Akt10]. The STC principles, introduced for first-order couplings, can also be extended to higher orders, once the complete spatio-temporal electric field in one of the four domains is known, by extending

the beam and pulse parameters to high-order terms. To analyze these higher-order couplings, the spatio-temporal electric field known in one domain simply needs to be transferred to the other three respective domains numerically. First-order couplings can also be present along with high-order couplings, which can render the STC of an ultrashort pulse very complex. As it is laid out earlier in Sec. 2.4.3 about the model of dynamic spatial replenishment and in Sec. 2.4.7 about the pulse splitting in femtosecond laser filaments, filaments in fact show strong and even dynamic STC due to the nonlinear effects taking place inside, underlining the need for a spatio-temporal characterization method.

In conclusion, it can be said that STCs are omnipresent in the propagation of ultrashort laser pulses, their impact becoming the stronger, the shorter and more intense the pulse. For femtosecond filamentation in gases the consequence is that its characterization crucially needs to analyze the complete spatio-temporal electric field in order to give a comprehensive statement about its pulse evolution and propagation dynamics. In the following, a brief introduction into existing common spatio-temporal pulse characterization methods is given, without the claim of completion.

2.5.2 Spatially resolved Fourier transform spectrometry

The spatio-temporal pulse characterization method "spatially resolved Fourier transform spectrometry", is a self-referenced version of Fourier transform spectroscopy (FTS) developed simultaneously and independently by [Mir14] and [Gal14], later called TERMITES [Par16]. This characterization method is chosen for the experiment to determine the spatio-temporal dynamics along the length of the filament, presented in Chapter 4. It is part of one out of two large classes of methods for spatio-temporal pulse characterization called "spatially-resolved spectral measurement techniques" [Jol20]. The principle setup is illustrated in Fig. 2.6. A collimated incident beam is sent onto a Mach-Zehnder type interferometer. One arm serves as a reference and the other as a signal. The signal arm contains the pulse to be measured while the pulse in the reference arm needs to be known temporally by means of an additional temporal pulse characterization method. In the reference arm, the delay τ between the two arms can be tuned by means of a movable retroreflector and the pulse is subsequently focused by an off-axis paraboloid (OAP) mirror with a very short focal length in

order to generate a tight focus. In the focus, an iris can be inserted that acts as low-pass filter for the spatial frequencies of the beam. After the tight focus, the beam diverges strongly, which creates homogeneous spherical wavefronts shortly after. The unmanipulated signal beam recombines with the diverging reference beam at the second beam splitter, generating a spatial interference pattern which is recorded by a CCD camera. The pixel size of the CCD determines the sampling of the spatial frequencies of the beam of interest. A measurement is performed by scanning the delay between the reference and signal pulse while recording the spatially resolved interference pattern for every delay step τ with the CCD camera. After a complete scan, every pixel of the CCD contains an interferogram of the spatially homogeneous reference arm and the spatially varying signal pulse at that point in space. If one assumes an unknown complex electric field $\tilde{E}(\omega) = \left|\tilde{E}(\omega)\right| \exp\left(i\phi(\omega)\right)$ in the spectral domain with the respective field $E(t) = |E(t)| \exp\left(i\phi(t)\right)$ in the temporal domain and a known complex reference electric field $E_{\mathrm{ref}}(t)$, the interferogram $I(\tau)$ as function of delay per CCD pixel is given by [Mir14]:

$$I(\tau) = \int |E(t) + E_{\mathrm{ref}}(t-\tau)|^2 \, \mathrm{d}t, \tag{2.36}$$

which is equal to:

$$I(\tau) = \int |E(t)|^2 \, \mathrm{d}t + \int |E_{\mathrm{ref}}(t)|^2 \, \mathrm{d}t + \int E(t) E^*_{\mathrm{ref}}(t) \mathrm{d}t + \int E^*(t) E_{\mathrm{ref}}(t) \mathrm{d}t, \tag{2.37}$$

where * denotes the complex conjugated electric field. The wanted information for the pulse reconstruction is contained in the mixed-field terms of Eq. 2.37. By applying a Fourier transform, the mixed- and equal-field terms can be easily separated from each other:

$$\begin{aligned} \mathcal{FT}\{I(\tau)\} = \mathcal{FT}\left\{ \int |E(t)|^2 \, \mathrm{d}t + \int |E_{\mathrm{ref}}(t)|^2 \, \mathrm{d}t \right\} \\ + \tilde{E}(\omega)\tilde{E}^*_{\mathrm{ref}}(\omega) + \tilde{E}^*(-\omega)\tilde{E}_{\mathrm{ref}}(-\omega). \end{aligned} \tag{2.38}$$

The term $\tilde{E}(\omega)\tilde{E}^*_{\mathrm{ref}}(\omega)$ of Eq. 2.38, containing the pulse information of interest, can be rewritten into the form:

$$A_{\mathrm{cross}}(\omega) = \left|\tilde{E}(\omega)\right| \left|\tilde{E}_{\mathrm{ref}}(\omega)\right| \exp\left(i\left[\phi(\omega) - \phi_{\mathrm{ref}}(\omega)\right]\right). \tag{2.39}$$

Eq. 2.39 shows that the cross-correlation signal between the signal beam and the reference beam can be expressed as a product of their pulse amplitudes along with their phase difference. Note that for simplification Eq. 2.39 omits the additional spherical curvature of the reference pulse due to tight focusing with the OAP. If the spectral phase of the reference pulse is known by means of an additional temporal pulse characterization technique and the reference pulse' spectrum covers the spectral width of the signal pulse, the complete electric field of the signal pulse can be reconstructed spatially-resolved. Even if the reference beam is not known, the cross-correlation term still shows the relative spatial distribution of the signal pulse with respect to the unknown reference. The reconstruction of the signal beam requires

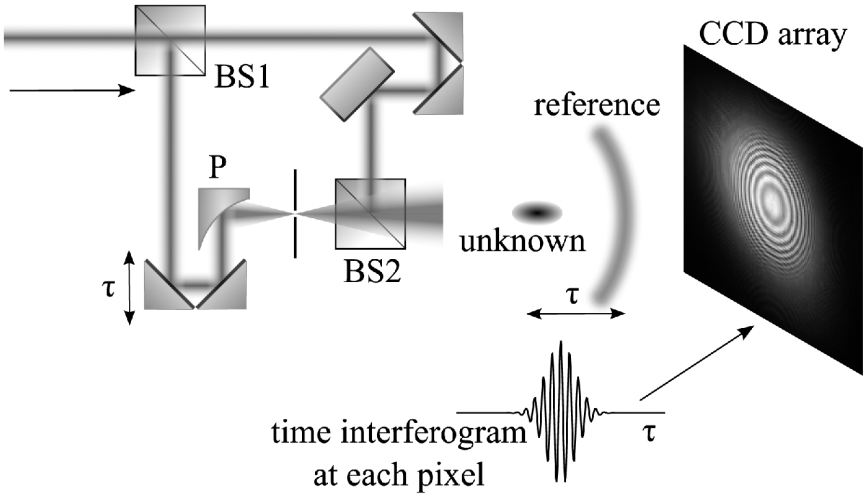

Figure 2.6: Principle setup of the spatially resolved Fourier transform spectrometry method [Mir14]. The beam is split into two arms by a beam splitter. The reference beam is sent onto a movable retroflector and tightly focused by an off-axis paraboloid mirror. The unaffected signal beam interferes with the spatially expanded and homogeneous reference after a second beam splitter and the interference pattern is recorded on a CCD. Reprinted with permission from [Mir14] © The Optical Society.

the reference beam, i.e. the strongly diverging beam from the focus of the OAP with spherical wavefronts, to be homogeneous across the whole area of the CCD and free from any STCs. The higher the spatial homogeneity of the reference beam, the better the reconstruction of the signal beam. In the setup itself, a higher homogeneity of the reference beam could be achieved by a tighter focusing with the OAP. However, the limit is given by the combination of the minimal focal spot size of the OAP with the maximal pulse energy of reference pulse that does not lead to ionization in the focus. Laser-induced plasma would lead to beam distortions. In practice, the homogeneity of the reference is limited by the maximal available power for creating the reference beam – as it is strongly diverging it rapidly decreases in signal intensity from the focus of the OAP – while maintaining a necessary minimal signal beam strength for generating an interference pattern with enough fringe contrast for a successful pulse reconstruction. The signal beam's size on the CCD plays an important role in the recording of the spatially-resolved interference pattern. Since the reference beam is heavily divergent, whereas the signal beam is collimated, the fringe spacing across the spatial interference pattern is not constant. Thus, there are technical requirements on the CCD for a sufficient recording of the interference pattern given by the required amount of pixels N_{pixel} over the beam diameter is [Jol20]:

$$N_{\mathrm{pixel}} = \frac{p_{\mathrm{pixel}} D_{\mathrm{beam}}^2 \beta}{2\lambda_0 |f|}, \tag{2.40}$$

with p_{pixel} being the amount of pixels required at the edge of the beam to resolve the interference pattern, the collimated beam diameter D_{beam}, β the fraction of the incident beam used to create the reference and f the focal length of the mirror to focus the reference beam. Since N_{pixel} is the amount of pixels required along one spatial axis, the total amount of required pixel is N_{pixel}^2. The demands on the CCD for a sufficient beam sampling can lead to very big data sizes in the range of hundreds of megabytes up to gigabytes for the complete scan. However, in the subsequent data processing the data set can be shrunk massively. The spatially-resolved signal pulse in the spectral domain $\tilde{E}'(x,y,\omega)$, including the spherical curvature of the reference

pulse, can be obtained via the relationship:

$$\tilde{E}'(x,y,\omega) = \frac{A_{\text{cross}}(x,y,\omega)}{\tilde{E}_{\text{ref}}(\omega)} e^{i\phi_{\text{ref}}(\omega)}, \tag{2.41}$$

which can be rewritten to:

$$\tilde{E}'(x,y,\omega) = \frac{|A_{\text{cross}}(x,y,\omega)|\, e^{i\phi(x,y,\omega)}}{\sqrt{|A(x_{\text{c}},y_{\text{c}},\omega)|} e^{i\phi(x_{\text{c}},y_{\text{c}},\omega)}} e^{i\phi_{\text{ref}}(\omega)}, \tag{2.42}$$

with $(x_{\text{c}}, y_{\text{c}})$ representing the coordinates of the beam center. The pulse of interest at the plane of the detector, $\tilde{E}(x,y,\omega)$, is retrieved by removing the spherical curvature of the reference pulse numerically, i.e. :

$$\tilde{E}(x,y,\omega) = \tilde{E}'(x,y,\omega) \exp\left(-i\sqrt{x^2+y^2+L^2}K(\omega)\right), \tag{2.43}$$

where L is the distance from the focus of the OAP to the CCD and $K(\omega)$ is the wavenumber. The respective signal pulse in the time domain is obtained via Fourier transforming $\tilde{E}(x,y,\omega)$ with respect to ω. Since the method requires taking images over many laser pulses, beam movements, fluctuations of the spectrum or the wavefront during that acquisition time are limiting the method, whereas beam intensity fluctuations can be accounted for, e.g. by integrating the signal of the CCD over time. Another limitation is given by fluctuations of the delay stepping. The self-referenced FTS method is intrinsic multishot-based, due to limited acquisition speed of the CCD. Therefore, the method cannot resolve single shot fluctuations of the spatio-temporal beam pattern.

The other large class of methods for spatio-temporal pulse characterization can be summarized as “frequency-resolved spatial measurement techniques” [Jol20]. One common member of this class of methods, representing an alternative to SRFTS for complete spatio-temporal pulse characterization, is given by the method “INSIGHT”, introduced next.

2.5.3 INSIGHT

As part of the class of frequency resolved spatial measurement techniques, INSIGHT – developed by [Bor18] – retrieves the spatial profile by obtaining a frequency-resolved spatial pattern of the beam. A scheme of the method is shown in Fig. 2.7.

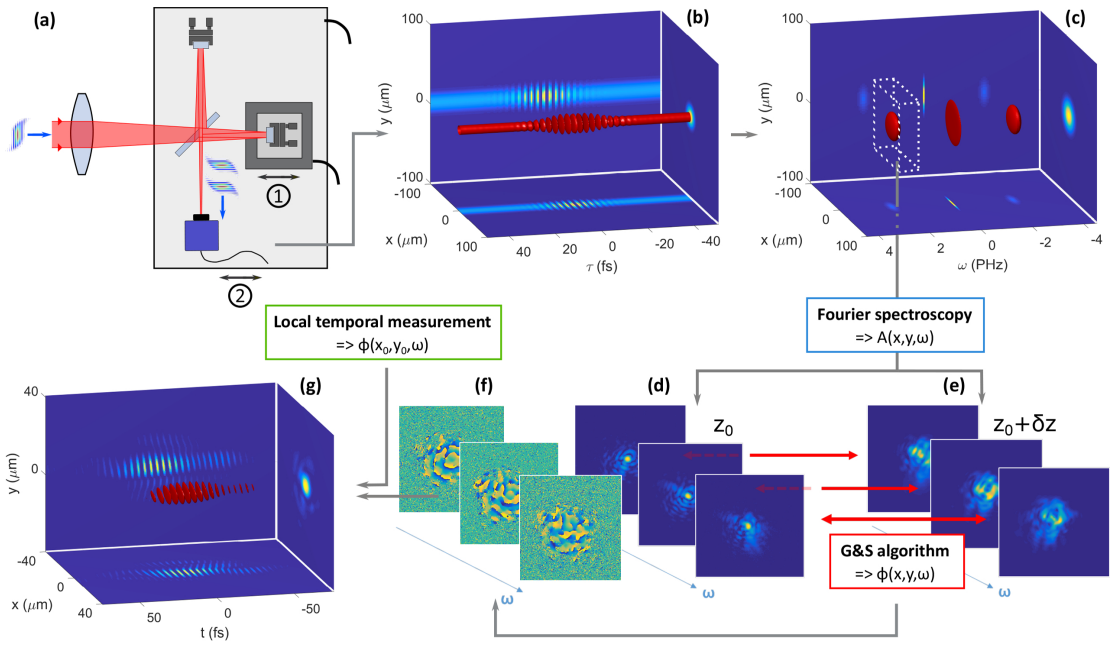

Figure 2.7: Principle scheme of the spatially resolved Fourier transform spectrometry method "INSIGHT". (a) A camera at the output of an interferometer records the inference pattern generated by the beam copies. Simultaneously, the non-interfered beam is recorded with a camera placed behind one of the end mirrors. From the delay scan one obtains a spatially resolved interference pattern per delay step (b). By Fourier transform with respect to time, the spatially resolved spectral amplitude profiles are obtained (c). Selecting the positive spectral frequencies only, the spectral amplitudes for every delay step are acquired (d). Shifting the whole interferometer, the whole recording process is repeated for every movement step δz of the interferometer around the focus position z_0 (e). With a retrieval algorithm, the spectral phase is extracted from the pulse amplitude (f). Real part of the final spatially-temporally resolved electric field (g). Reprinted with permission from [Bor18] © The Optical Society.

The beam of interest is split into two copies by a beam splitter in a Michelson or Mach-Zehnder type interferometer. Whereas in TERMITES the collimated beam is analyzed, in INSIGHT the beam focus and z-positions around the focus are analyzed by a camera sensor at the output port of the interferometer. One end mirror is tunable so that the delay between the two arms, i.e. the delay between the pulse copies, can be tuned. FTS is performed by measuring the spatial interference pattern between the two pulse copies for every delay step, resulting in an interferogram per pixel of the camera sensor. Via Fourier transforming the interferogram with respect to time, the pulse spectrum per pixel, thus spatially resolved over the pulse profile, is obtained. By only selecting the positive frequencies in the spectrum, the spatially-resolved spectral amplitude profile of the beam is retrieved. The spectral phase distribution with respect to an unknown reference phase, necessary for a complete characterization, is acquired by moving the whole interferometric setup along the beam direction z by steps of δz, around the focus position z_0, and repeating the acquisition of the spatial spatially-resolved spectral amplitude for each step. If the spectral phase at one arbitrary spatial position of the beam is additionally measured by means of another method, this phase serves as the reference and the full spatio-spectral profile of the beam can be retrieved. The INSIGHT method has the advantage of having a very compact setup while, due to the in-focus recording of the spatio-temporal beam profile, only a very small camera sensor is required. Furthermore, since laser-matter experiments are usually performed at the focus position, with INSIGHT one measures the spatio-temporal beam profile at the most interesting position for experiments. The disadvantage of this method is given by the required focusing of the incident beam by a lens or, alternatively, by a focusing mirror. The focusing lens needs to be aligned very accurately with respect to the incident beam because any tilt or decentration from the optical axis of the lens would add additional beam distortions on the pulse of interest that could not be distinguished from the inherent beam distortions one wants to detect with this method. Similarly, a focusing mirror will always have a slight tilt to the optical axis and therefore cause additional astigmatism on the pulse of interest that can only be completely removed numerically, if the exact tilt and curvature of the mirror are known. Therefore, SRFTS is preferred for the complete spatio-temporal characterization of a femtosecond filament along its length

presented in this work because filament pulses can inhibit complex STCs that shall not be covered by any additional distortion caused by the characterization setup itself.

In summary, both presented spatio-temporal pulse characterization techniques are able to fully characterize an ultrashort laser pulse spatio-temporally, i.e they are complete characterization methods. They require additional knowledge about the amplitude and phase (SRFTS) or only the phase of a reference pulse (INSIGHT). Hence, both require an additional measurement by a solely temporal pulse characterization technique. In the following, a brief introduction into temporal pulse characterization techniques is given, introducing FROG and d-scan as these have been the techniques used in the experiments of this thesis.

2.5.4 Temporal pulse characterization techniques

The first widely established pulse characterization technique has been the autocorrelator [Mai66; Gio67; Sha77]. Autocorrelation is a simple and well understood pulse characterization technique and therefore still regularly used in ultrafast laser optics to characterize optical laser pulses. However, it is not a complete method, i.e. it does not retrieve the pulse's phase and amplitude profile and requires assumptions, such as the assumed pulse shape or the symmetry of the pulse profile, so that a pulse duration can be retrieved.

Since the development of the autocorrelation technique, many more advanced techniques such as FROG [Kan93b; Kan93a; Tre97; O'S01; Bat10], SPIDER [Iac98; Gal99; Mai05; Rad07; Mah15], MIIPS [Loz04; Xu06; Coe08], or self-referenced spectral interferometry (SRSI) [Oks10], chirp scan [Lor13] and d-scan [Mir12a; Mir12b; Syt21] have been developed. Two of the most commonly used techniques, FROG and d-scan, used for the temporal characterization of the optical pulses in the experiments described in this thesis, are presented in the following.

Frequency-resolved optical gating

The "frequency-resolved optical gating (FROG)" technique [Kan93b; Kan93a; Tre97; O'S01; Bat10] developed from the autocorrelation technique. Whereas in the autocorrelation technique the SH (or nonlinear) signal intensity of two pulse copies is

measured as a function of delay, in a SH FROG it is their SH (or nonlinear) spectrum as a function of delay [Tre93; Kan93a; DeL94]. By a pulse retrieval algorithm - different algorithms for this task exist - a simulated FROG trace can be calculated and optimized, until it matches the measured one. If additionally the fundamental spectrum of the pulse is determined, the pulse can be reconstructed completely in phase and amplitude. A SH FROG trace has a direction-of-time ambiguity in the reconstructed pulse [Tre00]. From this ambiguity follows, that a pre- and a post-pulse cannot be distinguished from each other, neither can asymmetric pulse shapes be resolved. A SH FROG is applied as temporal pulse characterization method in the experiment on the determination of the plasma lifetime via TH enhancement, presented in Chapter 3. There are many different FROG versions such as the TH FROG [Tsa96], the self-diffraction (SD) FROG [Kan93a; Cle95], polarization-gate (PG) FROG [Kan93b; Tre93; DeL94] or the transient-grating (TG) FROG [Swe97] that do not possess temporal ambiguity. However, all FROG techniques rely on the interaction of at least two pulses which need to be aligned. Beam overlap can be a non-trivial task and also lead to errors in the pulse retrieval, especially if very short laser pulses of sub-10 fs, being prone to STCs, need to be retrieved. Hence, optimally, a pulse characterization technique should not need beam overlap and only require a single beam for the characterization. The d-scan technique [Mir12a; Mir12b] fulfills this requirement and has become, also due to its ease of use, a widely used pulse characterization technique. It is used for the additional temporal pulse characterization in the spatio-temporal analysis of a femtosecond filament along its length presented in Chapter 4 and is presented in the following.

2.5.5 Dispersion scan

Dispersion scan is a single-beam pulse characterization technique for ultrashort laser pulses in the femtosecond regime developed by Miranda *et al.* [Mir12a; Mir12b]. Several versions of the d-scan technique such as TH d-scan [Sil13; Hof14], crossed-polarized wave (XPW) d-scan [Taj16], SD d-scan [Can17], or single-shot d-scan [Fab15; Lou17; Sil17] already exist. The scheme for a basic SH d-scan setup, used in this thesis, can be see in Fig. 2.8.

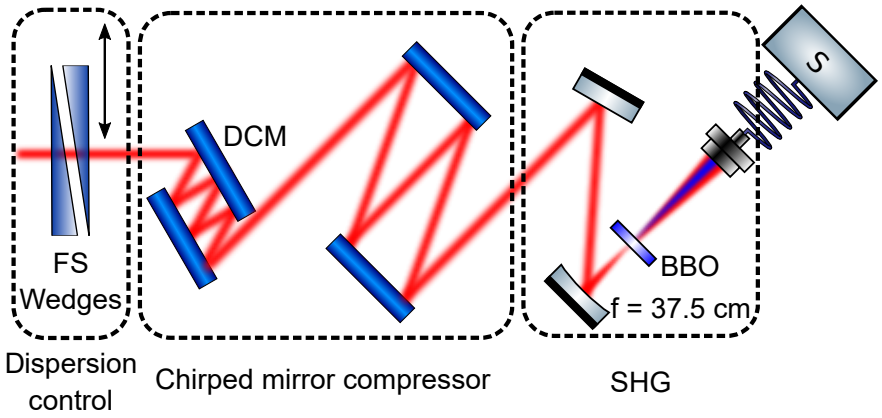

Figure 2.8: SH dispersion scan setup. The incident beam is sent onto a glass wedge pair (W) that can be moved transversal to the beam propagation direction. The beam then propagates through a double chirped mirror (DCM) pair and is subsequently focused onto a nonlinear crystal (here a barium borate (BBO) crystal) with a concave silver mirror (CSM, $f = 37.5\,\text{mm}$) to generate the SH. The SH is sent into a fiber-based optical spectrometer. Adapted with permission from [Neo22] © The Optical Society.

The incident beam is sent onto a glass wedge pair mounted on a motorized translation stage which moves the wedges transversely with respect to the beam direction. By inserting the wedges into the beam path, additional dispersion is introduced. If the incident pulse is defined as $\tilde{E}_{\text{in}}(\omega) = \left|\tilde{E}_{\text{in}}(\omega)\right| \exp\left(i\phi(\omega)\right)$, the pulse is positively chirped by the wedges by an additional phase term:

$$\Delta\phi_{\text{disp}}(\omega,z) = \frac{\omega n(\omega)}{c} z = k(\omega) z, \tag{2.44}$$

with the amount of dispersion depending on the inserted wedge material thickness z. After having passed the glass wedges, the beam is negatively chirped by multiple reflections on the DCMs. Every reflection introduces a fixed amount of negative dispersion to the beam. The total amount of negative dispersion depends on the amount of reflections on the DCMs. Due to manufacturing and performance reasons, DCMs are designed in a way that every reflection introduces strong oscillations in the second derivative of the spectral phase, the group delay dispersion (GDD). However, since the other mirror of the DCM pair introduces oscillations of opposite phase

with respect to the first one, nearly all oscillations are effectively suppressed, if equal numbers of reflections on both mirrors are used. Since by the DCMs only integer amounts of dispersion can be introduced, the continuously tunable amount of wedge thickness is chosen so that the overall dispersion of the pulse is balanced around the zero point. A d-scan trace is recorded by tuning the dispersion from negative to positive (or vice versa) by inserting equal amounts of glass thickness while recording the SH spectrum for every insertion step. An example of a d-scan trace from the spatio-temporal characterization experiment of the filament is illustrated in Fig. 2.9. The trace possesses complex features which indicates that the pulse is not Fourier limited, i.e. the pulse does not have a flat spectral phase. This example shows that rough information about the pulse characteristics can be obtained already from the d-scan trace itself: the shorter a pulse, the narrower is its width on the dispersion axis of the trace and the broader is its spectral width. A pulse that is negatively or positively chirped in the second order derivative of the spectral phase, the GDD, is offset from the relative zero position of glass insertion along the dispersion axis. The group delay (GD) does not affect the d-scan trace. A pulse with third-order dispersion (TOD), generates a trace that is tilted with respect to wavelength axis. A positively chirped pulse is tilted upwards and a negatively chirped pulse is tilted downwards. GDD and TOD can also exist together and cause a shift and a tilt. Additionally, to the dispersion scan, the fundamental spectrum of the pulse is recorded. In order to retrieve the pulse phase from the d-scan trace, a retrieval algorithm run, starting with a guessed phase, is conducted. From the retrieval a simulated d-scan trace is calculated. Via a minimization parameter μ:

$$\mu = \frac{\sum_{i,j} S_{\mathrm{meas}}(\omega_i,z_j) S_{\mathrm{sim}}(\omega_i,z_j)}{\sum_{i,j} S_{\mathrm{sim}}(\omega_i,z_j)^2}, \tag{2.45}$$

the simulated d-scan trace S_{sim} is compared to the measured one S_{meas}. In several iterations, the retrieval tries to minimize μ. When a minimal difference is found, the pulse phase is retrieved and the laser pulse is completely characterized. D-scan does not require any assumptions on the pulse and is not possessing the temporal ambiguity of the SH FROG. Therefore, it is a complete characterization method, able

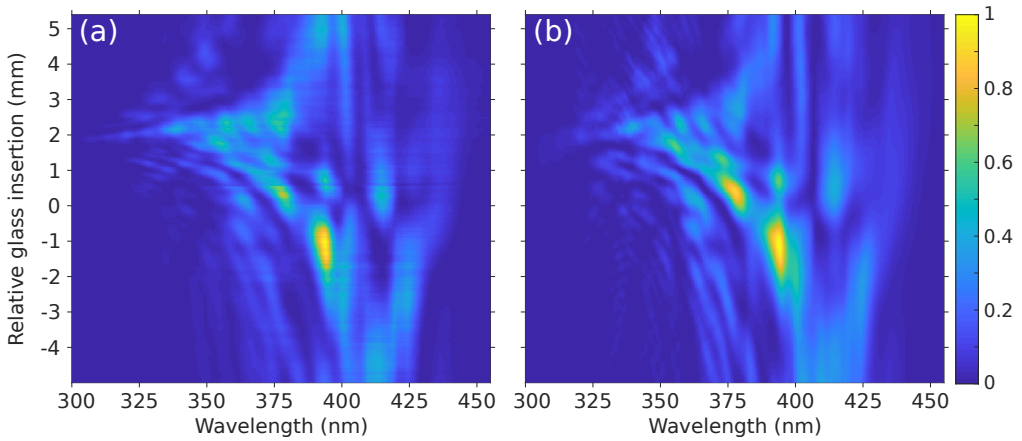

Figure 2.9: SH d-scan traces of the filament pulse at position d = 150 mm of the experiment in Chapter 4, belonging to a sub-10 fs pulse. (a) measured trace, (b) retrieved trace from the d-scan algorithm. The y-axis denotes the relative wedge insertion in mm and the x-axis the wavelength in nm.

to characterize all pulse features, i.e. also asymmetric pulse shapes. The common d-scan setups are inherently multi-shot pulse characterization setups, since the acquisition time of a SH spectrum takes longer than the usual repetition rate of the laser used in the experiment. However, as mentioned above, single-shot d-scan setup already exist. For the experiment presented in this thesis, the most common d-scan setup, the SH d-scan, was chosen since it is a well understood setup and has high enough detection efficiency and spectral detection width necessary for the experiment.

CHAPTER 3

Determination of the temporal plasma evolution via TH enhancement

In this chapter, the experiment about the temporal plasma evolution via TH enhancement in gaseous media is presented and its results discussed. It begins with an introduction into the experimental setup as well as its procedure and principle. It is followed by a presentation of the plasma lifetime measurements and a discussion of the results. In the last part, observations about the onset of TH enhancement are presented and discussed.

3.1 Experimental setup, procedure and principle

In this section, the experimental setup and procedure are presented, including a typical measurement trace and the data processing to retrieve the experimental data.

3.1.1 Experimental setup

Laser system

The laser system for this experiment is a customized commercial titanium-sapphire amplifier system (Dragon, KMLabs Inc.), based on the CPA technique. A titanium-sapphire oscillator emits 10 fs pulses with a central wavelength of 790 nm and a pulse energy of 1.8 nJ. In a grating-based pulse stretcher, the pulse is stretched to about 200 ps and then enters a Pockels cell surrounded by two polarizers, one before and one after the cell, with orthogonal orientation to each other. The Pockels cell is triggered to the oscillator output and rotates the polarization of the incident beam by $\pi/2$. Only when the polarization of the incident beam is changed by the cell,

it passes a second polarizer and enters the ensuing multi-pass amplification stage. In that way the repetition rate is reduced to 1 kHz. The titanium-sapphire-based amplification stage is pumped by a ns pump laser with a central wavelength of 527 nm and a pulse energy of 40 mJ (Ascend 60, Spectra-Physics). In this stage, the infrared pulse can be amplified up to 2 mJ, but the amplifier is usually only operated at 1 mJ, corresponding to an amplification factor of 10^6. The amplifier stage is followed by a grating compressor in which the pulse is compressed to 35 fs. With an adjustable attenuator, the power of the amplifier system can be varied between about 2 % and 100 %. After the attenuator, the beam is sent to an imaging setup, cleaning the beam profile by imaging a position within the amplifier with an optimized beam profile. The final output beam has a M^2-value of $M^2 = 1.6$ in one axis and $M^2 = 1.8$ in the other axis with a diameter ($1/e^2$) of 6.4 mm.

Setup

The experimental setup for the temporal plasma evolution study via TH enhancement is shown in Fig. 3.1. From the attenuator, the beam is split into two arms, the "pump arm" and the "signal arm", by a beam splitter plate. With the $\lambda/2$-waveplate in front of the beam splitter plate, the power distribution between the two arms can be adjusted. In the pump arm, the beam is sent to a retroreflector positioned on a one-axis translation stage (Newport, M-UTM150CC.1) to adjust the temporal delay between the arms. The translation stage has a total scan range of 150 mm and is computer-controlled via a motion controller and driver (Newport, ESP300). Initially, for temporal scans, a range of 6.64 cm, corresponding to 443 ps was available. Later, for long temporal scans of the noble gases argon and helium, the setup was modified so that the translation stage can be shifted in steps of 127 mm, enabling a total temporal scan window of 5076 ps (see Sec. 3.2.3). The minimal step size for the experiment corresponds to 4 fs. The actual step size for any scan is chosen with respect to the total temporal window of the scan, in order to keep the total scan time at around 15 min up to 30 min. After the retroreflector, the beam passes a $\lambda/2$-waveplate and a calcite polarizer. The waveplate is mounted on a computer-controlled rotational motion controller (8MR151-30, Standa). By rotating the waveplate with respect to the polarizer, the power in the arm can be adjusted. The calcite polarizer

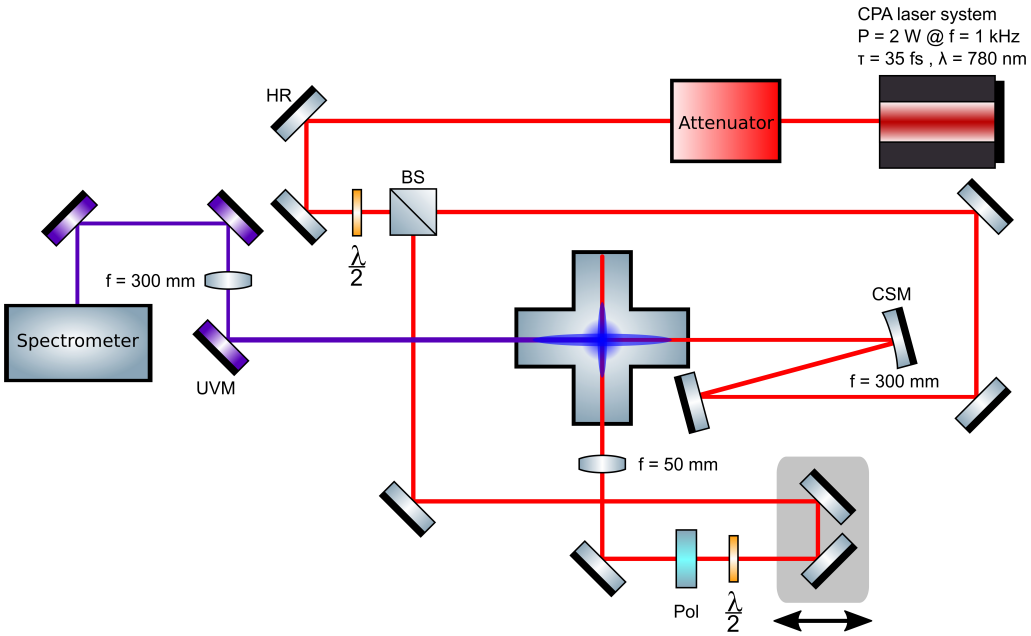

Figure 3.1: Scheme of the experimental setup. The cross in the image center represents the chamber which can be filled with gas. The beams cross at an angle of 90° and interact in the overlap volume. The generated UV-light (in purple-blue) is separated from the fundamental light, refocused and sent to a spectrometer. HR: high-reflective mirror for 780 nm, BS: beam splitter, Pol: polarizer, CSM: concave silver mirror, UVM: dichroic mirror, high-reflective for 260 nm and high-transmissive for 780 nm. Reprinted with permission from [Jus19] © The Optical Society.

chirps the pulse to about 80 fs and is set to transmit p-polarized light in its normal configuration. After the polarizer, the beam is focused with a lens of $f = 50\,\mathrm{mm}$ into a chamber, filled with the gas of interest, generating a mm long plasma string, e.g. about 3 mm in air atmosphere at ambient pressure. For measurements, the usual power in this arm is 0.5 W. In the signal arm, the beam is sent to a focusing mirror with $f = 300\,\mathrm{mm}$ creating a filament with a length of approximately 4 cm in air. The filament crosses the plasma string at an angle of 90°, minimizing the overlap volume and thus the plasma absorption of the fundamental and TH radiation from the filament. The plasma severely enhances TH from the filament by the process described in Sec. 2.4.8. The chamber is equipped with 2 mm fused silica windows on the entrance side of the filament and the plasma string and a 2 mm MgF_2 window on the filament exit side to optimize the TH transmission out of

the chamber. The generated TH propagates collinearly with the fundamental to the dichroic mirrors. These mirrors have a high reflectivity for the TH at around 260 nm and a high transmission for the fundamental at around 780 nm. With every consequent reflection on a dichroic mirror, the contrast between the TH and the fundamental is increased so that both signals can be measured simultaneously with the spectrometer (HR4000CG-UV-NIR, Ocean Optics), despite the fundamental being far more intense at the chamber output. Since the generated TH is divergent, it is refocused by a lens ($f = 300\,\mathrm{mm}$) and enters the spectrometer via free-space propagation to avoid a signal decrease by the propagation through a fiber, which generally has a low transmission in the UV. For measurements, the usual power in the signal arm is 0.3 W.

3.1.2 Experimental procedure

For initial alignment, the chamber is evacuated and subsequently filled with about 1.1 bar of argon. The pump and signal beams are aligned so that they overlap spatially in the center of the chamber. Filling the chamber with argon severely helps to find the temporal overlap, since its plasma has a lifetime of more than 1 ns, as it is shown later in this chapter. Note that the plasma lifetime can be defined arbitrarily. Here, plasma lifetime is defined as the time it takes for the plasma density to decrease from the maximum density to $1/e$ of that density. A plasma lifetime in the ns range implies a temporal overlap of at least 30 cm which extremely simplifies to find the spatio-temporal overlap. Once the zero delay position of the translation stage is found – the position for which both arms have the same optical path length – one switches to the gas of interest. For all gases, except air which is investigated at ambient pressure, a pressure of about 1.1 bar is used in order to guarantee that the chamber is kept free from outside contamination. Then, the spatial and temporal overlap is fine-optimized with the focusing mirror in the signal arm because the best alignment for the new gas can slightly deviate from the best alignment for argon. When the best alignment is set, the TH is aligned into the spectrometer. Via a computer script, the step size and length of the scan as well as the scan speed is set. The script controls the translation stage and the readout of the spectrometer, automatically. For every step of the translation stage, the spectrometer records a spectrum. When it is saved, the procedure repeats until the end of the scan.

3.1.3 Experimental principle

Filaments that are intercepted by laser-induced plasma show a significant increase in THG, i.e. the TH is strongly enhanced by the plasma, compared to an undisturbed filament, as mentioned earlier in Sec 2.4.8. Fig. 3.2 shows the difference between the measured TH signal of the undisturbed air filament at ambient pressure compared to the TH signal from the same filament intercepted by plasma from the pump arm.

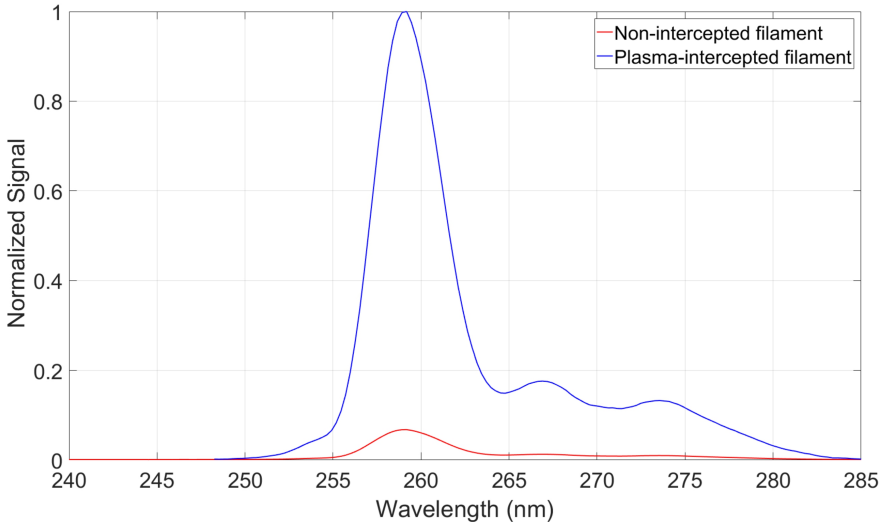

Figure 3.2: TH signal from a femtosecond filament in air at ambient pressure as a function of the wavelength. Presented in red is the TH signal from the unperturbed filament and shown in blue is the signal from the filament intercepted by plasma. The TH emission from the unperturbed filament is magnified by a factor of 15 for better visualization. The enhancement factor is estimated to be around 375. Reprinted with permission from [Jus19] © The Optical Society.

This comparison clearly shows that the TH signal is strongly enhanced when the filament is intercepted by laser-induced plasma. For any investigated gas, an enhancement factor of about 300 was observed. This factor is in accordance with other experiments about plasma-induced TH enhancement in filaments which usually report absolute enhancement factors in the range of two orders of magnitude [Sun09; Sun10; Liu11; Gry17]. As described in Sec. 2.4.8, the TH enhancement follows the temporal plasma evolution. Hence, when the TH signal from the filament is measured as a function of delay, the temporal behaviour of the plasma density in the pump

arm is studied simultaneously. However, it has to be noted, that no statements about the absolute plasma density but only about the temporal trend of the relative plasma density can be given. To the best of the author's knowledge, it is a quite unique property of this method, that the temporal evolution of the plasma density is directly imprinted in the measurement signal. Fig. 3.3 shows an exemplary temporal trace of the spectrally resolved TH from a femtosecond filament in air, and in that way also of the relative plasma density, as a function of the delay between the pump generating the plasma string and the filament beam in the probe arm.

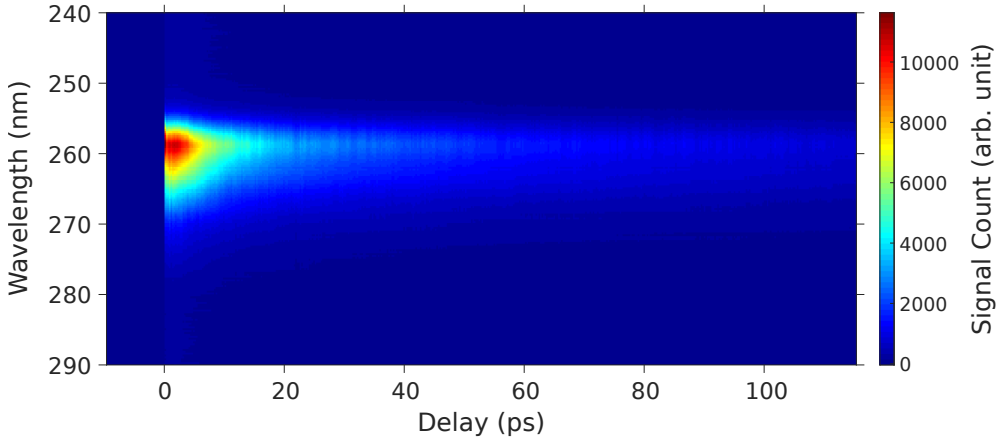

Figure 3.3: Spectrally resolved TH signal of an air filament at ambient pressure as a function of delay between the pump and the filament pulse. Adapted with permission from [Jus19] © The Optical Society.

Here, positive delay is defined as the pump pulse arriving earlier than the filament pulse and negative delay vice versa. Fig. 3.3 exemplarily shows that the TH spectrum is not affected by the plasma interception. This statement remains correct for all other investigated gases, too. Since the TH spectrum is not affected by the plasma from the pump, the measurement data representation can be simplified by integrating the TH signal over the spectral domain. Fig. 3.4 shows the same experimental data than in Fig. 3.3, integrated over the spectral domain. The obtained temporal TH traces for air resemble the ones observed in [Sun09; Yao12; Jar14], showing a good agreement of this method with established ones. The TH signal reaches its maximum shortly after zero delay. From there, it decays rapidly in a nearly exponential manner

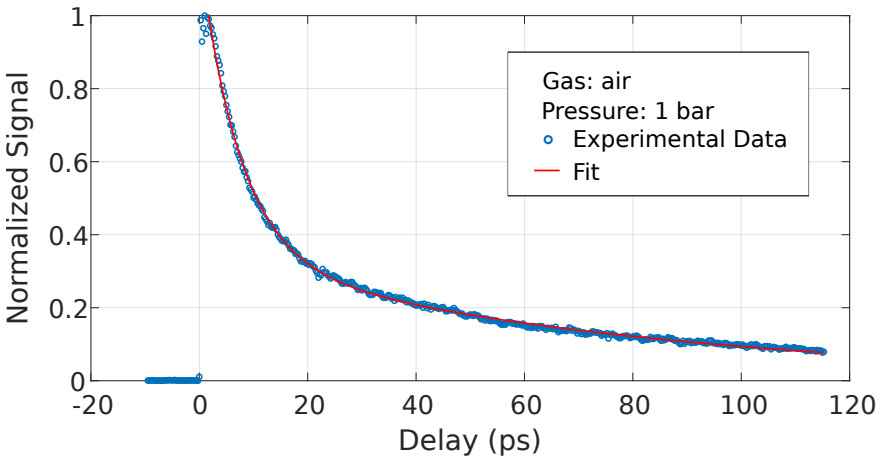

Figure 3.4: Spectrally integrated TH signal of an air filament at ambient pressure as a function of delay between the pump and the filament pulse. The line in red represents a regression fit to the experimental data. The trace is normalized with respect to the maximum TH signal. Adapted with permission from [Jus19] © The Optical Society.

and reaches $1/e$, so its plasma lifetime, after around 14 ps. In order to have an estimate on the uncertainty of the measured TH signals, the measurement for air was repeated ten times and the plasma lifetime showed a standard deviation of about 8.6 % from the average value. Therefore, the method gives reliable information about the plasma lifetime of the investigated gases. For simplification, the traces of all the other investigated gases, shown in the following Section 3.2, are displayed in the spectrally integrated representation as well.

3.2 Experimental results

In this section, an investigation of the influence of several experimental parameters on the plasma decay is presented, followed by an analysis of the plasma lifetime in the invested atomic and molecular gases helium (He), argon (Ar), xenon (Xe), carbon dioxide (CO_2), (molecular) nitrogen (N_2) and air.

3.2.1 Parameter study

The performed parameter study comprises the laser pulse energy, beam polarization, pulse duration, and gas pressure and begins with the parameter pulse energy. Note

that the studies in air atmosphere are shown for all parameters. The figures of the decay studies in the other gases are only presented here, when a significant change in the plasma decay with respect to the parameter can be observed. Otherwise, the respective figure is moved to Chapter A in the appendix.

Pulse energy

For the pulse energy study, the power of the pump arm was tuned by means of rotating the $\lambda/2$-waveplate with respect to the polarizer. The power of the signal arm was kept constant. The scans performed in the molecular gases were carried out with a temporal stepping of 0.25 ps and the ones in the atomic gases with a temporal stepping of 1 ps. The study comprises the gases air, nitrogen, and carbon dioxide as well as the rare gases argon and xenon. In Fig. 3.5, the pulse energy study for air is shown.

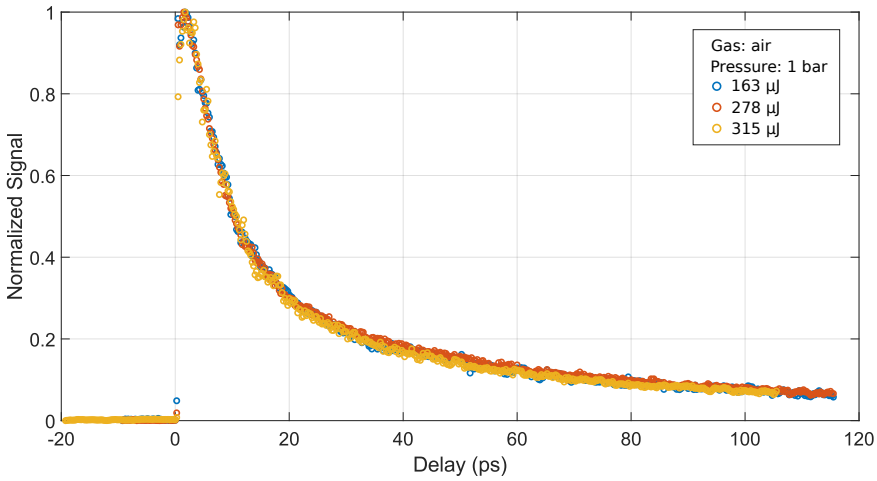

Figure 3.5: Normalized temporal TH evolution signal for different pump pulse energies in air measured at 1 bar.

The variation of the pump pulse energy is not affecting the temporal TH evolution signal in air. All traces are nearly identical. The same behaviour can be observed in the pump pulse energy study of carbon dioxide, shown in Fig. A.1. In case of nitrogen, shown in Fig. A.2, an insignificant variation of the temporal evolution is visible for a pump pulse energy of 174 µJ, after the signal dropped lower than $1/e$.

The deviation is in the uncertainty range of the experimental method. For the pump pulse energy study in argon, shown in Fig. 3.6, a stronger variation of the temporal TH evolution for the lowest studied pulse energy of 92 µJ compared to the temporal evolution for the higher pump pulse energies of 129 µJ and 146 µJ can be observed.

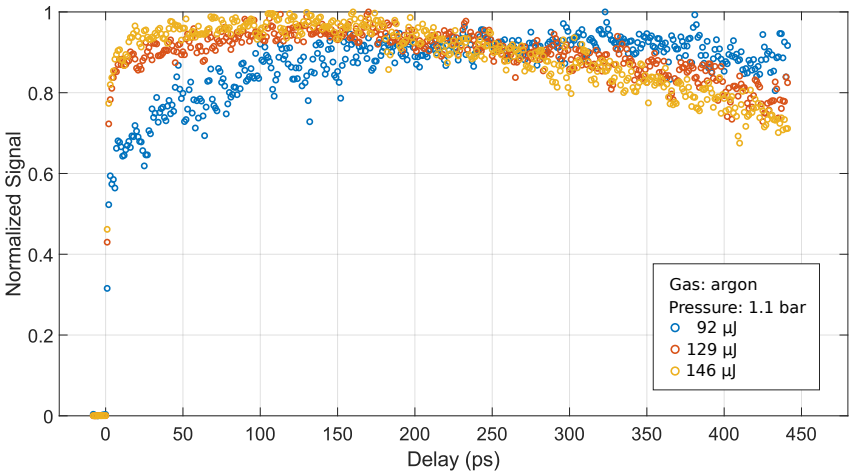

Figure 3.6: Normalized temporal TH evolution signal for different pump pulse energies in argon measured at 1.1 bar.

The signal for 92 µJ is rising slower towards the maximum than the other two, but then stays at the maximum for the whole scan range of 441 ps. Due to this observation, the other temporal scans of the argon plasma were performed at 146 µJ, for which no deviation in the temporal trends is observed. In case of xenon – pump pulse energy study in Fig. A.3 – the trend is comparable to the molecular gases, i.e. no significant deviation with respect to the pump pulse energy can be observed.

Overall it can be summarized that tuning the pump pulse energy does not lead to a different temporal TH evolution. Although, the investigations in nitrogen and argon show some insignificant deviations for some pump pulse energies, tuning of the pump pulse energy in the presented range is not significantly affecting the TH evolution in the two gases. Hence, it is possible to compare measurements for different gases, obtained at different pump pulse energies. Varying the pump pulse energy in the investigated range only affects the absolute magnitude of TH enhancement caused by different absolute plasma densities. However, it does not affect the temporal trend of the plasma.

Polarization

For the investigation of the polarization dependency, the orientation of the polarizer in the pump arm was changed from p-polarization to s-polarization so that the two arms of the setup possess orthogonal polarization. Besides the different orientation of the polarizer, the measurements were conducted in the same way than previously explained in Sec. 3.1.2. The results for the new orientation are compared to plasma lifetime measurements conducted in the normal orientation of the polarizer. This investigation was performed for laser-induced plasma in air, carbon dioxide and nitrogen as shown in Fig. 3.7, Fig. A.4 and Fig. A.5.

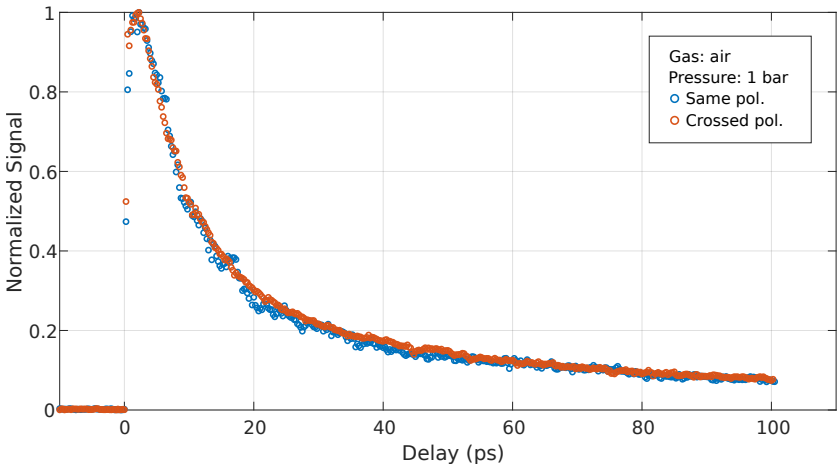

Figure 3.7: Normalized temporal TH evolution signal for different pump beam polarization states with respect to the probe beam in air measured at 1 bar.

For neither of the three gases any dependency of the plasma lifetime on the polarization of the pump is found. It is expected that the independence of the temporal plasma evolution on the pump polarization for the investigated gases air, carbon dioxide and nitrogen also applies to the non-investigated gases of this study such as the atomic gases.

Pulse duration

The pulse duration in the pump arm was set to 80 fs, the usual pulse duration for all the measurements with this setup, and 35 fs, by removing the calcite polarizer. Since, without the polarizer the pulse energy cannot be varied, a scan with the polarizer

was performed solely at maximum pump pulse energy. The measurement comprised all investigated gases, i.e. the molecular gases air, carbon dioxide and nitrogen as well as the atomic gases helium, argon and xenon. The measurement in air atmosphere can be seen in Fig 3.8.

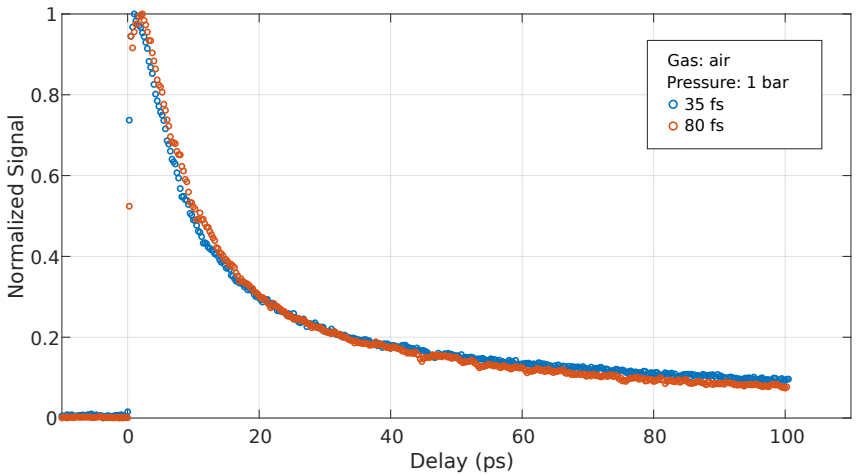

Figure 3.8: Normalized temporal TH evolution signal for different pump pulse durations in air measured at 1 bar. The traces are normalized to the maxima of the signals.

The temporal trends for the different pump pulse durations are nearly identical in air. In carbon dioxide, Fig. 3.9, a slight variation of the temporal evolution can be observed for the different pump pulse durations. The plasma generated from the longer pump pulse decays slower than the plasma of the shorter pulse. In case of nitrogen, illustrated in Fig. A.6, the traces for both pump pulse durations are nearly identical until the TH signals drop to lower than $1/e$. From there, the plasma of the shorter pulse seems to decay slightly slower than the long pulse. Nonetheless, the difference between the traces is not large and could be explained by measurement uncertainties. In summary, there is no clear evidence for a dependency of the temporal plasma evolution on the pump pulse duration in the molecular gases.

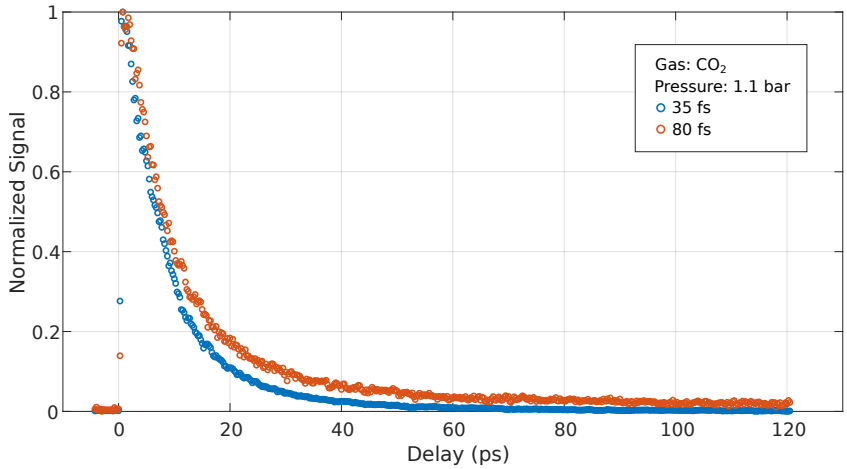

Figure 3.9: Normalized temporal TH evolution signal for different pump pulse durations in carbon dioxide measured at 1.1 bar. The traces are normalized to the maxima of the signals.

The measurement in the atomic gas helium is shown in Fig. 3.10.

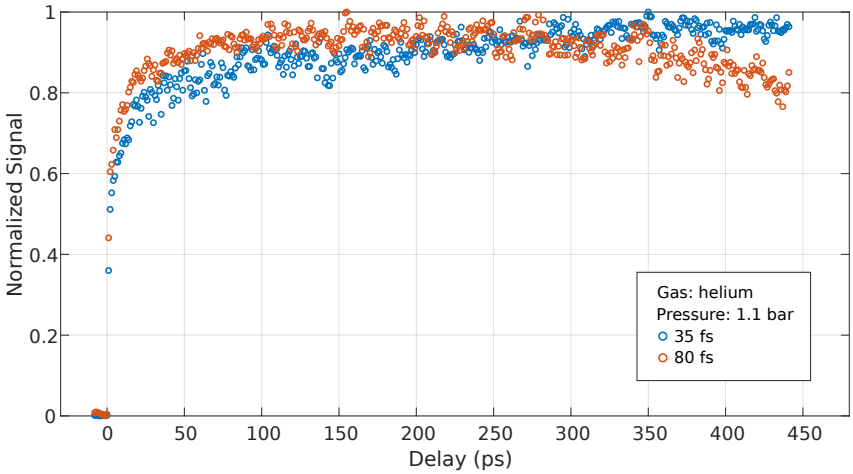

Figure 3.10: Normalized temporal TH evolution signal for different pump pulse durations in helium measured at 1.1 bar. The traces are normalized to the maxima of the signals.

The TH signal of the 35 fs long pump pulse rises slower than the TH signal of the 80 fs long one and reaches its maximum at the end of the scan range, whereas the signal for the long pulse rises quicker but reaches its maximum at a delay of around

225 ps and slowly decays from there on. Note, that the decay likely is a measurement artefact because later investigations in helium atmosphere with longer scan ranges showed no decay in that scan range. The measurement in argon is illustrated in Fig. 3.11.

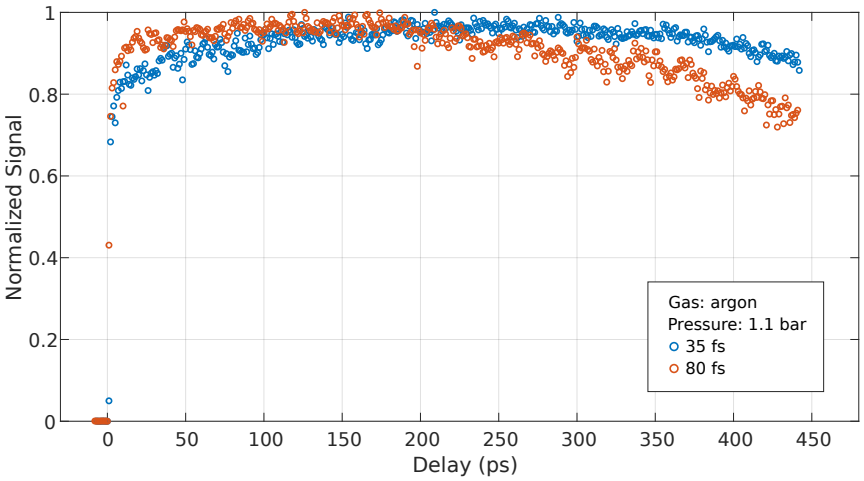

Figure 3.11: Normalized temporal TH evolution signal as a function of the pump pulse duration in argon measured at 1.1 bar. The traces are normalized to the maxima of the signals.

Its plasma shows a similar trend to the helium plasma. The trace of the long pulse rises faster but also decays earlier compared to the trace of the short pulse. Whereas the trace of the long pulse reaches its maximum at around 160 ps, the trace of the short pulse reaches its maximum after around 250 ps. The measurement for xenon can be seen in Fig. A.7. The trend for xenon does not match the trend of helium and argon. The TH traces for both pump pulse durations are identical within the noise level of the measurement. In summary, as for the measurements in the molecular gases, there is no clear evidence that the plasma evolution in the atomic gases depends on the pump pulse duration. This finding is in accordance with the expectation, as the pulse durations are very similar and in terms of intensity, 8.3 $\mathrm{PW/cm^2}$ and 3.6 $\mathrm{PW/cm^2}$ is estimated in the focus for the argon plasma for a pulse duration of 35 fs and 80 fs, respectively, with a pulse energy of 160 µJ, disregarding plasma defocusing. Thus, the ionization dynamics for both pulse durations take place in the strong field

regime of ultrashort laser pulses. A severely different plasma dynamic would be expected for ionizing pulses in the ns range, where the ionization is dominated by particle collision events.

Hence, it can be summarized for all investigated gases that it cannot be said with confidence whether there is a dependency of the temporal plasma evolution on the pump pulse duration. Since for all other measurements, reported in the following, the pump pulse duration was fixed to 80 fs, the lifetime measurement results can be compared nonetheless.

Gas pressure

The gas pressure in air was varied between 0.5 bar and 1.0 bar in steps of 0.1 bar. For every pressure, the TH enhancement was measured as a function of delay. The measurement is visible in Fig. 3.12.

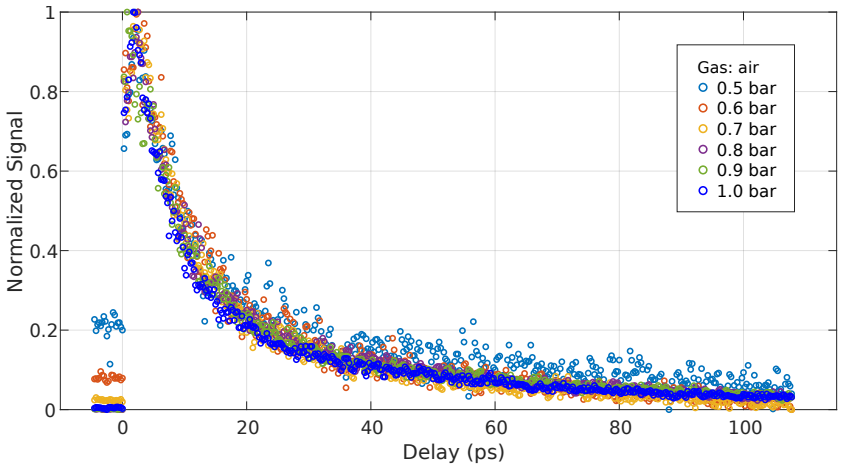

Figure 3.12: Normalized temporal TH evolution signal for different gas pressures of 0.1 bar from 0.5 bar to 1.0 bar in air. The traces are normalized to the maxima of the signals.

The traces for the different pressure levels show no significant difference in their temporal behaviour. Thus, it is concluded that the gas pressure is not significantly affecting the plasma lifetime of air in the investigated pressure range. For the measurements of lower pressure, i.e. from 0.5 bar until 0.7 bar, the TH traces do not start at zero enhancement for negative delays, as expected. In fact, at delays

greater than 80 ps, the TH signals of these three measurements drop lower than for negative delays. It is assumed that this behaviour is not real and is a measurement artefact caused by the low TH signal at these pressure levels, enhancing inherent measurement noise. Overall it can be summarized, that the gas pressure has no significant effect on the temporal plasma evolution in the investigated pressure range. It is assumed, that this behaviour is valid for all investigated gases, making the measurements between gases obtained at different pressure levels comparable to each other.

In the following, the experimental results for plasma lifetime measurements of the atomic and molecular gases will be presented, starting with the results for the case of the molecular gases.

3.2.2 Plasma lifetime of the molecular gases

The investigation of the plasma lifetime in molecular gases comprises air, nitrogen and carbon dioxide. Whereas nitrogen and carbon dioxide are purely molecular gases, air is a gas mixture, mostly containing the molecular gases nitrogen, with about 78 % and oxygen with about 21 % [Bri96]. From its gas mix ratio, one would assume that the air plasma is dominated by the nitrogen contribution. However, it was shown that at intensities close to the clamping intensity of an air filament at around 50 TW/cm^2 [Kas00], oxygen constitutes 80 % of the air plasma, thus being its major plasma constituent [Fay01], as it is more easily ionized than nitrogen. Therefore, the plasma lifetime in air atmosphere should in fact deviate from the plasma lifetime in molecular nitrogen and be similar to the lifetime in molecular oxygen. In Fig. 3.13 the temporal plasma evolution in the molecular gases is shown. The plasma lifetime measurements in all three gases were performed with a temporal step size of 0.25 ps at a pressure level of 1.1 bar (carbon dioxide, nitrogen) and ambient pressure (air). Note that the gases did not have the same pressure level and also the pulse energy in pump and signal arm, stated in Tab. 3.1, was not the same for the measurements in the different gases. Nonetheless, as the parameter study in Sec. 3.2.1 verified no significant influence of the parameters pressure and pulse energy for the parameter window that was chosen for the experiments, the measurements can be compared. In all gases a sharp increase shortly after zero delay occurs followed by an exponential-

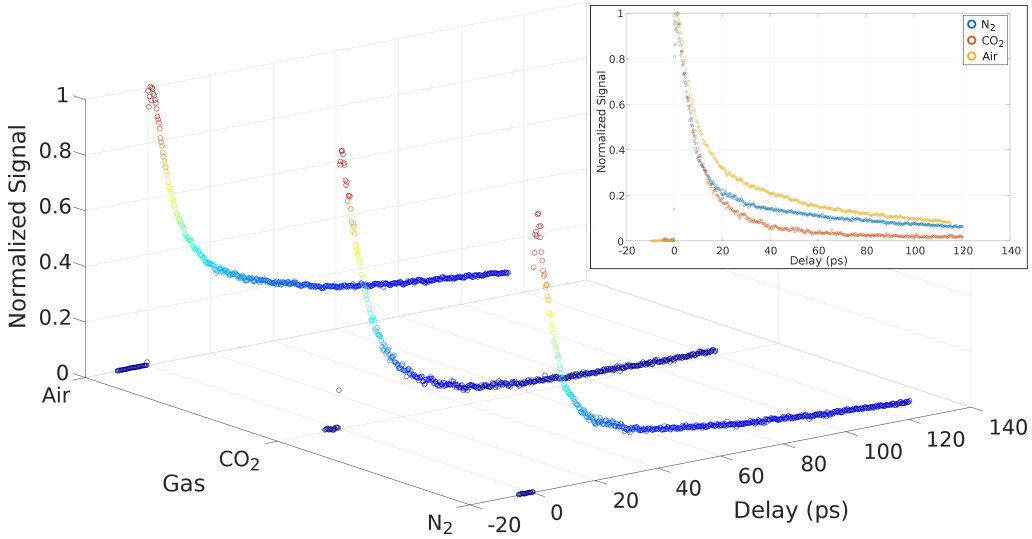

Figure 3.13: Temporal TH evolution signal of air at 1 bar and N_2 and CO_2 at 1.1 bar. The traces are normalized to the maxima of the signals. The x-axis shows denotes the gas type, the y-axis the delay in ps and the z-axis the normalized signal strength. Inset: two-dimensional representation of the plots. Reprinted with permission from [Jus19] © The Optical Society.

Table 3.1: Pulse energy in the pump and signal arm for plasma lifetime measurements in the molecular gases.

Gas	Pump pulse energy [µJ]	Signal pulse energy [µJ]
Air	315	573
CO_2	317	522
N_2	174	330

like rapid decay after reaching the maximum shortly after zero-delay. However, the decay time constants are different for the three gas media. The fastest decay is shown in N_2, with a lifetime of about 8.25 ps, followed by CO_2 with about 9.75 ps and air with 14 ps. As expected, the lifetime of air plasma differs significantly from the plasma lifetime in nitrogen atmosphere. Overall, in all molecular gases a quite rapid decay of their laser-induced plasma on a ps-time scale is observed, with air plasma having the longest lifetime with about 14 ps. In the following, the temporal plasma evolution of the atomic gases is shown.

3.2.3 Plasma lifetime of the atomic gases

The investigation of the atomic gases comprises the rare gases helium, argon and xenon. The temporal plasma evolution of the atomic gases is shown in Fig. 3.14. All three gases were measured with a temporal step size of 1 ps.

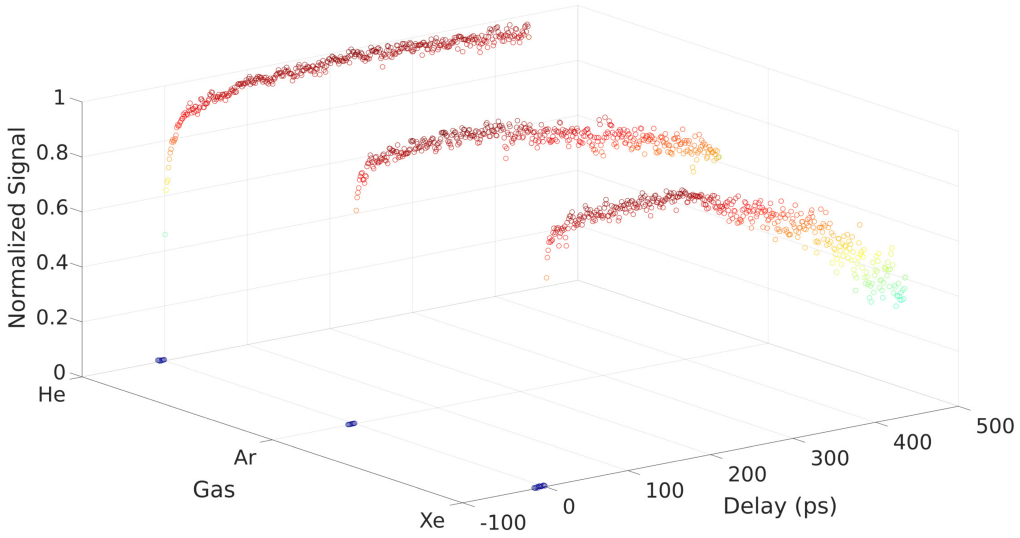

Figure 3.14: Temporal TH evolution signals of helium and argon at 1.1 bar as well as xenon at 0.5 bar. The traces are normalized to the maxima of the signals. The x-axis shows denotes the gas type, the y-axis the delay in ps and the z-axis the normalized signal strength. Reprinted with permission from [Jus19] © The Optical Society.

The measurements in the rare gases were performed at 1.1 bar (helium, argon) and 0.5 bar (xenon). Furthermore, the pulse energy in the pump and signal arm, stated in Tab. 3.2, varies for the three gases. The individual pulse energy settings were chosen for signal stability reasons.

Table 3.2: Pulse energy in the pump and signal arm for plasma lifetime measurements in the atomic gases.

Gas	Pump pulse energy [µJ]	Signal pulse energy [µJ]
Helium	316	580
Argon	146	256
Xenon	150	232

The temporal plasma evolution in the atomic gases clearly differs from the one in the molecular gases. An explanation for this finding is given in Sec 3.3. Whereas the plasma in the molecular gases decays in the ps-range, directly after having reached the maximum, the plasma in the atomic gases reaches a plateau after the maximum signal and does not decay for more than 100 ps. As a consequence, the measurements in the atomic gases are carried out in a longer temporal window of 441 ps compared to around 140 ps in the case of the molecular gases. However, this scan range is not large enough to cover completely their plasma decay. Whereas the xenon plasma reaches $1/e$ at the end of the scan range, with an estimated plasma lifetime of 443 ps, the argon and helium plasma do not decay fast enough to estimate their lifetimes. To determine the plasma lifetime in these gases, the setup has been modified to the long scan configuration mentioned in Sec. 3.1.1, with a total scan range of 5076 ps. In order to keep the total scan time in an acceptable range, the temporal step size was increased to 2 ps. The long scans in helium and argon plasma are displayed in Fig. 3.15. The respective pulse energies are stated in Tab. 3.3.

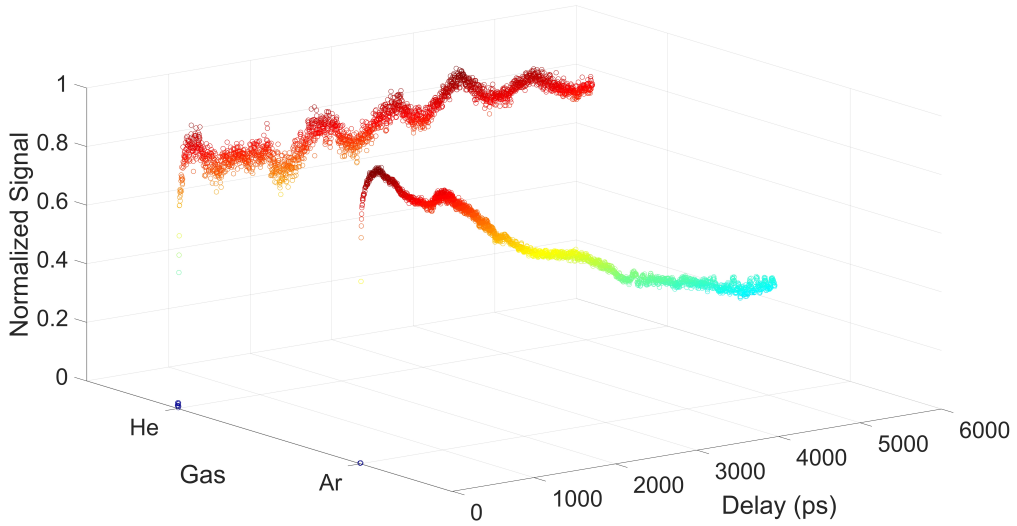

Figure 3.15: Long scans of the temporal TH evolution signals of helium and argon at 1.1 bar. The traces are normalized to the maxima of the signals. The x-axis shows denotes the gas type, the y-axis the delay in ps and the z-axis the normalized signal strength. Reprinted with permission from [Jus19] © The Optical Society.

Table 3.3: Pulse energy in the pump and signal arm for the extended plasma lifetime measurements in argon and helium.

Gas	Pump pulse energy [µJ]	Signal pulse energy [µJ]
Argon & Helium	283	576

In the long scan of argon plasma, a clear decay is visible and the lifetime is determined to 4543 ps. Therefore, argon plasma has a lifetime that is about 10 times longer than xenon plasma, which has a 32 times longer plasma lifetime than air plasma; the molecular gas plasma with the longest lifetime. It is quite remarkable, that helium still does not show any decay at all. The helium plasma lifetime must be much longer than a few ns. Unfortunately, due to technical reasons it was not possible, to cover such a long scan range experimentally.

The long scans in helium and argon, especially the one in helium, show some significant oscillations in the trace. These oscillations are not assumed to be real features of the temporal plasma evolution in the two gases. Similar oscillations could be reproduced, when the individual partial scans of the long scans in the two gases were repeated at certain positions. It was observed that the translation stage shows a non-constant movement in the vertical direction during a scan. The stage slightly moves up and down from one end of the stage to the other, which changes the overlap between the pump and the probe beam. This effect takes place for all scans since it is a property of the translation stage but it is more prominently displayed when the TH enhancement is low. In that case, the difference between a better and a worse overlap of pump and probe is magnified, compared to scans that are measured with a strong TH enhancement. Furthermore, power fluctuations also slightly affect the overall TH signal, leading to observable fluctuations in the case of low TH enhancement.

In summary, in the atomic gases the respective plasmas have a significantly longer lifetime than in the molecular gases with decay times in the ns range and helium plasma having the longest lifetime that even exceeds the maximal scan range. In the following, the observed differences in the plasma lifetimes between the atomic and the molecular gases as well as the differences in the lifetimes in between gases of the two groups is explained.

3.3 Analysis and discussion of the measured plasma lifetimes

The plasma lifetime of a gas can be affected by the ionization and the recombination process, introduced in Sec. 2.3.2 and in Sec. 2.3.3, respectively. The ionization process inherently involves laser-matter interaction. Hence, the generated plasma profile heavily depends on the gas and laser pulse properties. For instance, the generated plasma density increases with the pulse energy and intensity, with the actual scaling being highly nonlinear [Thé06] (see also Sec. 2.3.2). Furthermore, the ionization process depends on the pulse profile and duration, as introduced in Sec. 2.3.2. For very long pulses in the ns range, the ionization takes place over the whole pulse duration. Due to this long interaction time, collisional ionization dominates over the radiative ionization in the form of MPI or TI [Gia14]. In the case of a fs pulse, however, the interaction time is limited to an intra-pulse time window around the peak of the pulse. Because of this short interaction time and the low gas density, collisional ionization events are strongly suppressed and MPI or TI dominate [Yam11]. The ionization process also controls the initial free electron density and temperature T_e. For this experiment, however, the parameter study in Sec. 3.2.1 implies that the ionization event is not the driving process behind the severely different plasma lifetimes observed in the investigated gases. The tuning of the pulse energy showed no significant influence on the temporal plasma evolution of the plasma in air, nitrogen and carbon dioxide. The only effect of an increase in the pulse energy is a higher signal intensity of the TH, thus, a higher absolute plasma density. In consequence, also the different initial plasma densities cannot explain the individual lifetimes in-between the gases. The parameter pulse duration cannot be the reason either, since it was kept the same for all measurements. Thus, the different plasma lifetimes must originate from differences in the dynamics during plasma recombination which, in the case of fs laser pulses, is free from any laser-matter interaction. As already laid out in Sec. 2.3.3, the plasma processes during recombination are strongly dependent on the free electron temperature T_e. For the experimental conditions with a free electron temperature $> 1\,\mathrm{eV}$, recombination is mainly driven by the three-body electron-ion recombination channel. However, it assumed that the main processes responsible for the observed recombination dynamics are the non-recombining elastic electron-

electron collisions and the (non-recombining) inelastic collisions of free electrons with ions, atoms or molecules, as explained in Sec. 2.3.3. Differences in the recombining three-body collisions cannot explain the measurement results. To give an example: the geometrical atomic cross section for argon is three times higher than the one of molecular nitrogen [Fri11]. Hence, if recombining three-body collisions were the main process behind the recombination times, the argon plasma would show a faster decay than the nitrogen plasma. The large variety in the recombination times between the plasma of the atomic rare gases and the molecular gases originates from differences in the cross sections of non-recombining inelastic collisions of free electrons with atoms, molecules or ions. These cross sections are influenced by the density of the energy level structure. For atomic gases it is significantly lower than for molecular gases, since molecules also possess rotational and vibrational levels. These states have a small energy difference between adjacent ones. In consequence, the chance for an inelastic collision is less likely in an atomic than a molecular gas. In fact, the cross section of a free electron with a kinetic energy of 20 eV transferring energy to a certain amount of states of molecular nitrogen via inelastic collisions is higher [Mal09] than the total inelastic cross section of argon or xenon with an equal-energetic free electron [Hee79]. The cross section of nitrogen accounts to $89.9 \times 10^{-18}\,\mathrm{cm}^2$ [Mal09], whereas the cross section for argon is $50.8 \times 10^{-18}\,\mathrm{cm}^2$ [Hee79] and the one for xenon is $84 \times 10^{-18}\,\mathrm{cm}^2$ [Hee79]. The kinetic energy of a free electron in the laser-induced plasma at experimental conditions is expected to be lower than 20 eV, lying in the range of only a few eV [Cap00; Kar15] (see Sec. 2.3.3). Unfortunately, 20 eV is the lowest kinetic energy of a free electron for which comparable information on the cross sections of nitrogen, argon and xenon exists. Nonetheless, it can be expected that the trend remains the same also for lower kinetic energies because the cross sections of the atomic gases have a monotonously decreasing trend from a kinetic energy of 100 eV to a kinetic energy of 20 eV [Hee79]. In contrast, the cross section of molecular nitrogen shows a monotonously increasing trend in the same energy range [Mal09]. A similar behaviour is expected for the other atomic and molecular gases. When more inelastic non-recombining collisions take place, more low-energetic free electrons are generated. Since these free electrons recombine efficiently, the electron energy distribution function receives a dip on the low energy side. It is a

property of the EEDF to quickly reshape into a Maxwellian distribution by elastic free electron-electron collisions transferring energy from the high energy side of the EEDF to low energy side, leading to an overall decrease of the average free electron temperature T_e. The lower free electron temperature leads to a strong increase of the recombination rate due to the nonlinear temperature dependence of the three-body recombination rate coefficient (see Eq. 2.28 in Sec. 2.3.3). A faster shift of the EEDF (Sec. 2.3.1) in the molecular gases leads to a higher recombination rate in the atomic gases. Due to the nonlinear dependence of the recombination rate coefficient, a small difference in the redistribution time can already lead to a strong difference in the recombination time. This explanation also leads to an understanding of the different recombination times in-between the plasma of the rare gases. From helium to xenon, the energy level structure becomes denser, leading to a higher chance for non-recombining inelastic collisions to take place. This relationship is in accordance with the monotonously increasing cross section from neon to xenon for inelastic electron collisions for electrons with an energy of 30 eV. Thus, xenon plasma possesses the fastest plasma decay of all investigated gases and helium plasma the slowest.

In summary, the experimental findings about the plasma lifetimes in the different gases can be well understood by the recombination processes. The molecular gas plasmas have a significantly higher recombination rate than the atomic gas plasmas. The recombination rate is mainly influenced by the density of the energy level structure of the different gases for similar laser parameters and gas pressure levels. The denser energy structure of the molecular gases with respect to the atomic gases leads to a higher cross section for inelastic non-recombining collisions of free electrons with atoms, ions, or molecules. Due to these collisions, the EEDF is redistributed to a lower free electron temperature which in consequence leads to a higher recombination rate as explained in Sec. 2.3.3. The higher cross section for non-recombining inelastic collisions in the molecular gases with respect to the atomic gases leads to a faster redistribution of their plasma's EEDF and in that way to a higher recombination rate that severely lowers the plasma lifetime. This explanation can also be applied to understand the differences in the plasma lifetimes observed in the atomic gases: the less dense the energy level structure is, which is the case from xenon towards helium, the longer is the plasma lifetime in the respective gas atmosphere.

In the following, a more detailed analysis on the temporal TH evolution during the onset of TH enhancement in the atomic and molecular gases is presented. A surprisingly complex behaviour, which is invisible for delay steps $\geq 0.25\,\mathrm{ps}$, is found.

3.4 Investigation of the TH enhancement around zero delay

In addition to the measurements about the plasma lifetime in atomic and molecular gas atmospheres on the ps and ns time-scale, the TH enhancement around zero delay was studied to have a more detailed picture on the sudden change between no enhancement at negative delays and the strong maximum shortly after zero delay. It was expected, that the TH signal will increase to the maximum shortly after zero delay and then decrease again, as it can be observed in Fig. 3.13 for the molecular gases, or increase towards the maximum and remain there for several hundreds of ps until the signal decreases again, as it can be observed in Fig. 3.14 for the atomic gases. Fig. 3.16 shows the temporal TH measurement around zero delay for air. It was recorded with a delay stepping of 4 fs and scanned until around a maximum delay of 2.4 ps with a pulse energy of 300 µJ for the pump and a pulse energy of 550 µJ for the probe.

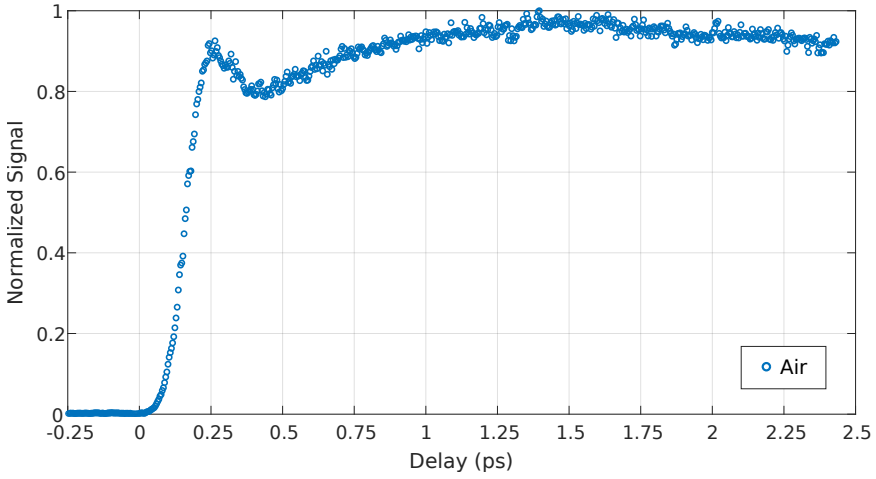

Figure 3.16: Normalized temporal TH evolution signal for air with a stepping of 4 fs and a pulse energy of 300 µJ for the pump and a pulse energy of 550 µJ for the probe.

Interestingly, the signal does not follow the expected trend. First, the TH signal rises from zero delay towards the maximum in about 0.25 ps. However, instead of decreasing monotonously after the maximum, the signal first decreases and reaches a local minimum after around 125 fs from the maximum but then increases again and reaches another maximum, in fact the global maximum of the trace, 1.125 ps later, i.e. at an absolute delay of 1.5 ps. Whereas the first increase from no TH enhancement towards the first local maximum is very rapid, the increase from the local minimum towards the global maximum takes about 4.5 times longer. Since the overall temporal window from the onset of TH signal until the global maximum takes only 1.5 ps, the unexpected trend of the signal is not visible in the longer scans presented earlier, as the whole scan around zero delay only comprises four to five data points in the long scans. The scan around zero delay, with the same stepping and laser parameters than for air, was repeated for the molecular gases nitrogen, carbon dioxide and the atomic gases helium and argon. The measurements are summarized in Fig. 3.17 and the corresponding characteristic features are stated in Tab. 3.4.

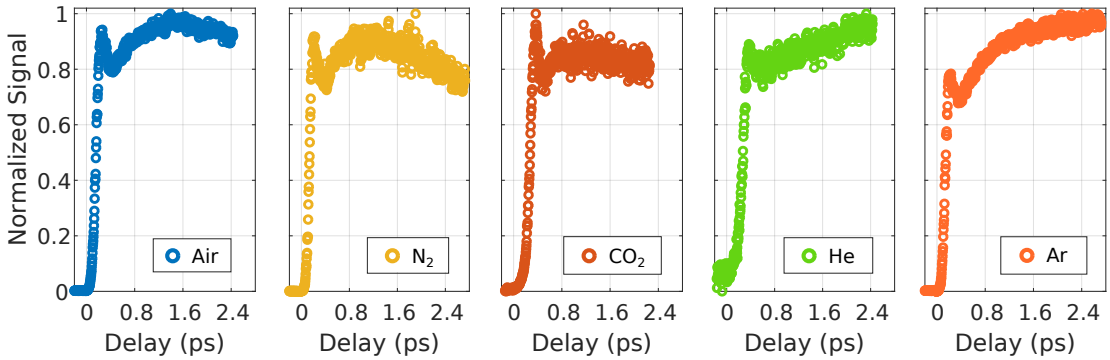

Figure 3.17: Normalized temporal TH evolution signals for air, nitrogen, carbon dioxide, helium and argon around zero-delay scanned with a stepping of 4 fs and a pulse energy of 300 µJ for the pump and a pulse energy of 550 µJ for the probe. Adapted from [Jus20].

The overall trend of the temporal TH evolution in air, i.e. a peak followed by a minimum and a subsequent reincrease of the signal, can be observed for all gases but there are also specific differences. In accordance with the measurement in air, the TH traces in the molecular gases show a second peak. For the TH traces in air and nitrogen atmosphere, the second peak is also the global maximum. The TH

Table 3.4: Properties of characteristic features of the TH traces shown in Fig. 3.17.

Gas	Peak [fs]	Int. peak [%]	Min. [fs]	Int. min. [%]	Peak2 [fs]	Int. peak2 [%]
Air	240	94	430	79	1480	97
N_2	200	92	400	74	1160	90
CO_2	280	100	480	75	960	86
He	280	89	480	77	/	/
Ar	200	78	400	69	/	/

traces in helium and argon do not show a second maximum. There, the TH signal is monotonously increasing from the minimum until the end of the scan range. The most striking difference between the TH traces in atomic gas atmosphere with respect to the TH traces in molecular gas atmosphere is that relative signal strength of the first peak and minimum is significantly lower in comparison to the overall trace. In contrast to helium, the TH signal of argon has a distinct minimum and TH signal is asymptotically increasing towards the maximum signal with a $f(t) = 1 - \exp(-t)$ function-like behaviour, whereas helium shows a linear increase.

Overall, all investigated gases show a local minimum after having reached the maximum of the trace. This similar trend indicates that it is caused by an effect that exists in the plasma-induced TH enhancement in all gas atmospheres.

In a further investigation performed in air atmosphere, the power dependency of the this short-time scale effect was investigated. Therefore, the pulse energy in the pump arm was tuned to 160 µJ, 240 µJ and 320 µJ and the TH signal recorded with a temporal stepping of 4 fs. The measurement is shown in Fig. 3.18 and the corresponding characteristic features are summarized in Tab. 3.5.

Table 3.5: Properties of characteristic features of short-time pulse energy scan of air shown in Fig. 3.18.

E_{pulse} [µJ]	Peak [fs]	Int. peak [%]	Min. [fs]	Int. min. [%]	Peak2 [fs]	Int. peak2 [%]
160	240	100	410	57	1600	67
240	240	100	410	81	1700	96
320	240	100	410	81	1700	96

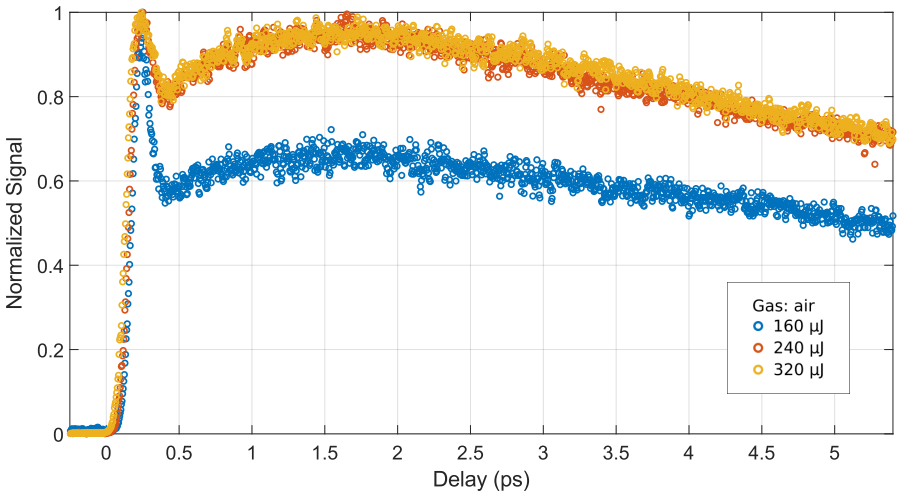

Figure 3.18: Normalized temporal TH evolution signals of air for different pump pulse energies with a stepping of 4 fs and a probe pulse energy of 550 µJ.

The scans for a pump pulse energy of 240 µJ and 320 µJ are nearly identical but the scan for a pump pulse energy of 160 µJ is distinctively different. Its minimum and second maximum are significantly lower than for the other two pulse energies and the contrast between the two is smaller, i.e. the second maximum is relatively shallow. Fig. 3.19 shows the same traces than in Fig. 3.18 in a zoomed-in version around the onset of the TH enhancement.

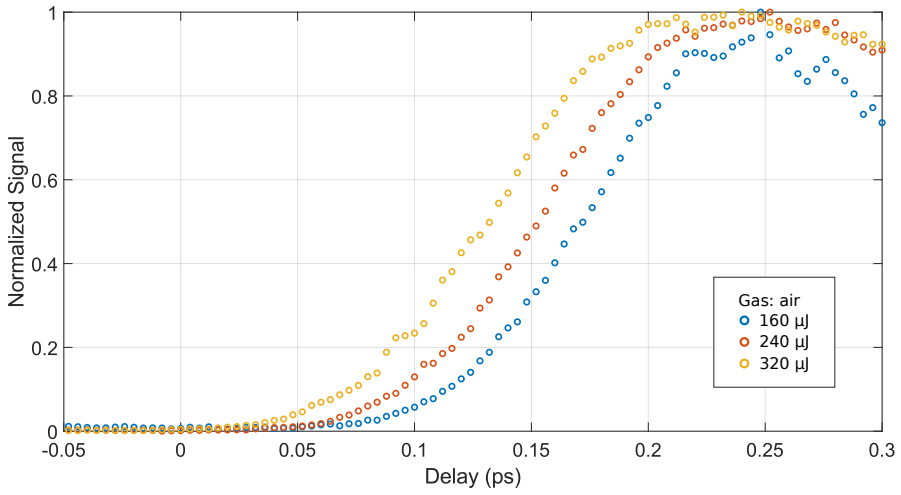

Figure 3.19: Normalized temporal TH evolution signals of air for different pump pulse energies with a stepping of 4 fs and a probe pulse energy of 550 µJ around zero delay.

It is observed that the onset of TH enhancement scales inversely with the pump pulse energy. The TH of the highest pump pulse energy of 320 µJ increases the earliest, followed by the trace for a pump pulse energy of 240 µJ and the trace for the pump pulse energy of 160 µJ. The traces show a roughly linear spacing in their onset point, being 20 fs (320 µJ and 240 µJ) and 16 fs apart from each other (240 µJ and 160 µJ), respectively. Note that the delay stepping of the measurement is 4 fs, so the two spacings differ only by one delay step, a difference which can be explained by measurement noise. In a further measurement it was investigated, whether the characteristic features of the TH temporal evolution as a function of the pump pulse energy, observable in air, can also be observed in other gases. Hence, the pump pulse energy study was carried out in argon with the same temporal stepping and laser parameters as in air. The measurement can be observed in Fig. 3.20.

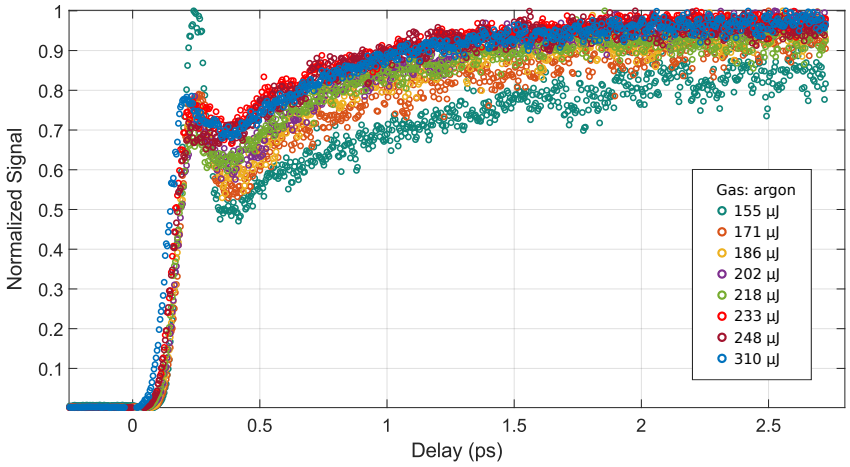

Figure 3.20: Normalized temporal TH evolution signals of argon for different pump pulse energies with a stepping of 4 fs and a probe pulse energy of 550 µJ.

The pulse energy scan for argon shows some similarities and some differences to the one in air. As in the case of air, all traces show a distinct first maximum from which the signal decreases again towards a local minimum. However, from the local minimum the signal is not increasing again towards a second local or global maximum, as it is the case in air, but the signal just monotonously increases with a decreasing slope until the end of the scan range, in accordance to the temporal

measurements for argon and helium presented in Fig. 3.17. In all traces, with the exception of the one with the lowest pulse energy of 155 µJ, the global maximum is reached at the end of the scan range. In the scan with a pulse energy of 155 µJ, the first maximum is also the global maximum of the trace, being 2 times higher than the minimum. The ratio for the other traces is much smaller, with the traces for 233 µJ, 248 µJ and 310 µJ having the smallest ratio of about 1.12. A similar trend takes place in air, where the traces corresponding to a pump pulse energy of 240 µJ and 320 µJ have a nearly identical max-min ratio of 1.25, whereas the trace for a pump pulse energy of 160 µJ has a ratio of 2.27. The zoomed-in plot of Fig. 3.20, showing the onset of the TH signal in argon atmosphere, is presented in Fig 3.21.

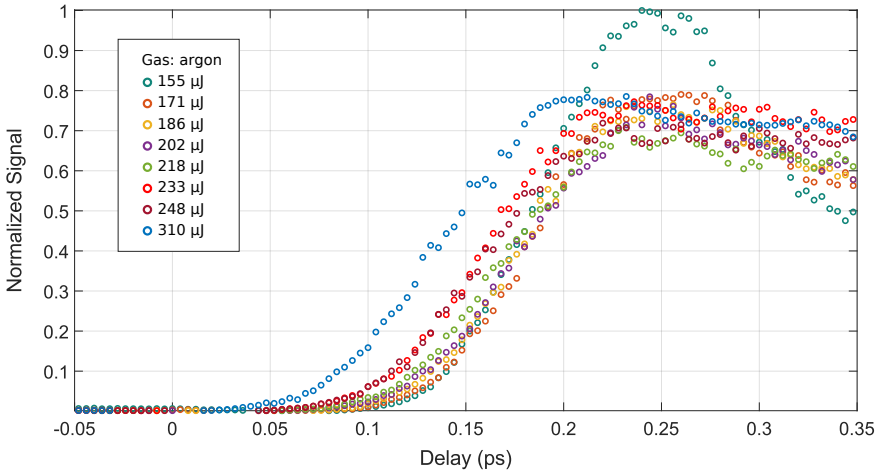

Figure 3.21: Normalized temporal TH evolution signals of argon for different pump pulse energies with a stepping of 4 fs and a probe pulse energy of 550 µJ around zero delay.

As in the case of the TH traces in air, the onset of the TH trace depends on the pump pulse energy, with the traces for higher pump pulse energies starting earlier than the traces for lower pump pulse energies. However, in the case of argon the trend is not as clear as it is for air, since the spacing of the traces for the different pump pulse energies is not equidistant. Nonetheless, the trace for highest pump pulse energy of 310 µJ clearly starts the earliest.

In summary, the experimental results on the TH enhancement around zero delay show some similarities for the atomic and molecular gases: the TH signal rises

towards a maximum in the beginning until it decreases towards a local minimum and rises again towards a local or global maximum. In the case of the molecular gases, the second maximum is comparable in height with the respect to the first maximum, in the case of the atomic gases, the maximal signal is reached at the end of the scan range after a monotonous increase from the local minimum. In the pulse energy scans performed in air and argon atmosphere a similar behaviour can be observed: the trace for the lowest pulse energy clearly differs to the similar traces of the other pulse energies, with a significantly stronger first maximum with respect to the overall TH evolution. Comparing the TH onset in air and argon atmosphere, a different behaviour in the two gases can be observed. In the case of air, the traces of the different power levels are equidistantly spaced, with the trace with the highest pump pulse energy starting the earliest and the trace with the lowest pump pulse energy starting the latest. This trend is not that obvious in argon: the trace for the highest pump pulse energy clearly starts the earliest but then the traces are not clearly separated or equidistantly spaced from each other. Nonetheless, the traces maintain the order observed in air atmosphere with the highest pump pulse energy starting the earliest and the lowest pump pulse energy starting the latest.

3.5 Analysis and discussion of the TH enhancement around zero delay

3.5.1 Temporal TH evolution around zero delay

The temporal TH traces around zero delay in all investigated gases show an unexpected evolution with a first peak, followed by a local minimum with a re-increasing signal afterwards. Whereas the TH evolution for delays significantly greater than about 0.5 ps can clearly be attributed to plasma-induced TH enhancement (see Sec. 2.4.8 and [Sun09; Sun10; Yao12]), the explanation for the signal evolution until $\tau = 0.5\,\mathrm{ps}$ is not so simple. This difficulty lies in the fact that pulse-related effects such as the Kerr effect and other intensity-dependent effects still contribute, as it is explained by Suntsov *et al.* for a very similar experimental configuration [Sun09]. This group and another, [Yao12], also observed the sharp increase in the TH signal after zero delay and, in the case of Suntsov *et al.*, the pump-energy-dependent shift in the TH onset. A likely explanation for the experimental findings around zero

delay goes back to a pump-probe experiment conducted in fused silica with a near collinear geometry between a strong pump and weak probe [Jür19]. In this experiment, a double-peaked structure is observed shortly after zero delay for the measured transmission loss of the probe, due to plasma generation by the pump, propagating through the fused silica sample. Zero delay is defined by the maximum distortion of the probe's pulse spectrum caused by crossed-polarized wave generation between the pump and probe. The first maximum in the transmission loss, around 100 fs after the zero delay, is attributed to a nonlinear pump-probe interaction, described as a two-beam coupling (TBC) process in [Smo00; Bur05; Wah13], leading to a depletion of the probe [Jür19]. TBC describes two-beam interaction caused by the Kerr nonlinearity for a spatial and temporal overlap of the two interacting beams. When a strong pump arrives before the probe, the coupling can even take place without temporal overlap, if the pump-driven Kerr nonlinearity has a non-instantaneous response [Bur05]. In that case, the Kerr nonlinearity has a relaxation time and the probe interacts with the Kerr-induced transient material modification by the pump. The delayed Kerr response leads to a phase shift of the probe that can either, depending on its sign, lead to energy gain or energy loss [Smo00]. The double-peaked structure with the first maximum followed by the local minimum observed in the experiments here for all the investigated gases (see Fig. 3.17) could be caused by such a TBC, induced by a delayed Kerr response due the strong pump interacting with the gas. The nonlinear dependency of the first-maximum-to minimum-ratio as a function of the pulse energy speaks in favour of an intensity-dependent effect such as the Kerr nonlinearity. However, the interaction shortly after zero delay might even be more complicated with plasma dynamics contributing to the TH evolution: directly after the pump has formed the plasma, it is very dense and compact. In that moment the plasma induces a strong modification to the filament (signal) pulse shortly after zero delay leading to a strong enhancement that leads to the first peak. With ongoing time, the laser-induced plasma expands [Gia17]. During the expansion phase, it becomes less dense so that the free electron density decreases, leading to a reduction in the modification of the filament pulse. In consequence, the TH signal decreases and reaches the local minimum. With ongoing expansion, the plasma starts to match better spatially with the bigger filament beam compared to the initially compact

pump beam. Hence, the signal increases again leading to the second maximum (in case of the molecular gases) or the monotonously increasing signal in the scan range (in the case of the atomic gases). Since the plasma continues to expand, the spatial match of the plasma with the signal beam becomes worse again, leading to a reduction in TH intensity, as observed in the molecular gases. The different temporal trend in the TH evolution of the atomic gases compared to the molecular gases can be explained by different material-dependent time constants for the plasma expansion caused by disparate initial free electrons temperatures and densities after the plasma creation. Since the plasma expansion is temperature-dependent [Gia17], the initial free electron temperature plays an important role in the subsequent plasma dynamics. Further, the second maximum in the TH traces of the molecular gases is reached much slower than the minimum after the first peak. This characteristic feature of the TH traces could be attributed to a nonlinear decrease in the plasma expansion speed caused by a nonlinear reduction of the free electron temperature due to collision processes [Gia17]. Note that plasma recombination should only play a minor role until around $\tau = 2\,\mathrm{ps}$, thus being insufficient to explain the dynamics directly after zero delay. However, recombination could already contribute significantly to the decrease of the TH signal after the second maximum in the molecular gases. For the atomic gases, recombination is completely negligible for the scan range. The TBC- and the plasma-related explanation for the TH around zero delay are not mutually exclusive and can also take place simultaneously.

3.5.2 Pulse-energy-dependent shift of TH onset

While both explanations in Sec. 3.5.1 can be applied to the overall short-time TH evolution in the scan range, the shift in the TH onset depending on the pump pulse energy needs to be treated separately, as it only comprises the short temporal window from zero delay to maximally $\tau = 100\,\mathrm{fs}$, which makes plasma expansion unlikely as an explanation. In principal, it is expected that the TH enhancement starts when the pump and probe pulse begin to overlap spatially [Sun10]. However, the geometrical configuration of the setup remains the same, when only the pump pulse power is tuned. Hence, geometrical effects cannot explain the shift in the TH onset. The shift could also be explained by TBC, since a higher pump pulse energy would

lead to a stronger Kerr effect, effectively causing an earlier enhancement of the TH. In that case, the spacing between the onsets of TH for the different pump pulse energies should be linearly dependent on the pump energy, since the Kerr effect is linearly dependent on the intensity (see Eq. 2.4 in Sec. 2.2.1). For the measurement of air (Fig. 3.19) that is the case. For the situation in argon (Fig. 3.21) it is not so evident. Note that the temporal stepping of the TH onset amounts to only 4 fs. Hence, small fluctuations in the pump pulse energy strongly influence the observed pump-dependent shifts of the TH onset. A power-stabilized pump pulse is needed for further studies of this effect.

In summary, the unexpected behaviour of the TH temporal evolution shortly after zero delay in all investigated gases can have different reasons, these being a non-instantaneous Kerr response and spatial plasma effects. Also a simultaneous contribution of the Kerr response and the plasma effects together is possible. Further investigation on the influence of the different effects assisted by 3D simulations of the pulse propagation including Kerr nonlinearity and plasma expansion models is needed so that a cleaner explanation of the TH evolution and the pump-energy-dependent shift of the TH onset can be given.

CHAPTER 4

Spatio-temporal characterization of a femtosecond filament along its length

In this chapter, the experiment aiming at the complete spatio-temporal characterization of a femtosecond filament at several positions along its length is presented. According to Couairon *et al.* [Cou07], a filament characterization can be called "complete", if the measurement combines intensity maps of the real space intensity $I(\boldsymbol{r},t)$ as well as of the reciprocal space intensity $I(\boldsymbol{k},\omega)$ as a function of the propagation direction z. More strictly, a complete filament characterization must determine the three-dimensional representation of the electric field's amplitude and phase. To the best of the author's knowledge, the method presented here is the first complete characterization method of a femtosecond filament. So far, experimental studies have focused on characterizing the filament pulse in the temporal or spectral domain, usually in combination with spatial sampling [Tzo01a; Cou02; Sku06; Sti06; Sch09; Sch11a; Kre14; Pus19]. If spatio-temporal investigations were performed, they were either limited in the analyzed filament length [Kos97] or mainly studied the pulse energy along the propagation length [Bro97; Fon99a]. In bulk media, e.g. quartz glass [Kum03], and liquids, e.g. water [Mat04], spatio-temporal filament characterization measurements along the length of the respective medium have been carried out but without determining the electric field of the pulse. Existing complete spatio-temporal characterization methods like the ones introduced in Sec. 2.5.2 - 2.5.3, have not been applied to filament pulses, yet.

This chapter begins with a presentation of the experimental setup used for filament characterization, followed by a description of the experimental procedure and principle, and concludes with a discussion of the experimental results.

4.1 Experimental setup, procedure, principle, and conditions

This experiment was conducted at the Atomic Physics Department at Lund University in Sweden with LASERLAB-EUROPE funding (654148, EU H2020) and is reported in [Neo22]. Performing the experiment in Lund provided a beam-pointing stabilized laser system as well as the possibility to quantitatively fine-tune the dispersion of the fundamental driving pulse, enabling a high reproducibility of the experimental conditions such as the maximized spectral broadening. Further, the required combination of a spatio-temporal characterization (spatially resolved Fourier transform spectrometry) and temporal characterization (dispersion scan) setup for the complete filament characterization was already installed. These two characterization techniques were combined with a filament termination technique brought by Leibniz University Hannover, consisting of a custom vacuum component with a mounted and exchangeable thin metal plate that is installed into the filament generation chamber. With the filament drilling a pinhole through this plate, it serves as a differential pumping stage [Sch11a]. In the following, the experimental setup is described.

4.1.1 Laser system and experimental setup

The experimental setup for the spatio-temporal characterization of the femtosecond filament is shown in Fig. 4.1. The employed laser system is a Ti:Sapphire-based amplifier with a central wavelength of 800 nm and a repetition rate of 1 kHz, generating an average power of up to 5 W. To optimize beam pointing, the transversal beam position is monitored by two beam cameras, positioned at the near field and the far field of the beam, counteracting slow transversal beam drifts by sending their information into a feedback loop of a two-mirror stabilization setup. An acousto-optical programmable filter (Dazzler, Fastlite Inc.) is used to adjust the spectral phase of the laser pulses up to the third order of dispersion, generating nearly Fourier transform limited pulses with a duration of 21 fs at the filament setup. The Dazzler is used to negatively pre-chirp the pulses from the laser amplifier for optimal white-light generation conditions in the filament. Due to its precise control – GDD and TOD can be adjusted individually – the filament generation conditions are repeatable to a high degree. The amplified and chirp-manipulated laser beam

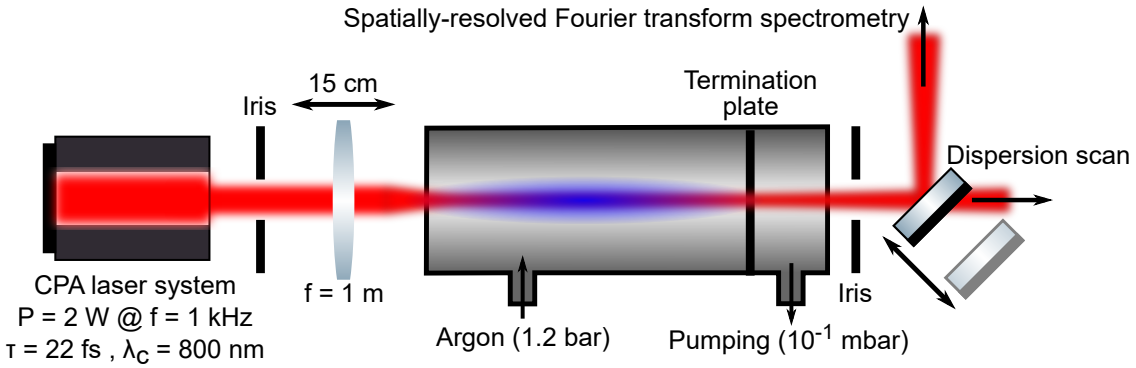

Figure 4.1: Experimental setup for the filament generation chamber and termination stage. The laser beam is focused into an argon-filled gas tube. Inside the gas tube, a filament is generated, which drills a hole through a thin aluminium plate. Subsequently, the filament is terminated by pumping the generation gas. The beam from the filament stage can either be sent to a temporal characterization setup (dispersion scan) or a spatio-temporal characterization setup (spatially resolved Fourier transform spectrometry). Reprinted with permission from [Neo22] © The Optical Society.

passes an adjustable aperture for fine-tuning of the pulse energy and beam size and is then focused into a 1.2 m long gas tube, filled with argon, by a $f = 1\,\mathrm{m}$ lens. This lens is mounted on a translation stage with a travel range of 15 cm along the beam direction (M-UTM150CC.1, Newport Inc.). The aperture and the lens enable precise control over the input energy, the (geometrical) focal spot size and the initial formation point of the filament. Inside the gas tube, a filament with a length of approximately 20 cm is generated, estimated by the visible plasma fluorescence. The filament is terminated by a 0.5 mm thick aluminium plate, positioned shortly after the geometrical focus of the beam. The filament beam drills a hole through the plate with a diameter of $\approx 200\,\mu\mathrm{m}$. As this hole size roughly corresponds to the dimensions of the filament core (see Sec. 2.1.1), the measurements are limited to studies of the central spatial region and exclude the reservoir and conical emission. Subsequent pumping of the tube section after the plate reduces the pressure to about 10^{-1} mbar. At this pressure level, nonlinear beam propagation is sufficiently suppressed, stopping the filamentation process. Thus, further pulse propagation after the sharp pressure gradient is linear. By moving the lens, the filament is shifted with respect to the gas tube and, in that way, can be terminated at different positions along its length

with µm precision. In this experiment, the filamenting pulse is characterized at 9 relative positions, i.e. $d = 0\,\mathrm{mm}$, $d = 15\,\mathrm{mm}$, $d = 35\,\mathrm{mm}$, $d = 55\,\mathrm{mm}$, $d = 75\,\mathrm{mm}$, $d = 95\,\mathrm{mm}$, $d = 115\,\mathrm{mm}$, $d = 135\,\mathrm{mm}$, and $d = 150\,\mathrm{mm}$. $d = 0\,\mathrm{mm}$ represents the earliest filament position, where it is the shortest, while $d = 75\,\mathrm{mm}$ lies in the middle of the characterized filament length, and $d = 150\,\mathrm{mm}$ describes the longest filament, i.e. the last scanned position. The gas flow inside the tube is constantly regulated to ensure a stable pressure during data acquisition. An insertable cross-hair after the filamentation tube is used as an alignment reference for the two characterizations setups. By centering the generated diffraction pattern of the cross hair on the alignment irises of the characterization setups, it is ensured that both are sampling the filament beam in the same way. Behind the crosshair, neutral density (ND) filters can be placed into the beam path. After the filters, the beam can be sent either to the d-scan setup for temporal pulse characterization (see Sec. 2.5.5) or to the SRFTS setup (see Sec. 2.5.2) for spatio-temporal pulse characterization. About 1.5 m before the SRFTS setup, a focusing mirror with $f = 1\,\mathrm{m}$ is placed to collimate the divergent beam from the gas tube. In the path of the d-scan setup, no refocusing mirror is installed so that the divergence expands the beam for characterizing only a small central area of the transverse beam profile. The d-scan and the SRFTS setup are presented in Fig. 4.2.

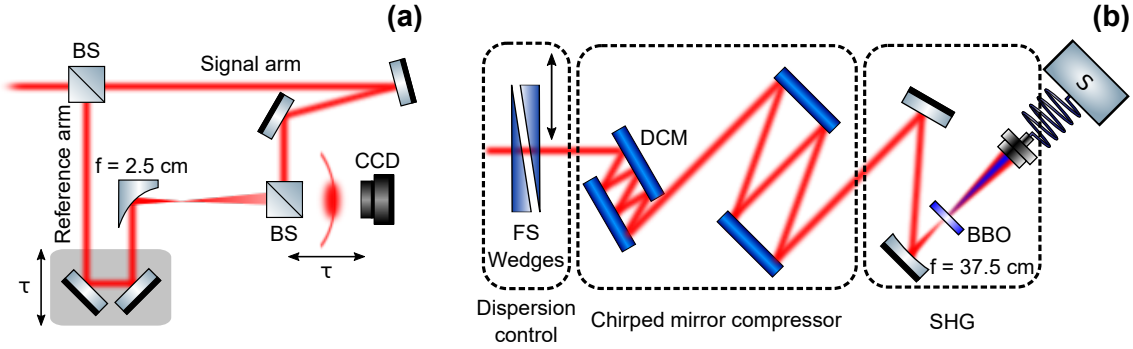

Figure 4.2: Pulse characterizations setups. (a) Spatially resolved Fourier transform spectrometry setup for spatio-temporal pulse characterization. BS: beam splitter. (b) Dispersion scan setup for temporal pulse characterization. FS: fused silica, DCM: double-chirped mirrors, S: spectrometer. Reprinted with permission from [Neo22] © The Optical Society.

For a spatio-temporal characterization of the filament beam, the SRFTS setup is used. The working principle is explained in Sec. 2.5.2 and shown in Fig. 2.6 and Fig. 4.2(a). A Mach-Zehnder-type interferometer consists of a reference and a signal arm. Here, the slightly focused incident beam is split into the respective arms by a 90:10 beam splitter. The reference beam passes a movable retroreflector mounted on a piezo stage with sub-optical-cycle precision (Piezo Systems Jena) which is used to adjust the delay between signal and reference. Subsequent to the retroreflector, the beam is tighly focused with an OAP mirror with a focal length of $f = 2.5\,\mathrm{cm}$. From the focal spot, the beam heavily diverges with spherical wave fronts. The reference beam recombines with the signal beam at the second 50:50 beam splitter, generating a spatial interference pattern that is recorded with a CCD camera with a chip size of $12\,\mathrm{mm} \times 8\,\mathrm{mm}$ and pixel size of $3.6\,\mu\mathrm{m}$ (GS3-U3-91S6M-C, FLIR Inc.). The signal beam propagates through a neutral optical density (ND) 0.4 filter (not shown), reducing the beam power by about 60 %, adapting the intensity of the signal with respect to the reference beam at the CCD. The attenuation is necessary because, although the reference beam contains 90 % of the initial pulse energy, without the ND filter it would have a much lower signal strength than the signal beam, due to its strong divergence. Even with the signal beam's attenuation by the ND filter, the reference is still weaker at the camera chip. The large beam size of the reference leads to a homogeneous beam distribution on the sensor, as only a very small spatial portion of it is measured with the beam camera. Due to this large expansion, the central pixel of the measured signal at the CCD corresponds to a field autocorrelation trace of the reference pulse. The signals of the other pixels inhibit the phase difference of the signal pulse with respect to the reference pulse at that position of the transverse beam profile. The CCD is positioned at a distance from the second beam splitter at which the signal beam roughly covers one third of its total size. As described in Sec. 2.5.2, the beam size at the sensor is a trade-off between spatial resolution on the one hand and coverage of the spatial frequency bandwidth on the other hand, as well as avoiding significant beam diffraction. The beam size of choice is optimal for the given experimental conditions. For a measurement with the SRFTS setup, the retroflector in the reference arm is scanned and a spatial interference pattern on the CCD is recorded for every delay step.

The other beam path after the gas tube leads to the d-scan setup for a temporal characterization of the center of the filament beam, providing the characterization of the reference of the SRFTS setup. The principle of d-scan is described in Sec. 2.5.5 and the scheme is shown in Fig. 2.8 and Fig. 4.2(b): the SH spectrum of a pulse is measured as a function of its dispersion tuned around the zero point, i.e. close to its Fourier transform limit. In the d-scan setup of the experiment, this requirement is achieved by compressing the pulse in a DCM compressor (PC70, Ultrafast Innovations GmbH). Since the DCM compressor can only introduce integer steps of negative dispersion depending on the amount of reflections on the mirrors – in the experiment the total amount of negative dispersion accounts to $\approx -320\,\mathrm{fs}^2$ at 800 nm – the pulse is fine-tuned with positive dispersion by inserting a pair of 8° motorized fused silica wedges into the beam. The amount of positive dispersion depends on the inserted glass thickness. The SH spectrum is generated by focusing the beam with a concave silver mirror with $f = 37.5\,\mathrm{cm}$ into a beta barium borate (BBO) crystal and it is recorded with a fiber-based optical spectrometer. For every investigated filament position, two d-scan measurements are performed, one before the SRFTS scan and one after, by scanning the wedges and recording the SH spectrum for every wedge insertion step. Additionally, a fundamental spectrum is recorded for every d-scan measurement.

In the following, the experimental procedure for the spatio-temporal characterization of the femtosecond filament along its length is described.

4.1.2 Experimental procedure

With an alignment iris and camera before the filamentation stage the beam is aligned through the gas tube. An aluminium plate is installed into the gas tube and the residual air before and behind the plate is pumped out. The translation stage of the lens is moved to a position, for which the geometrical focus is approximately at the aluminium plate. The adjustable aperture is slightly closed, the cover above the setup removed, and the beam is sent into the setup. Without any cover, the size of the hole becomes slightly larger due to increased beam pointing fluctuations, avoiding partial beam blocking by random beam movements during data acquisition. The focused beam drills through the plate in a few seconds but the drilling is continued

for another 30 min. It has been observed that after this waiting time the hole size does not increase anymore. Subsequently, the cover above the setup is put back and the chamber is filled with argon and regulated to stable conditions, while the compartment behind the plate is continuously pumped. The lens' translation stage is moved to the center. With argon inside, a filament in the gas tube is formed. The adjustable aperture is closed to an empirically found optimal opening diameter for the broadest white light and most stable filament conditions. With a bigger diameter, the filament is prone to break up into multiple filaments; with a smaller diameter the broadening is first reduced and at some point the filamentation regime abruptly ends. The chosen pressure level, the opening diameter and other experimental parameters for optimal generation conditions are described in detail in Sec. 4.1.4. The crosshair behind the gas tube is inserted and the beam is aligned to the characterization setups. After completion of the alignment, the crosshair is taken out. The lens' translation stage is moved to the measurement start position $d = 150\,\mathrm{mm}$. At this position, the measured filament has the greatest length and the largest spectral broadening. The GDD and TOD are adjusted via the Dazzler for optimizing the broadening, also providing for the most stable filament conditions. The spectral broadening is verified with a measurement of the fundamental spectrum at the d-scan setup. Then, a scan along the filament can be performed. A d-scan trace is recorded with empirically determined scanning parameters for a good recording quality. For every d-scan measurement, an additional recording of the fundamental spectrum is taken. Subsequently, ND filters with a combined attenuation of 5 orders of magnitude are inserted behind the crosshair position to attenuate the intense filament beam for a spatio-temporal scan with the SRFTS setup. With empirically determined optimal scan settings, a scan is recorded in about 30 min. Optimal parameters for the delay stepping and the pixel binning are predetermined by the beam size on the CCD, the focal length of the refocusing mirror in the beam path of the interferometer, and the Fourier-limited pulse duration, i.e. the spectral bandwidth. Once a spatially-resolved interferogram is recorded, the ND filters behind the crosshair position are removed and another d-scan trace is recorded in order to check that the filament conditions did not change since the recording of the spatio-temporal scan. If the filament conditions did change, another spatially resolved interferogram is recorded. Once a proper set of

one spatio-temporal scan and two dispersion scans is recorded, the lens' translation stage is moved to the next filament position and the procedure is repeated until the end of the stage or the scan range of interest.

In the following, the experimental principle, showing and explaining typical measurement traces as well as the necessary data treatment after the recording of a measurement, are presented.

4.1.3 Experimental principle

The goal of the experiment is a complete spatio-temporal characterization of a femtosecond filament along its length. Hence, the measurement needs to encompass the entire size of the filament core and the generated interference pattern between signal and reference beam at the SRFTS setup needs to be sampled well. Furthermore, the spatio-temporal as well as the temporal scan require a sufficient temporal resolution to resolve the filament pulse dynamics in the time domain. The measured filament pulses are sub-10 fs long and cover a maximal spectral width of $575 - 925$ nm. The fundamental spectrum and laser pulse which generates the pulses, can be seen in Fig. 4.3(a) and (b), respectively. The fundamental pulse has a central wavelength of 816 nm.

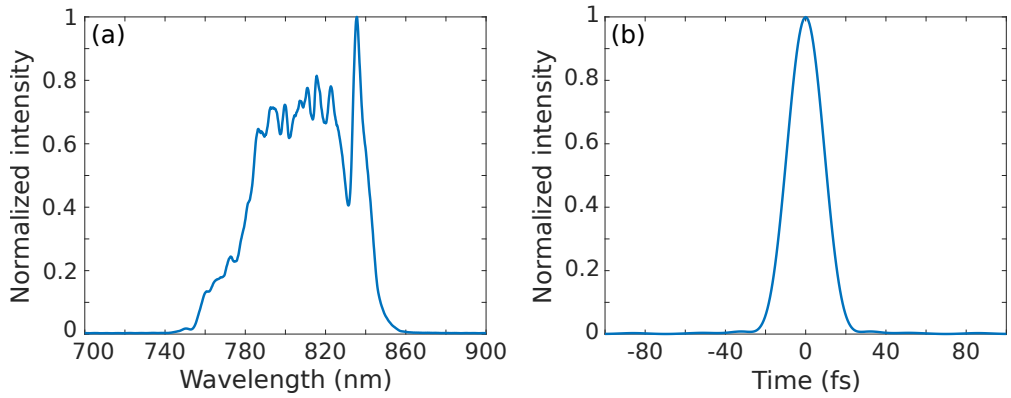

Figure 4.3: (a) Fundamental laser spectrum used for the experiment, enabling the strongest spectral broadening in the filament and the corresponding Fourier-transform-limited temporal pulse profile (b).

A typical d-scan trace from the experiment is presented in Sec. 2.5.5 in Fig. 2.9. A typical spatial interference pattern of the SRFTS setup can be observed in Fig. 4.4(a) for the filament position $d = 150$ mm.

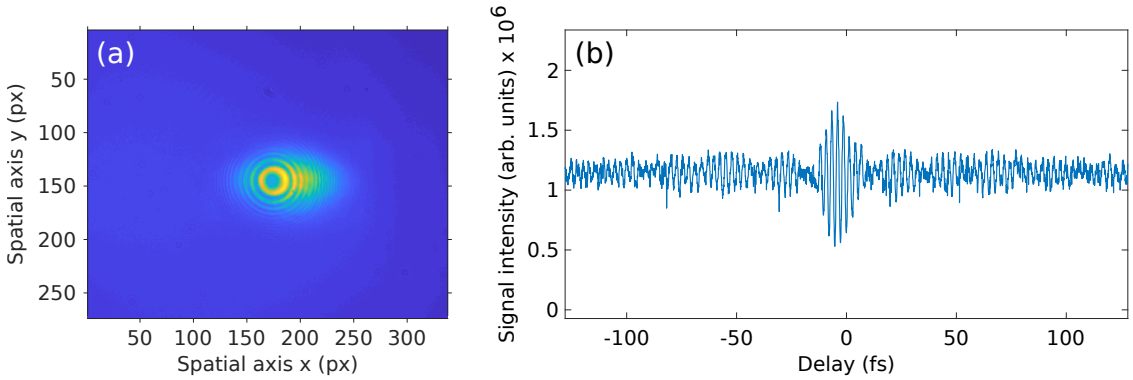

Figure 4.4: Binned CCD trace of the spatial interference pattern from the Fourier transform interferometer at zero delay (a) and lineout of the central pixel for $d = 150\,\text{mm}$ (b).

The binned CCD trace at central delay $\tau = 0\,\text{fs}$ possesses a high contrast interference pattern at the central position ($x = 175$, $y = 175$) with a decreasing contrast towards the horizontal edges at position ($x = 150$, $y = 150$) and ($x = 250$, $y = 250$). The non-interfered background signal is formed by the reference beam. Fig. 4.4(a) shows, that under real experimental conditions, the recorded reference signal is not completely homogeneous which reduces the contrast of the recorded interference pattern and lowers the signal-to-noise ratio (SNR). The horizontal lineout from the binned CCD pixels at midpoint of the spatial interference trace, displayed in Fig. 4.4(b), illustrates the observed contrast of the temporal interference signal. It shows a maximum contrast of the interference signal around zero delay with adequate contrast levels ranging from around $-10\,\text{fs}$ to $10\,\text{fs}$. Outside this range, the contrast is reduced by a factor 4 to 5. Nonetheless, the temporal window width cannot be reduced as it determines the frequency resolution. The maximum resolved frequency is determined by temporal delay step size. Note that the actual oscillating signal is isolated from the measured interference pattern via fast Fourier transform (FFT). A total spatio-temporal scan comprises of an interferogram, such as the one in Fig. 4.4(b), for every pixel of the CCD sensor. For the measurement, a temporal scan window from $-128\,\text{fs}$ to $128\,\text{fs}$ is chosen. Since a spectrum in the spectral domain represents the Fourier transform of an interferogram in the time domain, a fundamental spectrum can be reconstructed from the interferogram. Theoretically,

the fundamental spectrum of the central position of the spatial interference pattern needs to be equivalent to the fundamental spectrum measured with the d-scan setup, since both represent the reference beam, i.e. a reconstructed fundamental spectrum from the central pixel of the interference pattern can be used for cross-reference between the two methods. In practice, the limited SNR and resolution of the method let the spectrum from the SRFTS setup appear less broad than the one from d-scan, but their comparisons still provides a decent quality check. An example for a reconstructed fundamental spectrum for filament position $d = 150\,\mathrm{mm}$ can be observed in Fig. 4.5. Note that the spectral phase in Fig. 4.5 is only available after the full spatio-temporal pulse reconstruction.

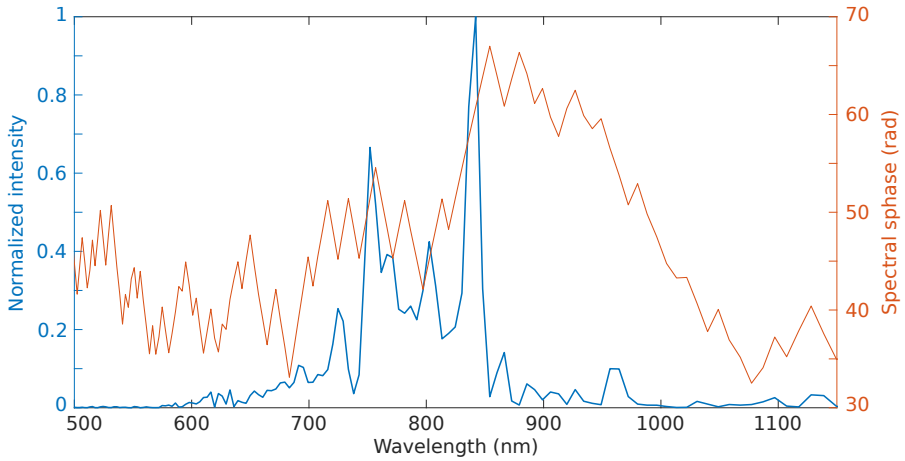

Figure 4.5: Reconstructed fundamental spectrum from the interferogram of the CCD pixel at midpoint of the interference pattern for $d = 150\,\mathrm{mm}$ (blue) and the corresponding reconstructed spectral phase (red).

Data treatment

The original data from the SRFTS setup is contained in a three-dimensional interferogram $I(x, y, \tau)$, representing the interferogram of the reference and the signal beam, spatially resolved in the two spatial dimensions x and y, where τ is the delay in the convolution. The signal pulse $E(x, y, \omega)$ in the spectral domain is contained in the measured trace $A_{\mathrm{cross}}(x, y, \omega)$ as described in Eq. 2.42 and Sec. 2.43 in Sec 4.1.1. Hence, first a Fourier transform of $I(x, y, \tau)$ with respect to the delay dimension is performed. By filtering the signal contribution around $+\omega_0$, $A_{\mathrm{cross}}(x, y, \omega)$ is obtained. Subsequently, $\tilde{E}'(x, y, \omega)$, containing the curvature of the spherical wavefronts, can

be calculated from $A_{\mathrm{cross}}(x, y, \omega)$ by dividing $A_{\mathrm{cross}}(x, y, \omega)$ by the reference field (see Eq. 2.42), assuming a homogeneous reference beam and inserting the spectral phase of the reference field, ϕ_{ref}, which is obtained by an additional measurement with the d-scan pulse characterization technique. The spectral phase of the reference is corrected with respect to the dispersion offset between the d-scan setup and the SRFTS setup by taking into account the dispersion landscape of all optical components between the two. This correction includes the DCM phase, the glass wedges and the propagation in air. In the next step, the spherical curvature of the reference field, originating from its expansion from the tight focus after the OAP, is removed from $\tilde{E}'(x, y, \omega)$ and the signal pulse in the spectral domain, $E(x, y, \omega)$, is obtained. The spherical curvature is removed by subtracting the phase of a numerically calculated spherical wave originating from a point source at the position of the OAP. In the final step of the initial data treatment, the signal field is transformed back into the temporal domain and interpolated to a new data grid that is large enough to cover the entire pulse information during the numerical backpropagation towards the termination point, but small enough to not take up unnecessary much memory space. The numerical backpropagation is presented in the following.

Numerical backpropagation

Gaining insight into the pulse properties at the termination point allows to perform an in-situ analysis of the filament dynamics by terminating the filament at different positions along its length. For the reconstruction of the filament pulse at this position of interest, $\tilde{E}(x, y, \omega; z_{\mathrm{ter}})$, a numerical backpropagation of the signal field $\tilde{E}(x, y, \omega)$ from the SRFTS setup to the termination point of the filament needs to be performed. For this purpose, a Fourier optics plane wave propagator $K_z(\omega) = \sqrt{K_{\mathrm{disp}}(\omega)^2 - k_x^2 - k_y^2}$ with the transverse wavenumbers k_x and k_y is applied to the field at the CCD, where the wavenumber $K_{\mathrm{disp}}(\omega)$ takes into account the dispersion landscape between the two positions. With the propagator, the field $\tilde{E}(x, y, \omega)$ is propagated to a plane located at z via:

$$\tilde{E}(x, y, \omega; z) = \mathcal{FT}^{-1}\{\tilde{E}(k_x, k_y, \omega) \exp(-iK_z)\}, \tag{4.1}$$

where $\tilde{E}(k_x,k_y,\omega)$ represents the 2D Fourier transform of $\tilde{E}(x,y,\omega)$ with respect to the spatial domains x and y. For the spatial backpropgation of $\tilde{E}(x,y,\omega)$ from the SRFTS setup towards the termination point of the filament, the complete landscape of components affecting the spatial backprogation, i.e. the divergence of the beam, needs to be included. In this experiment, this involves the linear propagation through air towards the $f = 1\,\mathrm{m}$ focusing mirror for beam collimation and the linear propagation in air and vacuum from the mirror towards the aluminium plate. Hence, the propagation towards the termination plate is performed in two steps: (i) from the SRFTS setup to the mirror and (ii) from the mirror to the termination point. The curvature of the mirror needs to be taken into account by applying the phase $\phi_{\mathrm{mirror}}(x,y,\omega) = \exp(iK_{\mathrm{disp}}(\omega)(x^2+y^2)/2f)$ in real space and spectral domain, with f being the focal length of the mirror. With the complete electric field $\tilde{E}(x,y,\omega;z_{\mathrm{ter}})$ at the termination point, the filament dynamics can be studied in situ and in detail by Fourier transforming the field to any domain of interest such as space vs. time (x,y,t), space vs. wavelength (x,y,λ), and reciprocal space vs. wavelength (k_x,k_y,λ), to name a few.

As introduced in Sec. 2.4, a filament inhibits very complex spatio-temporal pulse dynamics along its length. For instance, at certain positions in the filament, the leading edge of a pulse splits spatially and temporally from the main pulse due to plasma defocusing (Sec. 2.4.7). Dynamics such as the pulse splitting event, should be observable in the three-dimensional representation of the filament pulses at different propagations lengths. In the following, a brief insight into the supporting simulations for the filament dynamics of the experiment is given.

Simulations on the filament dynamics

The simulations encompass the nonlinear pulse propagation by inhibiting all important processes for describing filament dynamics, such as self-focusing and SPM due to the Kerr effect, as well as plasma generation by field-induced ionization. They support the spatio-temporal measurements and can be used also to reference the results by providing a simplified view on the relevant dynamics that can be compared to the actual observations.

The nonlinear pulse propagation is simulated by a numerical integration of the unidirectional pulse propagation equation (UPPE) [Kol02] for the carrier-resolved electric field, as outlined in [Bro19]. The generation of free electrons due to ionization is described by the formulation derived by Perelomov *et al.* [Per66]. The linear and nonlinear refractive indices of argon, are derived from [Dal60] and [She90] respectively. Following the method described in [Cou08], the nonlinear refractive index of argon is calculated to $n_2 = 2 \times 10^{-19}\,\mathrm{cm}^2/\mathrm{W}$ from the data in [She90]. A Fourier transform-limited pulse, corresponding to the experimentally measured pulse spectrum of the incident pulse sent into the gas tube (see Fig. 4.3) along with the experimentally measured beam size and pulse energy, was taken as the input pulse for the simulations.

Before the experimental results are presented in Sec. 4.2, a short overview about the experimental conditions for the presented measurement results is given in the following.

4.1.4 Experimental conditions

Three key motivations existed for the chosen experimental parameters of the filament: (i) the spectral broadening should be as large as possible, supporting the shortest possible laser pulses, which are strongly affected by nonlinear propagation dynamics, (ii) the earliest termination position of the filament should have enough spectral broadening due to nonlinear propagation dynamics so that a d-scan retrieval, requiring shorter pulses than the incident pulse sent into the gas tube, can be performed, (iii) the filament conditions should be as stable and reliable as possible. As already outlined in Sec. 4.1.2, the strongest broadening is usually also close to the most stable filament conditions. However, finding a match between strongest broadening, usually at the end of the filament, and a sufficient broadening at the beginning of the filament for d-scan pulse characterization is a trade-off. What “sufficient broadening” for the d-scan retrieval means, depends on the applied DCMs and the glass wedges for the dispersion manipulation in th d-scan setup with respect to the spectral bandwidth of the pulse of interest. The broadening and the stability of the generation conditions in general, e.g. avoiding break-up into multiple filaments, is controlled by the initial chirp of the fundamental pulse, the pulse energy, the beam size and the pulse

duration. For the experiment, the fundamental pulse was pre-chirped by $-200\,\mathrm{fs}^2$ to compensate for the positive dispersion of optical components before the gas tube. In this way, a nearly Fourier transform-limited pulse of 21 fs at the filament formation was achieved. Furthermore, the optimal generation conditions were found to be at a gas pressure of 1.2 bar and an iris opening of 4.2 mm, corresponding to a pulse energy of 0.7 mJ for the chosen focusing with a $f = 1\,\mathrm{m}$ lens.

In the following, the experimental results from the d-scan and the SRFTS setup, spectrally (d-scan) and spatio-temporally (SRFTS) backpropagated to the termination plate, are presented for a length of 15 cm along the filament. Note, that a pure spectral backpropagation of the d-scan measurements towards the termination point is equivalent to an analysis of the pulse center, whereas the spatio-temporal backpropagation expands the pulse information to the whole spatial profile.

4.2 Experimental results

This section begins with the results of the spectral evolution of the filament followed by the temporal evolution of the spectrally backpropagated d-scan pulses at the termination point, i.e. the temporal evolution of the pulse center. Subsequently, an investigation of the filament dynamics in two- and three-dimensional representations at the termination point, is presented. The analysis of the filament dynamics is supported by a time-frequency analysis via short-time Fourier transform (STFT).

4.2.1 Spectral evolution and comparison with simulations

In Fig. 4.6(a), the interpolated evolution of the experimental spectrum as a function of the relative filament length d is illustrated. Fig. 4.6(b) shows the corresponding simulated spectral evolution. The experimental evolution of the filament spectra shows that the spectral width increases towards longer filament lengths. All spectra in the filament are broader than the fundamental spectrum, presented in Fig. 4.3, underlining strong broadening by SPM in the filament along with broadening by plasma generation. The broadening is stronger on the blue side than on the red side, with the spectrum of the final position $d = 150\,\mathrm{mm}$ extending from 575 nm until 925 nm. Over the length of the filament, the spectral components on the blue side of the spectrum decrease in intensity but the blue edge extends further out. This expansion towards the blue also leads to an overall blue shift of the spectra as it is evident from Fig. 4.6. A spectral blue-shift during propagation is a typically effect

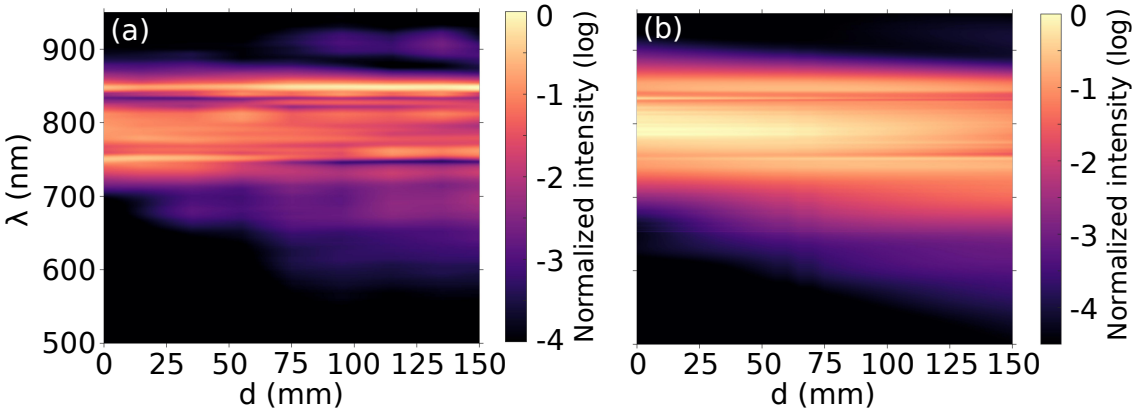

Figure 4.6: Spectral evolution of the beam center as a function of the relative filament length d in logarithmic representation: (a) experimental data interpolated from measurements at 9 different filament positions d, (b) spectral evolution of the simulated filament. Reprinted with permission from [Neo22] © The Optical Society.

observed in filamentation and is caused by the asymmetrical broadening induced by the plasma generation at the leading part of the pulse because of the plasma gradient, as described in Eq. 2.18 in Sec. 2.3.1.

The simulation, with its spectral evolution shown in Fig. 4.6(b), well reproduces the observed trends in the spectral evolution of the experiment, underlining that the observed spectral evolution can be understood and reproduced by basic nonlinear filament propagation dynamics involving plasma-induced broadening.

In the following, the experimental results of the temporal evolution of the filament pulse center is presented and compared to the results of the simulations.

4.2.2 Temporal evolution and comparison with simulations

In Fig. 4.7(a), the interpolated temporal evolution of the filament pulse center in the experiment is presented as a function of the relative filament position d. Fig. 4.7(b) displays the corresponding evolution of the on-axis temporal pulses from the simulations. In the analysis of the experimental temporal evolution it has been observed, that the pulse center and the spatially averaged pulse, i.e. the resulting pulse from an integration of the three-dimensional profile over the transversal spatial dimensions x and y, possess a nearly identical behaviour. Therefore, for simplification, the temporal evolution is only shown for the pulse center, based on the spectrally backpropagated d-scan pulses.

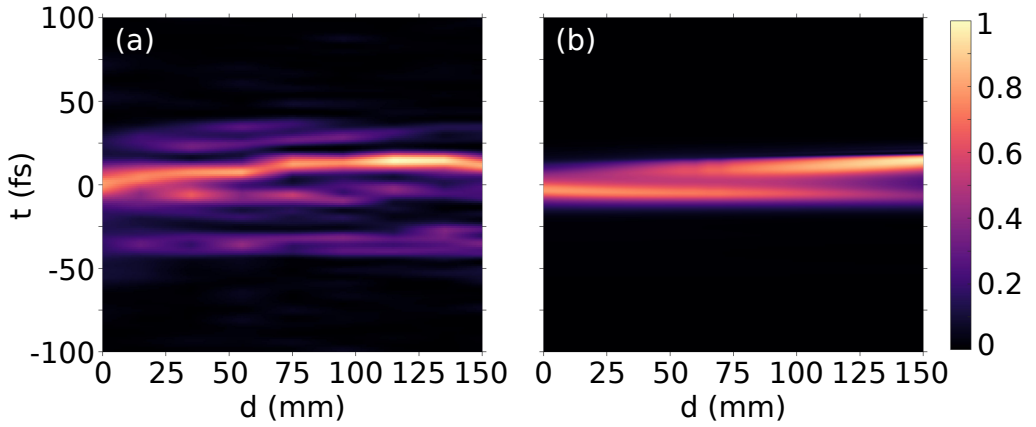

Figure 4.7: Temporal pulse evolution as a function of the filament position d. (a) interpolated experimental evolution of the filament pulse center, (b) simulated on-axis temporal pulse evolution. Reprinted with permission from [Neo22] © The Optical Society.

Fig. 4.7(a) shows that the earliest filament position possesses a pulse duration close to the one of the fundamental pulse, indicating that the filament formation point was captured at the beginning of the characterization. The pulse consists of a main peak with a temporal duration of 19 fs and two satellite pulses, a pre-pulse 35 fs before and a post-pulse 25 fs after the main pulse. During filament propagation, the main pulse splits at around $d = 25$ mm and the split reaches a maximum in the middle of the length with a separation of 25 fs. The splitting remains until the end of the scan range with a final separation of around 20 fs. This behaviour is well reproduced in the simulations, which show very similar splitting dynamics with the same separation at the end of the filament. However, the simulations do not show any pre- or post-pulse features. They probably stem from optical components before the filament setup, such as mirror coatings, and appear to not be related to non-Gaussian spectrum of the incident pulse or to the filamentation dynamics. Further, the pre-pulse gives the impression that it is gaining power during filament propagation. However, this apparent power increase is a normalization side-effect, attributed to the collection efficiency of the pre-pulse varying for the different filament termination points with respect to the geometrical focus, caused by beam diffraction at the termination plate's pinhole. In contrast, the intensity decrease of the post-pulse is attributed to plasma defocusing caused by the plasma generation of the main pulse. Nonetheless,

the pulse dynamics or contributions of the pre- and post-pulses cannot be determined exactly by sole observations in the spectral or temporal domain, so they might also inhibit self-driven nonlinear dynamics. The main pulse at the final filament position has a full width at half maximum (FWHM) of about 7 fs and is therefore significantly shorter than the main pulse at the beginning of the filament. This decrease in pulse duration during filament propagation clearly shows the effect of self-compression described in Sec. 2.4.6.

For a deeper understanding of the pulse evolution, a time-frequency analysis is performed on the fully spatio-temporally backpropagated electric field of the investigated pulses via STFT. In short-time Fourier transform, a sliding window function $G(t-\tau)$ is used to gate the electric field $\tilde{E}(t)$ of the pulse via:

$$E_{\mathrm{TF}}(\omega,t)=\int_{-\infty}^{\infty}\tilde{E}(t')G(t-t')e^{-2\pi i\omega t'}dt', \tag{4.2}$$

with E_{TF} representing the spectrogram, i.e. the time-frequency representation, of the electric field $\tilde{E}(t)$ via the gating with the window function. The actual shape of the window function is chosen to fit best the analysis of interest. Typical window functions are the Gaussian, the Kaiser, and the Tukey window. In addition to the actual window type, the function has the degree of freedom of a so-called "shape factor". Time-frequency analysis enables to analyze the spectral content of different temporal slices of a pulse. However, a time-frequency analysis inherently is a compromise between the resolution in the temporal and spectral domains. The better the resolution in one of the two domains, the worse it is in the other domain. Due to the connection of the two domains, this type of analysis is perfectly suited for an analysis of STCs, as temporal pulse components with a strongly different background in nonlinear dynamics will show discrepancies in their spectral content. Further, the main temporal component driving the nonlinear dynamics during filamentation can be traced [Akt08]. In Fig. 4.8(b), the spectrogram of the pulse center of the last filament position $d = 150$ mm is illustrated, with the spectral and temporal projections in Fig. 4.8(a) and Fig. 4.8(c), respectively.

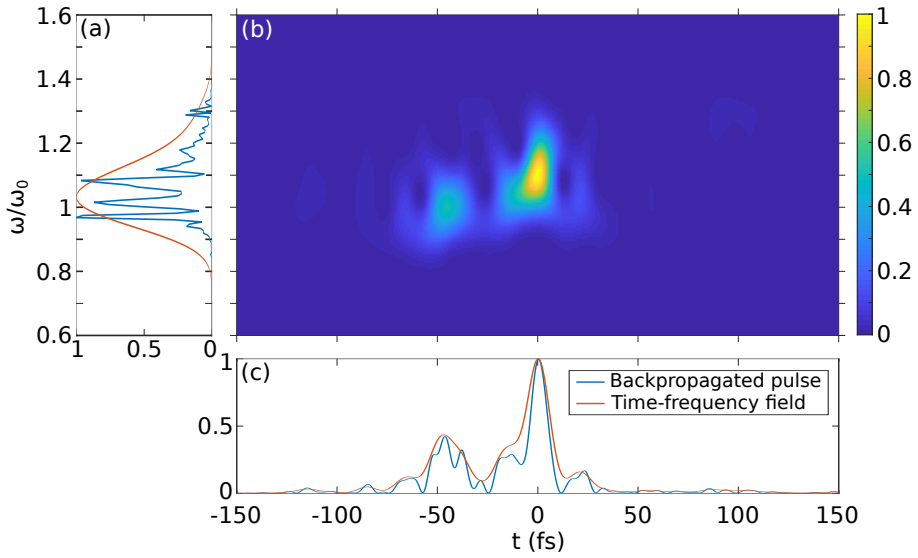

Figure 4.8: Spectrogram of the filament pulse for $d = 150\,\text{mm}$. Absolute square of the short-time Fourier transform of the field $E(x_c, y_c, t)$ at the center of the filament (b). Projections on the frequency- (a), and time axis (c). The frequency $\omega_0 = 2.31$ rad/fs corresponds to the central frequency of the input spectrum. Reprinted with permission from [Neo22] © The Optical Society.

For the time-frequency analysis of this experiment, a 34 fs long Kaiser window with a shape factor of 10 is chosen, providing a good trade-off between the spectral and temporal resolution, visible in the respective projection plots in comparison to the backpropagated spectrum and temporal pulse. The spectrogram clearly shows that the pre-pulse at $-35\,\text{fs}$ has a non-broadened spectrum, supporting the assumption that it is not contributing significantly to the nonlinear pulse dynamics. In contrast, the time-frequency analysis does not have enough temporal resolution to resolve the splitting of the main pulse but can reveal that its spectral width is significantly increased compared to the pulse spectrum at the beginning of the filament visible in Fig. 4.6. In summary, the findings about the filament dynamics via time-frequency analysis illustrate the potential of this method for the analysis of filamentation dynamics.

In the following, the results of the spatio-temporal evolution of the laser pulse during the propagation in the filament are presented in different two-dimensional representations of the various pulse domains, expanding the insights about the dynamics from the sole spectral and temporal analysis.

4.2.3 Filament dynamics in two-dimensional representations

The previous presentation of the spectral and temporal evolution of the filament has demonstrated that complex nonlinear propagation dynamics are not well recognized by observing these two domains separately. Via time-frequency analysis, combining temporal and spectral analysis, it could be shown that the disparate temporal features of the filament pulse at the final position $d = 150\,\mathrm{mm}$ were influenced differently strong by the previous nonlinear pulse propagation. The great advantage of the experimental method presented here is that, with the complete spatio-temporal characterization of the filament pulses, the analysis can be expanded to any relevant domain or combination of domains, greatly supporting the analysis of the filament pulse dynamics. Fig. 4.9 shows an overview of eight different relevant combinations of domains for the last filament position $d = 150\,\mathrm{mm}$. Note that x_c and y_c correspond to the coordinates of the beam center along the respective transverse spatial coordinates x and y.

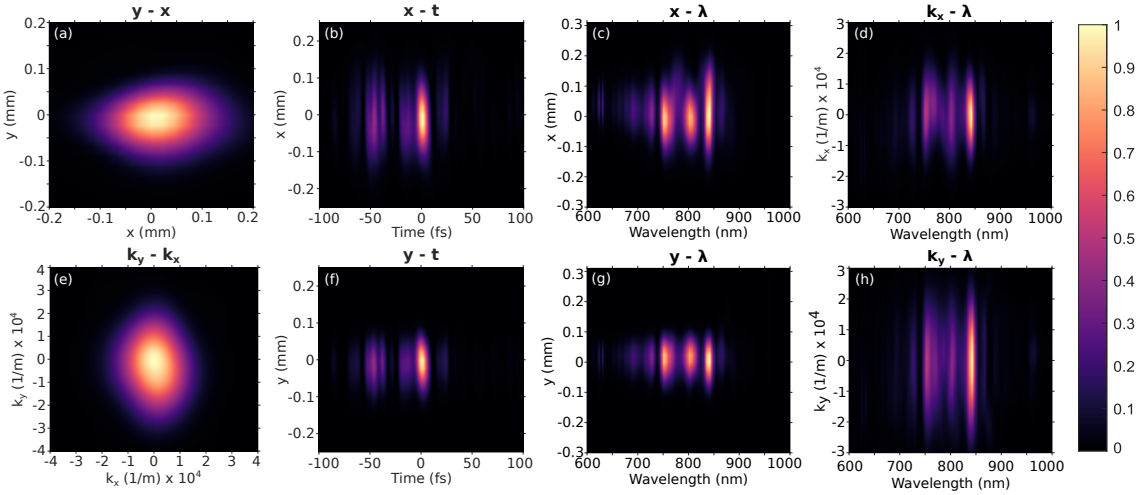

Figure 4.9: Normalized pulse representations of the last filament position in different two-dimensional combinations. (a) Spatial profile along the spatial dimensions x and y. (b) Spatio-temporal profile with respect to the spatial dimension x for y_c. (c) Spatio-spectral profile with respect to the spatial dimension x for y_c. (d) Reciprocal-spectral profile with respect to the reciprocal dimension k_x for $k_y = 0$. (e) Reciprocal pulse profile along the reciprocal dimensions k_x and k_y. (f) Spatio-temporal profile with respect to the spatial dimension y for x_c. (g) Spatio-spectral profile with respect to the spatial dimension y for x_c. (h) Reciprocal-spectral profile with respect to the reciprocal dimension k_y for $k_x = 0$.

Depending on the analysis of interest, the required domains can be combined; the method gives access to all. In order to trace the dynamics of the filament along its length, the analysis needs to be repeated for different positions d. In the following, for simplicity, the analysis is reduced to the four filament positions $d = 15\,\mathrm{mm}$, $d = 55\,\mathrm{mm}$, $d = 95\,\mathrm{mm}$, and $d = 135\,\mathrm{mm}$ and to the domains $x - t$, $x - \lambda$, and $k_x/k_0 - \lambda$. The respective plots for the orthogonal dimensions y and k_y show similar dynamics and can therefore be omitted. For all the three presented sets of domains, the four sub-plots are normalized to their global maximum.

In Fig. 4.10, the evolution of the x-t-domain, for y_c, is shown.

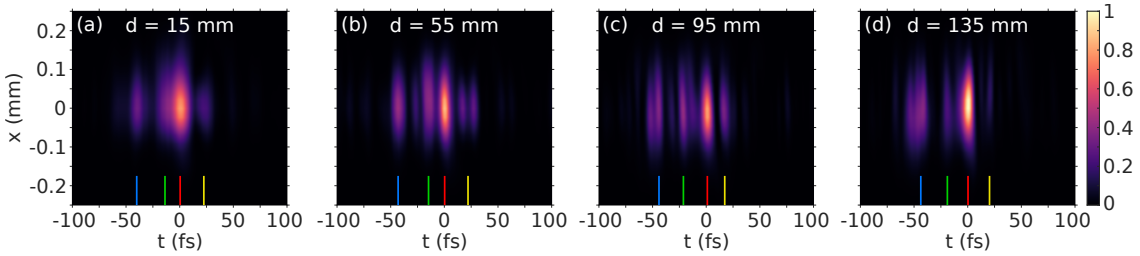

Figure 4.10: Temporal pulse evolution along the filament spatially resolved along the x direction, for y_c. Important elements are highlighted by colored ticks. A splitting of the main pulse (green and red ticks) can be distinguished from a pre-pulse (blue) and post-pulse (yellow). Reprinted with permission from [Neo22] © The Optical Society.

The most important elements known from the temporal evolution, the pre- and post-pulse as well as the main pulse, are also accurately resolved in this two-dimensional representation. Whereas the main pulse clearly splits during propagation (its sub-pulses are marked in red and green), the post-pulse (marked blue and yellow, respectively) does not significantly change its temporal behaviour. The pre-pulse shows a small splitting event that, however, is not as clear and widely separated at the end of the filament than the one for the main pulse. This observation supports once more the assumption that the pre-pulse is not significantly contributing to the nonlinear pulse propagation. Hence, as described in Sec. 4.7: since the pre-pulse is not drilling on the metal plate, the pinhole of the termination plate has a significant influence on its transversal beam size, because in that way the beam size depends on the relative distance of the filament position to the geometrical focus. Nonetheless, the pinhole is not affecting the observed temporal properties since these rely on

the undisturbed center of the pulse profile only, due to the d-scan characterization. As the main pulse self-focuses during propagation, its beam size is well sampled during propagation. The post-pulse is likely defocused by the plasma, explaining its intensity loss over the filament length.

In the following, the spatio-spectral evolution along the x-λ-domain for y_c is presented in Fig. 4.11.

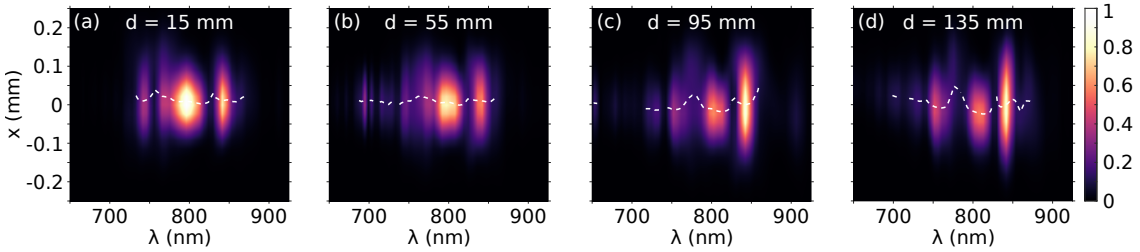

Figure 4.11: Beam size evolution as a function of the wavelength along the length of the filament for y_c. The dashed white line indicates the center of mass of the normalized intensity distribution with a threshold of 10 %. Reprinted with permission from [Neo22] © The Optical Society.

The spatio-spectral pulse evolution clearly shows a consistent increase of spectral evolution towards the blue side of the spectrum. In the beginning of the filament the spectral power is concentrated at around 800 nm but during further filament propagation it is redistributed towards the red side. The initial main peak roughly has a constant beam size during propagation, whereas the beam size of the red edge clearly increases. The blue edge, which is generated close and in front of the pulse peak in time and space, under the strong influence of self-focusing, preserves a small beam size over the length of the filament. The center of mass, indicated by the dashed white line with an intensity threshold of 10 %, highlights a pulse feature at around 770 nm that slightly shifts towards the red and persists throughout the whole length of propagation, being clearly off-center with respect to the main pulse distribution. As the shift already exists at the beginning of the filament, it is probably an artefact from the fundamental pulse, potentially from the pulse compressor. Nonetheless, such an observation is a clear STC and its observation is only possible with a complete spatio-temporal characterization, showing the potential of the characterization method. In addition to the shifted pulse feature at around 770 nm, a slight spatial chirp can be observed towards the end of the filament.

In the following, the angular spread in k_x-direction, for $k_y = 0$, as a function of the wavelength is analyzed, illustrated in Fig. 4.12.

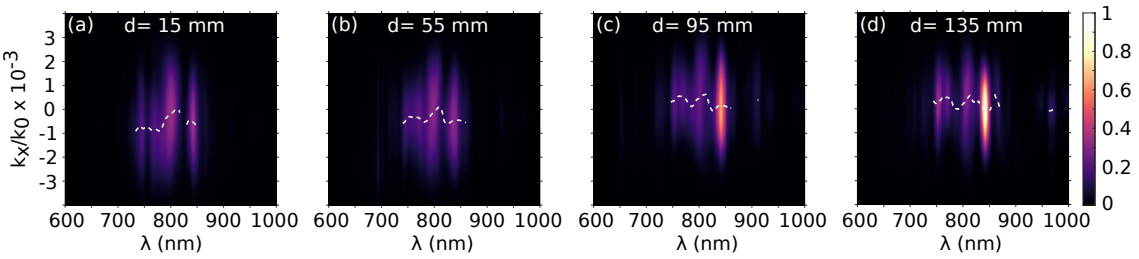

Figure 4.12: Angular spread evolution k_x/k_0 of the beam along the length of the filament as a function of the wavelength for $k_y = 0$. The dashed white line indicates the center of mass of the normalized intensity distribution with a threshold of 10 %. Reprinted with permission from [Neo22] © The Optical Society.

The angular spread is approximately similar for all wavelengths, showing a decreasing trend during filament propagation. In the beginning of the filament, the intensity is nearly equally distributed over the spectral dimension. During filament propagation, it is shifted towards the red edge of the distribution. Further, in accordance with the spatio-spectral evolution (see Fig. 4.11), the center of mass (dashed line) shows that there is a feature at 770 nm, which is significantly shifted with respect to the mean angular spread of the distribution, here indicating a variation in the propagation angle for this particular wavelength.

Overall the investigation of the filament dynamics in two-dimensional representations reveals that the nonlinear propagation may lead to complex effects on the pulse over the length of the filament. Fortunately, these dynamics can be resolved with the presented complete spatio-temporal characterization method, underlining the need of it for femtosecond filamentation analysis.

In the following, the filament analysis is extended to a three-dimensional representation, a novelty enabled by the presented characterization method.

4.2.4 Filament dynamics in three dimensions

A complete spatio-temporal characterization of a pulse is three-dimensional, with the field amplitude and phase of the pulse given in the two transversal spatial dimensions x and y as well as the temporal dimension t or, in reciprocal space, given in the two

reciprocal dimensions k_x and k_y along with the spectral dimension λ. Hence, also a complete three-dimensional pulse representation can be created from a measurement method such as the one presented in this thesis. To the best of the author's knowledge, this is the first representation of this kind for a femtosecond filament.

In the plots presented here, the intensity profile is normalized and presented in "shells" with a colour code. Every shell represents an intensity step of 25 %, ranging from 25 % to 75 %. A shell of 25 %, for instance, comprises all spatio-temporal parts of the pulse that have an intensity of at least 25 % of the maximum. Hence the shells become smaller for a higher intensity level. The color-code of a shell consists of a saturation and transparency series of red. The more saturated and less transparent the red, the higher is the relative intensity, with the non-transparent and completely saturated red representing the intensity range from 75 % to 100 %. Fig. 4.13 shows the three-dimensional intensity representation of the pulse, i.e. $|E(x, y, t)|^2$, for the last filament position $d = 150\,\mathrm{mm}$. The visible impact of nonlinear pulse propagation dynamics, such as the pulse splitting, is the strongest for that filament position, making it a good candidate for a demonstration of this plot type. Along with the three-dimensional representation of the pulse in reciprocal space (not shown), i.e. $|E(k_x, k_y, \lambda)|^2$, a complete view on the filament pulse at a certain termination position can be given with just two plots. Note that due to the numerical backpropagation, this spatio-temporal representation can be created for any beam position between the filament termination point and the characterization setup. In that way, also beam parameters such as the Strehl ratio [Mah83], a measure of the focus quality, can be obtained by this approach. The three-dimensional representation reproduces the observations made for this filament position in the temporal analysis shown in Fig. 4.7. Note that in Fig. 4.13, zero-delay is positioned at the center of the main pulse. The pre-pulse can be clearly observed, as well as the temporally separated component from the main pulse due to the splitting event. While, the intensity shells represent the fully three-dimensional view on the filament pulse, the planes of the plot show its projections into the respective domains (x, t), (y, t), and (x, y), providing a quick checkup of the pulse in two-dimensional representations.

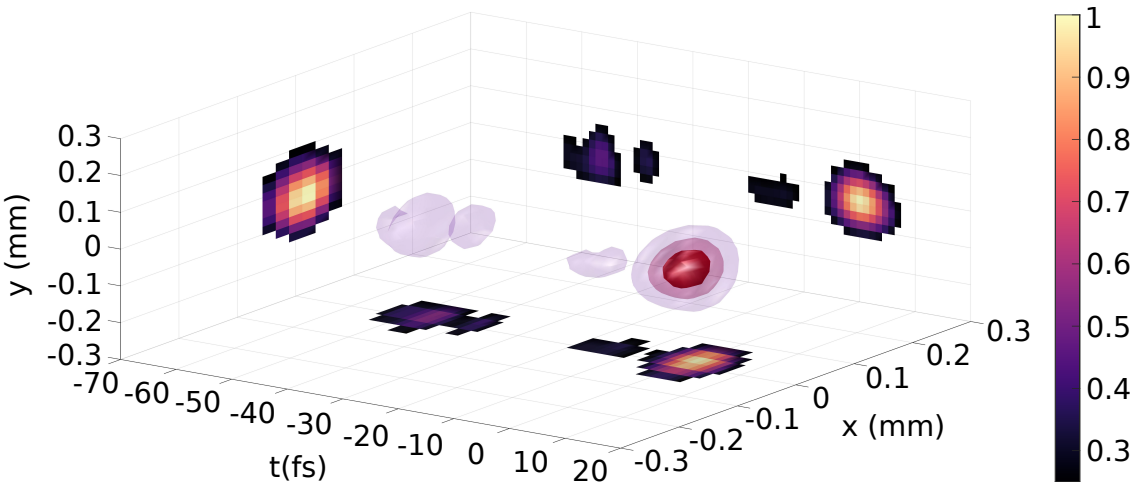

Figure 4.13: Normalized three-dimensional representation of the longest filament, $d =$ 150 mm, in real space. The intensity is shown in shells of 25 % steps, ranging from 25 % to 75 % of the maximum intensity. Reprinted with permission from [Neo22] © The Optical Society.

Fig. 4.13 demonstrates, that the three-dimensional view on filament pulses serves as a powerful and convenient tool to analyze the major dynamics of a filamenting pulse. However, local fluctuations of the beam properties at different positions across the spatial beam profile might not easily be observed with this plot type. Therefore, the homogeneity of the pulse properties over transverse beam profile for the last filament position $d = 150$ mm is analyzed via the earlier-introduced time frequency analysis. In Fig. 4.14 the spectrograms of individual spots within the transverse spatial beam profile of this filament position are presented, with Fig. 4.14(d) being identical to Fig. 4.8, showing the spectrogram of the pulse center. The time-frequency analysis of the transverse beam profile unveils small differences in the spatio-temporal properties across the beam. While the top area of the profile is very similar to the center, having been described earlier in Sec. 4.2.2 and visualized in Fig. 4.8, the left, right, and bottom areas possess clearly different spectrograms. On the left, the pre-pulse and the main pulse have a similar weight in relative intensity, in fact the pre-pulse is even slightly more intense. The spectrogram of the bottom area shows an equal relative intensity of the main and the pre-pulse and, additionally, has more pulse energy retained in the temporal pulse background. However, the

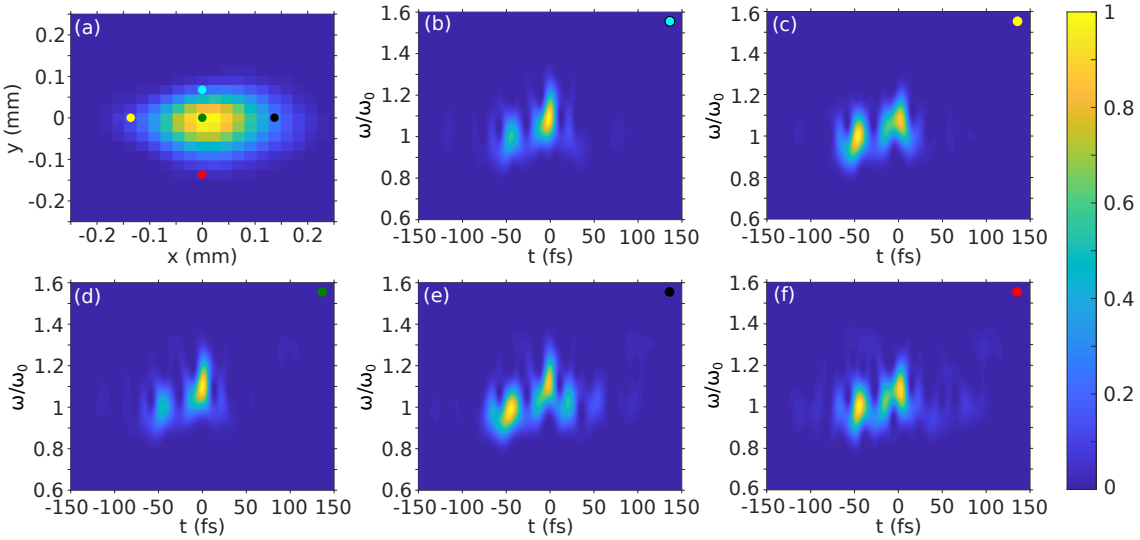

Figure 4.14: Normalized spectrograms of individual spots within the transverse spatial beam profile for the last filament position $d = 150\,\text{mm}$. The frequency $\omega_0 = 2.31\,\text{rad/fs}$ corresponds to the central frequency of the input spectrum.

strongest deviation from the center is present in the right area of the transverse beam profile. Not only is the pre-pulse clearly more intense than the main pulse, but also a post-pulse feature at around 25 fs with significant signal strength can be observed. Nonetheless, for all spectrograms of the different spatial positions, the main pulse has the broadest spectrum and is therefore the clear driver of nonlinear pulse propagation across the whole beam profile. The asymmetry in the spatio-temporal properties of the transverse beam profile of the last filament position is, in a weaker distinctness, already observed for the first filament position and is likely already present in the fundamental beam sent in to the filamentation stage. However, the nonlinear filament dynamics emphasize the asymmetry in the spatio-temporal properties, indicating the need for adequate beam cleaning before using filament beams for experiments that are sensitive to the beam profile. The often mentioned filamentation effect "self-cleaning" that leads to beam cleaning of a filamenting pulse, described in Sec. 2.1.2, is not obvious for the STCs that can be observed with this experimental method.

In the following a brief summary and discussion of all experimental results presented in this chapter is given, evaluating the performance of the presented complete spatio-temporal characterization method for femtosecond filaments.

4.3 Discussion and summary

The complete spatio-temporal pulse characterization technique introduced in this chapter provides a unique access into the dynamics of femtosecond filamentation. Via spectral and temporal analysis it is revealed, that the generated argon filament shows typical spectral broadening of the pulse spectrum over its length as well as self-compression of the main pulse. Further, the main pulse splits during nonlinear propagation, a property of the filament that, along with the spectral broadening, can be reproduced in simulations based on the experimental parameters. In addition to the splitting of the main pulse, a pre-pulse can be observed that persists over the whole length of the filament. With existing filament characterization schemes it could not have been clarified, whether, or to what degree, the pre-pulse contributes to the nonlinear pulse propagation dynamics. However, with this method, the analysis can be expanded to spatio-temporal properties of the pulse, enabling a deeper analysis of the filament dynamics. Via time-frequency analysis, it can be shown that the spectrum of the pre-pulse is unbroadened, i.e. the pre-pulse does not reach the intensity required for contributing significantly to the nonlinear propagation. With the expansion of the analysis to combinations of two-dimensional pulse representations, a STC at around 770 nm is observable in the spatio-spectral and reciprocal-spectral domain. A study of the transverse spatial beam profile of the last filament position, via time-frequency analysis, unveils asymmetries in its spatio-temporal properties, while the three-dimensional representation provides an excellent overview over the macroscopic pulse properties. It reproduces pulse features observed in the earlier temporal and spatio-temporal visualizations of that termination position. With the filament characterization method presented here, a complete spatio-temporal characterization of a femtosecond filament along its length could be performed.

Overall it can be concluded, that this method is a universal tool for the characterization of femtosecond filaments and a good addition to earlier methods. Current drawbacks of the method are given by the pinhole size of the termination plate and the limitations on the characterizable pulse durations given by the d-scan method. Further, for a typical amplifier system with a repetition rate in the kHz range, the method inherently is multi-shot. The current pinhole size of the termination

plate prohibits the analysis of the reservoir as well as of the conical emission and sometimes, depending on the distance of the investigated filament position with respect to the geometrical focus, partially blocks portions of the pulse which does not have a high enough intensity to self-focus. This partial beam blocking potentially leads to misreadings on the relative intensity of less-intense pulse features and limits the observable reciprocal beam space, also referred to as "$k_\perp$-space". The current configuration of the d-scan setup limits the characterization to filament pulses with a Fourier-transform-limited pulse duration of less than 10-15 fs. The analysis of longer pulses is theoretically possible, though, by adapting the chirp management by the wedges and the DCMs. However, despite the mentioned limitations of this method, it proves to be an optimal tool to investigate the effect of spatio-temporal pulse shaping on the femtosecond filament propagation dynamics. This method can lead to a very detailed understanding of filament dynamics with the possible goal to spatio-temporally shape the filament to ones own desire with regard to any application of interest.

CHAPTER 5

Conclusion and outlook

5.1 Conclusion

In this thesis, it was shown that femtosecond filamentation can be used to study the temporal evolution of laser-induced plasma via TH enhancement. Furthermore, a novel method for the complete spatio-temporal characterization of filaments along their length was introduced. Its potential in revealing complex spatio-temporal dynamics was demonstrated. Both experiments combined could show that a femtosecond filament is a truly versatile nonlinear propagation phenomenon, suitable both as a tool to investigate fundamental physics and for a broad range of applications. Its utilization requires comprehensive characterization of the filament pulse propagation dynamics by a complete spatio-temporal characterization method such as the one introduced in this thesis.

In Chapter 3 it was shown, that plasma-induced TH enhancement is a powerful method for the direct determination of the temporal evolution of laser-induced plasma. In an interferometric scheme, in which the beam in one arm is loosely focused to generate a femtosecond filament and the beam in the other arm (called pump beam) is tightly focused to generate a dense plasma spot, the TH enhancement was measured as a function of the delay between the two arms. The investigation encompassed measurements in the gas atmospheres of the atomic gases helium, argon, and xenon as well as in the atmospheres of the molecular gases carbon dioxide, nitrogen and air (as a mostly molecular gas mixture). A parameter study, comprising the pulse energy, the polarization of the light, the pulse duration, and the gas pressure was performed. For the investigated range of these parameters, they showed no significant influence

on the TH enhancement. Hence, measurements in the atmospheres of the different gases that were performed at slightly different pressures and pulse energies could be compared. Severe differences between the decay of the plasmas of the two gas types were found. Whereas the molecular gas plasmas decay directly after having reached the maximum plasma density in a similar time frame of about 10 ps to $1/e$, the atomic gas plasmas decay not earlier than after ≈ 440 ps (in the case of xenon). Further, the atomic gas plasmas show a large spread in their respective lifetimes with the lifetime of argon being around 4.5 ns and a lifetime of helium being greater than the maximal scan range of about 5 ns. The striking discrepancy between the decays of the plasmas of the two gas types and between the atomic gases is explained by differences in their energy state density affecting dynamics of the recombination process: the rate of the three-body electron-ion collisions, the dominating recombination process for femtosecond laser-induced plasma, is strongly nonlinearly dependent on the inverse of the free electron temperature. Hence, in plasmas in which the free electron temperature decreases faster than in others, also the recombination rate is severely larger, i.e. the plasma lifetime is shorter. The decrease in the free electron temperature is driven by non-recombining elastic collisions between free electrons and inelastic collisions between free electrons and heavy particles, i.e. neutral atoms and molecules as well as charged ions. Due to the existence of vibrational and rotational levels in molecular gases, the state density is severely higher than for atomic gases, leading to a higher cross section for non-recombining inelastic electron-heavy particle collisions. The same principle applies to the atomic gases: xenon has a higher state density than argon, which again has a higher state density than helium. The inelastic electron-heavy particle collisional cross section is therefore higher from xenon to helium. In addition to the plasma evolution studies, the TH enhancement itself was investigated in a temporal window of around 2.5 ps from zero delay. An unexpected local minimum after the maximum of enhancement, that is not resolved in the plasma evolution scans with a larger temporal stepping, was found for all gases. The contrast between the first peak and the subsequent minimum shows a nonlinear dependency on the pulse energy. Furthermore, the onset of TH enhancement is pulse energy dependent: the higher the pulse energy of the beam that generates the plasma spot, the earlier in time is

the onset. In contrast to the decay in TH enhancement on larger timescales that can clearly be attributed to be caused by the laser-induced plasma, the fundamental mechanism for TH enhancement at short timescale, is not entirely clear. It is assumed that the observed dynamics are mainly caused by a two-beam coupling process in which the pump-driven Kerr nonlinearity shows a non-instantaneous response affecting the filament pulse. As the Kerr response is intensity-dependent, there is also a dependency of the TH enhancement dynamics on the pump pulse energy. However, also plasma expansion dynamics might affect the observed trends.

In Chapter 4, a novel method for a complete spatio-temporal characterization of a femtosecond filament along its length is presented. A femtosecond filament in argon atmosphere with a length of 20 cm is terminated at 9 different positions over a distance of 15 cm along its length. The filamenting pulse is characterized via spatially resolved Fourier transform spectrometry in combination with dispersion scan. The measured spatio-temporally-resolved filament pulse profiles are numerically backpropagated to the termination point via a Fourier optics plane wave propagator. In this way, the method provides an in-situ four-dimensional analysis of the filament propagation dynamics. The access to this complete filament pulse information is used to analyze the filament in one-, two- and three-dimensional pulse representations. The one-dimensional analysis is performed in the temporal and spectral domain for the pulse center, as the spatially-averaged pulse shows the same trend. The results are compared to filament pulse simulations based on the unidirectional pulse propagation equation. An excellent agreement between the measured and the simulated spectra and a good agreement between the temporal evolution in the simulations and the measurement is found. The spectral evolution shows a clear broadening towards longer filaments, while the temporal evolution shows a pulse splitting of the main pulse that manifests as a clear double pulse with a separation of around 20 fs at the end of the filament scan range. In the measurement also a pre- and a post-pulse are observed. Via short-time Fourier transform analysis, applied to the filament pulse at the end of the scan range, enabling a spectral analysis of different time segments of a temporal distribution, it is verified that only the main pulse is significantly broadened. From that analysis it is concluded, that the main pulse dominates the nonlinear pulse propagation. Via two-dimensional pulse representations in the form

$x - t$ (spatio-temporal), $x - \lambda$ (spatio-spectral) and $k_x/k_0 - \lambda$ (reciprocal-spectral) at four equidistant filament lengths, a more in-depth analysis of the spatio-temporal properties of the filament pulse propagation is performed. The spatio-temporal pulse evolution shows, that the main pulse shortens during its propagation along the filament and becomes more intense. Furthermore, the pulse splitting of the main pulse and the temporal separation of the respective sub-pulses, already observed in the pure temporal pulse representation, is clearly reproduced. The spatio-spectral filament pulse analysis reveals an anomaly at around 770 nm that is off-center with respect to the center of mass of the spatio-spectral pulse distribution. The shift of the pulse feature increases towards the end of the filament. This pulse feature, assumed to be an artefact from the pulse compressor of the amplifier system, is a clear indication of a spatio-temporal coupling in the filament pulse properties. Its detection demonstrates that the presented method is capable of revealing complex filament propagation dynamics. In addition to the shifted spectral feature, a slight spatial chirp of the filament pulse can be observed towards the end of the filament. The analysis of the angular spread as a function of the wavelength over length of the filament reveals that the pulse feature at 770 nm has a slightly different propagation angle than the rest of the distribution, underlining that it originates from before the generation of the filament. The novel three-dimensional representation of a filament pulse in real space, in this case of the last filament position, provides a comprehensive overview of the pulse properties that were retrieved from the previous one- and two-dimensional filament pulse representations. A short-time Fourier transform analysis of the filament pulse properties along the transversal beam profile, at the end of the characterized filament length, exposes an asymmetry towards the bottom and the left and right edges of the distribution. There, the pre-pulse, despite the main pulse still having the broadest spectrum, becomes as intense as the main pulse. As in the case of the anomaly in the spatio-spectral pulse analysis, it is assumed that the asymmetry in the transversal beam profile also originates from the laser amplifier before the filament stage.

5.2 Outlook

The determination of the lifetime of femtosecond laser-induced plasma via TH enhancement proves to be a straightforward and simple approach for that investigation of fundamental physics. The major limitations of the current method are given by the maximal temporal window that can be scanned and the fact that only the relative trend of the temporal plasma evolution, i.e. of the free electron density, can be analyzed. No absolute free electron density can be attributed to any temporal delay in the measurement at the moment. By extending the method towards a determination of the absolute free electron density, for instance by combining it to existing methods that are capable of that (see Sec. 2.3.4), a quantitative analysis of the temporal plasma evolution can be performed. These methods even provide some transverse spatial resolution on the free electron density, potentially adding a completely new dimension to the laser-induced temporal plasma analysis. Another important plasma parameter is the free electron temperature, relevant especially for the plasma recombination dynamics. By establishing a time-resolved detection of the plasma fluorescence spectral distribution, the evolution of the free electron temperature can be studied simultaneously to the one of the free electron density: the plasma temperature leads to a Planck distribution of the fluorescence spectrum from which the former can be derived. Since the fluorescence spectrum will also contain characteristic line emissions of the ions and neutral atoms and molecules involved in the recombination process, the time-resolved spectral analysis will also show what constituents of the plasma are present at which moment during the plasma recombination. This information will deepen the understanding of the involved recombination processes. By extending the current method to measurements of the absolute free electron density and temperature, the plasma recombination dynamics can be analyzed comprehensively and new insights of the involved dynamics can be gained. Simply expanding the scan range of the current setup, will already answer the question of the lifetime of helium plasma and it can be compared to the ones of argon and xenon plasma. In the perspective of the analysis of the rare gases, it will also be interesting to determine the lifetime of neon and krypton plasmas. Additionally, it will be interesting to measure the lifetime of molecular oxygen plasma

and compare its lifetime to the one of air plasma. A very similar lifetime is expected. For the analysis of the fundamental mechanisms of plasma recombination, it will be interesting to extend the parameter analysis to a wider range of values. At some point, the observed independence of the plasma evolution on these parameters must end and it will be interesting to determine when that takes place for every studied parameter and with which relation to its tuning. Likewise, a clearer analysis of the involved pulse intensity is crucial, so that it can be added as an independent parameter to the existing parameter set and be distinguished from the pulse energy. In terms of the plasma lifetime determination method itself, it will be compelling to establish it not only in a gaseous environment but also in transparent dense media, e.g. in water. In that way, the amount of materials whose plasma can be studied could be greatly expanded. Besides the possibilities to expand the analysis of the plasma evolution, it is also intriguing to further investigate the TH enhancement itself. The conversion efficiency from the fundamental pulse energy to TH pulse energy could be quantified and ways to increase it be studied, since TH enhancement offers the possibility for the generation of ultrashort UV pulses with a relatively high pulse energy. Therefore, also the spatial properties of the enhanced TH beam should be investigated and possible parameter dependencies be studied.

The presented complete spatio-temporal characterization method of a filamenting pulse along the length of the filament proofs to be capable of determining complex nonlinear propagation dynamics. The method can easily be extended by scanning more filament positions than the 9 that were scanned in the presented experiment. By increasing the amount of scanned positions, the dynamics can be studied in more detail and, for instance with the three-dimensional pulse representation, a movie of the pulse filament evolution can be generated. Additionally, the parameters pulse energy and duration as well as gas pressure can be tuned more to investigate their influence on the filament dynamics. In this way, the validity of the scaling invariance of femtosecond filament proposed in [Hey16] can be examined. In addition to the investigation of these intrinsic filament parameters, the spatial and temporal profile of the fundamental pulse sent into the filament stage could be shaped, for instance into the increasingly interesting form of a cylindrical vector beam profile [Zha09; Nai16], and the influence on the filament dynamics be studied. In combination with

a pulse shaper for amplitude and phase, the current method could be integrated into an optimization loop to tailor the filament pulse properties for any application of interest. Especially interesting would be the optimization of intensity spikes which could enable the generation of isolated attosecond pulses as proposed in [Cou08; Gaa09]. Alternatively, the filament pulse could be optimized for the generation of high order harmonics. Also simulations could be integrated into that optimization process in order to predict potentially interesting parameter sets for the generation of a filament that can be examined in the experiment. On the long run, this approach might enable the generation of tailored filaments proposed by simulations. Furthermore, the existing method can be applied to other gases than argon and it can easily be adapted to short- and large-scale filaments or two-colour filaments that have fascinating properties such as possibility to generate intense THz-radiation [Kou20]. Challenging but interesting would be to send a second fundamental pulse, or even multiple pulses, into the filamentation stage to generate, for instance, a plasma grating structure at the termination point and investigate the influence of filament interaction on the pulse dynamics. For further analysis of the impact of laser-induced plasma on the filament dynamics, e.g. in the aforementioned case of the plasma grating structure, an additional characterization method could be integrated into the current setup to determine the absolute free electron density along the length of the filament. This analysis would also support the simulations of filament dynamics, as the free electron density is an important parameter for any filament simulation. Furthermore, every application targeting at the electric properties of a filament, such as electric guiding of external discharges as in the case of the "laser lightning rod project" [Pro21], that aims at guiding atmospheric lightning, would benefit from the study of the free electron density. A fascinating modification of the setup, on the long run, would be to install a single-shot characterization scheme, which is currently not possible due to the necessary scanning and integration of multiple images in the spatially-resolved Fourier spectrometry setup, while a single-shot d-scan setup could be installed already. Moreover, due to its small size, the pinhole in the termination plate prohibits an analysis of the filament reservoir and the conical emission and it blocks parts of the filament core that do not, or at least not significantly, self-focus during filament propagation and exceed the hole size. A re-design of the current

termination idea, for instance with a thin glass plate instead of a metal plate could already bring improvements since the glass would be transparent also for the outer parts of the beam distribution with the reservoir and the conical emission. Another idea for improvement on the termination approach would be to install a beam steering setup for the filament stage. By a controlled movement of the beam, the hole in the termination plate could be enlarged slightly and the aforementioned problems with its current size be reduced, while still maintaining a sharp pressure gradient for the filament termination. In this way, also a larger k-space of the filament pulse in the core could be measured which would further improve the spatio-temporal analysis of the filament, allowing to resolve structures like the so-called X-waves in the nonlinear regime [Con03], attributed to observations made in femtosecond filaments in water [Maj11] and air [Fac08]. With a termination in form of a glass plate, the characterization method might also be adapted to filaments in water. Transparent solids would already offer a termination surface at their end facet for filamentation inside them and could already be integrated into the current setup.

In summary, it can be said that both experiments possess various opportunities to advance the understanding of fundamental physical processes in the strong field regime of nonlinear optics and push the field of femtosecond filaments into many new directions for further experiments and applications.

Bibliography

[Ada63] Adams, J. B., M. A. Ruderman, and C.-H. Woo: 'Neutrino Pair Emission by a Stellar Plasma'. *Phys. Rev.* (1963), vol. 129(3): pp. 1383–1390. doi: 10.1103/PhysRev.129.1383 (cit. on p. 19).

[Akö01] Aközbek, N., M. Scalora, C. M. Bowden, and S. L. Chin: 'White-light continuum generation and filamentation during the propagation of ultra-short laser pulses in air'. *Opt. Commun.* (2001), vol. 191(3): pp. 353–362. doi: 10.1016/S0030-4018(01)01113-0 (cit. on pp. 19, 38).

[Akö02] Aközbek, N., A. Iwasaki, A. Becker, M. Scalora, S. L. Chin, and C. M. Bowden: 'Third-Harmonic Generation and Self-Channeling in Air Using High-Power Femtosecond Laser Pulses'. *Phys. Rev. Lett.* (2002), vol. 89(14): p. 143901. doi: 10.1103/PhysRevLett.89.143901 (cit. on pp. 4, 37, 38).

[Akö06] Aközbek, N., S. A. Trushin, A. Baltuška, W. Fuss, E. Goulielmakis, K. Kosma, F. Krausz, S. Panja, M. Uiberacker, W. E. Schmid, A. Becker, M. Scalora, and M. Bloemer: 'Extending the supercontinuum spectrum down to 200 nm with few-cycle pulses'. *New J. Phys.* (2006), vol. 8(9): pp. 177–177. doi: 10.1088/1367-2630/8/9/177 (cit. on p. 19).

[Akt07] Akturk, S., C. D'Amico, M. Franco, A. Couairon, and A. Mysyrowicz: 'Pulse shortening, spatial mode cleaning, and intense terahertz generation by filamentation in xenon'. *Phys. Rev. A* (2007), vol. 76(6): p. 063819. doi: 10.1103/PhysRevA.76.063819 (cit. on p. 12).

[Akt08] Akturk, S., A. Couairon, M. Franco, and A. Mysyrowicz: 'Spectrogram representation of pulse self compression by filamentation'. *Opt. Express* (2008), vol. 16(22): pp. 17626–17636. doi: 10.1364/OE.16.017626 (cit. on p. 103).

[Akt10] Akturk, S., X. Gu, P. Bowlan, and R. Trebino: 'Spatio-temporal couplings in ultrashort laser pulses'. *J. Opt.* (2010), vol. 12(9): p. 093001. doi: 10.1088/2040-8978/12/9/093001 (cit. on pp. 40–42).

[Ale16] Aleksandrov, N. L., S. B. Bodrov, M. V. Tsarev, A. A. Murzanev, Yu. A. Sergeev, Yu. A. Malkov, and A. N. Stepanov: 'Decay of femtosecond laser-induced plasma filaments in air, nitrogen, and argon for atmospheric and subatmospheric pressures'. *Phys. Rev. E* (2016), vol. 94(1): p. 013204. doi: 10.1103/PhysRevE.94.013204 (cit. on p. 22).

[Amm86] Ammosov, M. V.: 'Tunnel ionization of complex atoms and of atomic ions in an alternating electromagnetic field'. *Sov. Phys. JETP* (1986), vol. 64(6): pp. 1191–1194 (cit. on pp. 24, 25).

[App21] Appi, E., C. C. Papadopoulou, J. L. Mapa, C. Jusko, P. Mosel, A. Schoenberg, J. Stock, T. Feigl, S. Ališauskas, T. Lang, C. M. Heyl, B. Manschwetus, M. Brachmanski, M. Braune, H. Lindenblatt, F. Trost, S. Meister, P. Schoch, A. Trabattoni, F. Calegari, R. Treusch, R. Moshammer, I. Hartl, U. Morgner, and M. Kovacev: 'Synchronized beamline at FLASH2 based on high-order harmonic generation for two-color dynamics studies'. *Rev. Sci. Instrum.* (2021), vol. 92(12): p. 123004. doi: 10.1063/5.0063225 (cit. on p. 3).

[Aug12] Auguste, T., O. Gobert, C. F. Dutin, A. Dubrouil, E. Mével, S. Petit, E. Constant, and D. Descamps: 'Application of optical-field-ionization-induced spectral broadening in helium gas to the post-compression of high-energy femtosecond laser pulses'. *J. Opt. Soc. Am. B* (2012), vol. 29(6): pp. 1277–1286. doi: 10.1364/JOSAB.29.001277 (cit. on p. 2).

[Bai12] Bai, Y., L. Song, R. Xu, C. Li, P. Liu, Z. Zeng, Z. Zhang, H. Lu, R. Li, and Z. Xu: 'Waveform-Controlled Terahertz Radiation from the Air Filament Produced by Few-Cycle Laser Pulses'. *Phys. Rev. Lett.* (2012), vol. 108(25): p. 255004. doi: 10.1103/PhysRevLett.108.255004 (cit. on p. 37).

[Bal20] Balla, P., A. B. Wahid, I. Sytcevich, C. Guo, A.-L. Viotti, L. Silletti, A. Cartella, S. Alisauskas, H. Tavakol, U. Grosse-Wortmann, A. Schönberg, M. Seidel, A. Trabattoni, B. Manschwetus, T. Lang, F. Calegari, A. Couairon, A. L'Huillier, C. L. Arnold, I. Hartl, and C. M. Heyl: 'Postcompression of picosecond pulses into the few-cycle regime'. *Opt. Lett.* (2020), vol. 45(9): pp. 2572–2575. doi: 10.1364/OL.388665 (cit. on p. 3).

[Bat10] Bates, P. K., O. Chalus, and J. Biegert: 'Ultrashort pulse characterization in the mid-infrared'. *Opt. Lett.* (2010), vol. 35(9): pp. 1377–1379. doi: 10.1364/OL.35.001377 (cit. on p. 50).

[Béj07] Béjot, P. et al.: '32 TW atmospheric white-light laser'. *Appl. Phys. Lett.* (2007), vol. 90(15): p. 151106. doi: 10.1063/1.2722564 (cit. on pp. 3, 8).

[Bék03] Békési, J., J.-H. Klein-Wiele, and P. Simon: 'Efficient submicron processing of metals with femtosecond UV pulses'. *Appl. Phys. A* (2003), vol. 76(3): pp. 355–357. doi: 10.1007/s00339-002-1820-y (cit. on p. 40).

[Ber03] Bergé, L., C. Gouédard, J. Schjødt-Eriksen, and H. Ward: 'Filamentation patterns in Kerr media vs. beam shape robustness, nonlinear saturation and polarization states'. *Physica D* (2003), vol. 176(3): pp. 181–211. doi: 10.1016/S0167-2789(02)00740-6 (cit. on p. 13).

[Ber04] Bergé, L., S. Skupin, F. Lederer, G. Méjean, J. Yu, J. Kasparian, E. Salmon, J. P. Wolf, M. Rodriguez, L. Wöste, R. Bourayou, and R. Sauerbrey: 'Multiple Filamentation of Terawatt Laser Pulses

in Air'. *Phys. Rev. Lett.* (2004), vol. 92(22): p. 225002. DOI: 10.1103/PhysRevLett.92.225002 (cit. on pp. 12, 13).

[Bes66] Bespalov, V. I. and V. I. Talanov: 'Filamentary structure of light beams in nonlinear liquids'. *JETP Lett.* (1966), vol. 3: p. 307 (cit. on p. 13).

[Blo73] Bloembergen, N.: 'The influence of electron plasma formation on superbroadening in light filaments'. *Opt. Commun.* (1973), vol. 8(4): pp. 285–288. DOI: 10.1016/0030-4018(73)90196-X (cit. on p. 11).

[Böh14] Böhle, F., M. Kretschmar, A. Jullien, M. Kovacs, M. Miranda, R. Romero, H. Crespo, U. Morgner, P. Simon, R. Lopez-Martens, and T. Nagy: 'Compression of CEP-stable multi-mJ laser pulses down to 4 fs in long hollow fibers'. *Laser Phys. Lett.* (2014), vol. 11(9): p. 095401. DOI: 10.1088/1612-2011/11/9/095401 (cit. on pp. 3, 18).

[Bor18] Borot, A. and F. Quéré: 'Spatio-spectral metrology at focus of ultrashort lasers: a phase-retrieval approach'. *Opt. Express* (2018), vol. 26(20): pp. 26444–26461. DOI: 10.1364/OE.26.026444 (cit. on p. 48).

[Bor89a] Bor, Z.: 'Distortion of femtosecond laser pulses in lenses'. *Opt. Lett.* (1989), vol. 14(2): pp. 119–121. DOI: 10.1364/OL.14.000119 (cit. on p. 41).

[Bor89b] Bor, Z., Z. Gogolak, and G. Szabo: 'Femtosecond-resolution pulse-front distortion measurement by time-of-flight interferometry'. *Opt. Lett.* (1989), vol. 14(16): pp. 862–864. DOI: 10.1364/OL.14.000862 (cit. on p. 41).

[Bor92] Bor, Z. and Z. L. Horváth: 'Distortion of femtosecond pulses in lenses. Wave optical description'. *Opt. Commun.* (1992), vol. 94(4): pp. 249–258. DOI: 10.1016/0030-4018(92)90022-J (cit. on p. 41).

[Boy08] Boyd, R. W.: *Nonlinear Optics*. Third Edition. Academic Press, Burlington, 2008 (cit. on pp. 15, 16, 24).

[Boy09] Boyd, R. W., S. G. Lukishova, and Y. R. Shen: *Self-focusing: Past and Present*. Springer-Verlag, New York, 2009. doi: 10.1007/978-0-387-34727-1 (cit. on pp. 20, 22).

[Boy80] Boyd, R. W.: 'Intuitive explanation of the phase anomaly of focused light beams'. *J. Opt. Soc. Am.* (1980), vol. 70(7): pp. 877–880. doi: 10.1364/JOSA.70.000877 (cit. on p. 37).

[Bra00] Brabec, T. and F. Krausz: 'Intense few-cycle laser fields: Frontiers of nonlinear optics'. *Rev. Mod. Phys.* (2000), vol. 72(2): pp. 545–591. doi: 10.1103/RevModPhys.72.545 (cit. on p. 1).

[Bra95] Braun, A., G. Korn, X. Liu, D. Du, J. Squier, and G. Mourou: 'Self-channeling of high-peak-power femtosecond laser pulses in air'. *Opt. Lett.* (1995), vol. 20(1): pp. 73–75. doi: 10.1364/OL.20.000073 (cit. on pp. 2, 21, 31).

[Bra97] Brabec, T. and F. Krausz: 'Nonlinear Optical Pulse Propagation in the Single-Cycle Regime'. *Phys. Rev. Lett.* (1997), vol. 78(17): pp. 3282–3285. doi: 10.1103/PhysRevLett.78.3282 (cit. on p. 33).

[Bré09] Brée, C., A. Demircan, S. Skupin, L. Bergé, and G. Steinmeyer: 'Self-pinching of pulsed laser beams during filamentary propagation'. *Opt. Express* (2009), vol. 17(19): pp. 16429–16435. doi: 10.1364/OE.17.016429 (cit. on p. 33).

[Bré10] Brée, C., J. Bethge, L. Skupin S.and Bergé, A.. Demircan, and G. Steinmeyer: 'Cascaded self-compression of femtosecond pulses in filaments'. *New J. Phys.* (2010), vol. 12(9): p. 093046. doi: 10.1088/1367-2630/12/9/093046 (cit. on p. 33).

[Bré12] Brée, C.: 'Nonlinear optics in the filamentation regime'. PhD thesis. Humboldt-Universität zu Berlin, 2012. doi: 10.1007/978-3-642-30930-4 (cit. on p. 33).

[Bri96] Brimblecombe, P.: *Air composition & chemistry*. Second. Cambridge University Press, Cambridge, 1996 (cit. on p. 69).

[Bro19] Brown, J. M., A. Couairon, P. Polynkin, and M. B. Gaarde: 'Analysis of the angular spectrum for ultrashort laser pulses'. *J. Opt. Soc. Am. B* (2019), vol. 36(2): A105–A111. doi: 10.1364/JOSAB.36.00A105 (cit. on p. 99).

[Bro97] Brodeur, A., C. Y. Chien, F. A. Ilkov, S. L. Chin, O. G. Kosareva, and V. P. Kandidov: 'Moving focus in the propagation of ultrashort laser pulses in air'. *Opt. Lett.* (1997), vol. 22(5): pp. 304–306. doi: 10.1364/OL.22.000304 (cit. on pp. 10, 30, 87).

[Bur05] Burgin, J., C. Guillon, and P. Langot: 'Femtosecond investigation of the non-instantaneous third-order nonlinear suceptibility in liquids and glasses'. *Appl. Phys. Lett.* (2005), vol. 87(21): p. 211916. doi: 10.1063/1.2136413 (cit. on p. 84).

[Can17] Canhota, M., F. Silva, R. Weigand, and H. M. Crespo: 'Inline self-diffraction dispersion-scan of over octave-spanning pulses in the single-cycle regime'. *Opt. Lett.* (2017), vol. 42(15): pp. 3048–3051. doi: 10.1364/OL.42.003048 (cit. on p. 51).

[Cap00] Capitelli, M., F. Capitelli, and A. Eletskii: 'Non-equilibrium and equilibrium problems in laser-induced plasmas'. *Spectrochim. Acta B* (2000), vol. 55(6): pp. 559–574. doi: 10.1016/S0584-8547(00)00168-3 (cit. on pp. 22, 23, 26, 27, 75).

[Cap04] Capitelli, M., A. Casavola, G. Colonna, and A. De Giacomo: 'Laser-induced plasma expansion: theoretical and experimental aspects'. *Spectrochim. Acta B* (2004), vol. 59(3): pp. 271–289. doi: 10.1016/j.sab.2003.12.017 (cit. on p. 19).

[Cha06] Chakraborty, H. S., M. B. Gaarde, and A. Couairon: 'Single attosecond pulses from high harmonics driven by self-compressed filaments'. *Opt. Lett.* (2006), vol. 31(24): pp. 3662–3664. doi: 10.1364/OL.31.003662 (cit. on p. 35).

[Che16] Cheng, Y.-C., C.-H. Lu, Y.-Y. Lin, and A. H. Kung: 'Supercontinuum generation in a multi-plate medium'. *Opt. Express* (2016), vol. 24(7): pp. 7224–7231. doi: 10.1364/OE.24.007224 (cit. on pp. 3, 18).

[Chi02] Chin, S. L., A. Talebpour, J. Yang, S. Petit, V. P. Kandidov, O. G. Kosareva, and M. P. Tamarov: 'Filamentation of femtosecond laser pulses in turbulent air'. *Appl. Phys. B* (2002), vol. 74(1): pp. 67–76. doi: 10.1007/s003400100738 (cit. on p. 9).

[Chi07] Chin, S. L., F. Théberge, and W. Liu: 'Filamentation nonlinear optics'. *Appl. Phys. B* (2007), vol. 86(3): pp. 477–483. doi: 10.1007/s00340-006-2455-z (cit. on p. 12).

[Chi10] Chin, S. L.: *Femtosecond Laser Filamentation*. Springer-Verlag New York, 2010. doi: 10.1007/978-1-4419-0688-5 (cit. on pp. 16, 18, 19, 21, 22, 35).

[Chi64] Chiao, R. Y., E. Garmire, and C. H. Townes: 'Self-Trapping of Optical Beams'. *Phys. Rev. Lett.* (1964), vol. 13(15): pp. 479–482. doi: 10.1103/PhysRevLett.13.479 (cit. on p. 31).

[Cle95] Clement, T. S., A. J. Taylor, and D. J. Kane: 'Single-shot measurement of the amplitude and phase of ultrashort laser pulses in the violet'. *Opt. Lett.* (1995), vol. 20(1): pp. 70–72. doi: 10.1364/OL.20.000070 (cit. on p. 51).

[Coe08] Coello, Y., V. V. Lozovoy, T. C. Gunaratne, B. Xu, I. Borukhovich, C.-h. Tseng, T. Weinacht, and M. Dantus: 'Interference without an interferometer: a different approach to measuring, compressing, and shaping ultrashort laser pulses'. *J. Opt. Soc. Am. B* (2008), vol. 25(6): A140–A150. doi: 10.1364/JOSAB.25.00A140 (cit. on p. 50).

[Con03] Conti, C., S. Trillo, P. Di Trapani, G. Valiulis, A. Piskarskas, O. Jedrkiewicz, and J. Trull: 'Nonlinear Electromagnetic X Waves'. *Phys. Rev. Lett.* (2003), vol. 90(17): p. 170406. doi: 10.1103/PhysRevLett.90.170406 (cit. on pp. 11, 122).

[Cor07] Corkum, P. B. and F. Krausz: 'Attosecond science'. *Nat. Phys.* (2007), vol. 3(6): pp. 381–387. doi: 10.1038/nphys620 (cit. on p. 1).

[Cor93] Corkum, P. B.: 'Plasma perspective on strong field multiphoton ionization'. *Phys. Rev. Lett.* (1993), vol. 71(13): pp. 1994–1997. doi: 10.1103/PhysRevLett.71.1994 (cit. on p. 25).

[Cou02] Couairon, A., S. Tzortzakis, L. Bergé, M. Franco, B. Prade, and A. Mysyrowicz: 'Infrared femtosecond light filaments in air: simulations and experiments'. *J. Opt. Soc. Am. B* (2002), vol. 19(5): pp. 1117–1131. doi: 10.1364/JOSAB.19.001117 (cit. on p. 87).

[Cou03] Couairon, A.: 'Light bullets from femtosecond filamentation'. *Eur. Phys. J. D* (2003), vol. 27: pp. 159–167. doi: 10.1140/epjd/e2003-00255-9 (cit. on p. 31).

[Cou05] Couairon, A., M. Franco, A. Mysyrowicz, J. Biegert, and U. Keller: 'Pulse self-compression to the single-cycle limit by filamentation in a gas with a pressure gradient'. *Opt. Lett.* (2005), vol. 30(19): pp. 2657–2659. doi: 10.1364/OL.30.002657 (cit. on p. 34).

[Cou06] Couairon, A., J. Biegert, C. P. Hauri, W. Kornelis, F. W. Helbing, U. Keller, and A. Mysyrowicz: 'Self-compression of ultrashort laser pulses down to one optical cycle by filamentation'. *J. Mod. Opt.* (2006), vol. 53(1-2): pp. 75–85. doi: 10.1080/09500340500227760 (cit. on pp. 34, 35).

[Cou07] Couairon, A. and A. Mysyrowicz: 'Femtosecond filamentation in transparent media'. *Phys. Rep.* (2007), vol. 441(2): pp. 47–189. doi: 10.1016/j.physrep.2006.12.005 (cit. on pp. 2, 8–11, 17–20, 22, 24, 25, 31, 32, 34, 35, 38, 87).

[Cou08] Couairon, A., H. S. Chakraborty, and M. B. Gaarde: 'From single-cycle self-compressed filaments to isolated attosecond pulses in noble gases'. *Phys. Rev. A* (2008), vol. 77(5): p. 053814. doi: 10.1103/PhysRevA.77.053814 (cit. on pp. 35, 99, 121).

[Cour03] Courvoisier, F., V. Boutou, J. Kasparian, E. Salmon, G. Méjean, J. Yu, and J.-P. Wolf: 'Ultraintense light filaments transmitted through clouds'. *Appl. Phys. Lett.* (2003), vol. 83(2): pp. 213–215. doi: 10.1063/1.1592615 (cit. on p. 12).

[Cri13] Cristoforetti, G., E. Tognoni, and L. A. Gizzi: 'Thermodynamic equilibrium states in laser-induced plasmas: From the general case to laser-induced breakdown spectroscopy plasmas'. *Spectrochim. Acta B* (2013), vol. 90: pp. 1–22. doi: 10.1016/j.sab.2013.09.004 (cit. on p. 23).

[Dal60] Dalgarno, A and A. E. Kingston: 'The refractive indices and Verdet constants of the inert gases'. *Proceedings of the Royal Society of London. Series A. Mathematical and Physical Sciences* (1960), vol. 259(1298): pp. 424–431. doi: 10.1098/rspa.1960.0237 (cit. on p. 99).

[DAm07] D'Amico, C., A. Houard, M. Franco, B. Prade, A. Mysyrowicz, A. Couairon, and V. T. Tikhonchuk: 'Conical Forward THz Emission from Femtosecond-Laser-Beam Filamentation in Air'. *Phys. Rev. Lett.* (2007), vol. 98(23): p. 235002. doi: 10.1103/PhysRevLett.98.235002 (cit. on p. 3).

[DAm08] D'Amico, C., A. Houard, S. Akturk, Y. Liu, J. Le Bloas, M. Franco, B. Prade, A. Couairon, V. T. Tikhonchuk, and A. Mysyrowicz: 'Forward THz radiation emission by femtosecond filamentation in gases: theory and experiment'. *New J. Phys.* (2008), vol. 10(1): p. 013015. doi: 10.1088/1367-2630/10/1/013015 (cit. on p. 3).

[Deb19] Debord, B., F. Amrani, L. Vincetti, F. Gérôme, and F. Benabid: 'Hollow-Core Fiber Technology: The Rising of "Gas Photonics"'. *Fibers* (2019), vol. 7(2). doi: 10.3390/fib7020016 (cit. on p. 18).

[DeL94] DeLong, K. W., R. Trebino, and D. J. Kane: 'Comparison of ultrashort-pulse frequency-resolved-optical-gating traces for three common beam geometries'. *J. Opt. Soc. Am. B* (1994), vol. 11(9): pp. 1595–1608. doi: 10.1364/JOSAB.11.001595 (cit. on p. 51).

[Dor20] Doria, D., M.O. Cernaianu, P. Ghenuche, D. Stutman, K.A. Tanaka, C. Ticos, and C.A. Ur: 'Overview of ELI-NP status and laser commissioning experiments with 1 PW and 10 PW class-lasers'. *J. Instrum.* (2020), vol. 15(09): pp. C09053–C09053. doi: 10.1088/1748-0221/15/09/c09053 (cit. on p. 1).

[Dra79] Draine, B. T. and E. E. Salpeter: 'On the physics of dust grains in hot gas'. *Astrophys. J.* (1979), vol. 231: pp. 77–94. doi: 10.1086/157165 (cit. on p. 19).

[Dro04] Dromey, B., S. Kar, M. Zepf, and P. Foster: 'The plasma mirror—A subpicosecond optical switch for ultrahigh power lasers'. *Rev. Sci. Instrum.* (2004), vol. 75(3): pp. 645–649. doi: 10.1063/1.1646737 (cit. on p. 2).

[Dub03] Dubietis, A., G. Tamošauskas, I. Diomin, and A. Varanavičius: 'Self-guided propagation of femtosecond light pulses in water'. *Opt. Lett.* (2003), vol. 28(14): pp. 1269–1271. doi: 10.1364/OL.28.001269 (cit. on p. 9).

[Dub04a] Dubietis, A., E. Gaižauskas, G. Tamošauskas, and P. Di Trapani: 'Light Filaments without Self-Channeling'. *Phys. Rev. Lett.* (2004), vol. 92(25): p. 253903. doi: 10.1103/PhysRevLett.92.253903 (cit. on p. 12).

[Dub04b] Dubietis, A., E. Kučinskas, G. Tamošauskas, E. Gaižauskas, M. A. Porras, and P. Di Trapani: 'Self-reconstruction of light filaments'. *Opt. Lett.* (2004), vol. 29(24): pp. 2893–2895. doi: 10.1364/OL.29.002893 (cit. on p. 12).

[Dub92] Dubietis, A., G. Jonušauskas, and A. Piskarskas: 'Powerful femtosecond pulse generation by chirped and stretched pulse parametric amplification in BBO crystal'. *Opt. Commun.* (1992), vol. 88(4): pp. 437–440. doi: 10.1016/0030-4018(92)90070-8 (cit. on p. 1).

[Dur11] Durand, M., Y. Liu, B. Forestier, A. Houard, and A. Mysyrowicz: 'Experimental observation of a traveling plasma grating formed

by two crossing filaments in gases'. *Appl. Phys. Lett.* (2011), vol. 98(12): p. 121110. DOI: 10.1063/1.3568888 (cit. on p. 2).

[Dur12] DURAND, M., A. JARNAC, Y. LIU, B. PRADE, A. HOUARD, V. TIKHONCHUK, and A. MYSYROWICZ: 'Dynamics of plasma gratings in atomic and molecular gases'. *Phys. Rev. E* (2012), vol. 86(3): p. 036405. DOI: 10.1103/PhysRevE.86.036405 (cit. on pp. 28, 30).

[Dur13] DURAND, M., A. HOUARD, B. PRADE, A. MYSYROWICZ, A.DURÉCU, B. MOREAU, D. FLEURY, O. VASSEUR, H. BORCHERT, K. DIENER, R. SCHMITT, F. THÉBERGE, M. CHATEAUNEUF, J.-F. DAIGLE, and J. DUBOIS: 'Kilometer range filamentation'. *Opt. Express* (2013), vol. 21(22): pp. 26836–26845. DOI: 10.1364/OE.21.026836 (cit. on pp. 3, 8).

[Dzi06] DZIERŻĘGA, K., W. ZAWADZKI, B. POKRZYWKA, and S. PELLERIN: 'Experimental investigations of plasma perturbation in Thomson scattering applied to thermal plasma diagnostics'. *Phys. Rev. E* (2006), vol. 74(2): p. 026404. DOI: 10.1103/PhysRevE.74.026404 (cit. on p. 29).

[Dzi10] DZIERŻĘGA, K., A. MENDYS, S. PELLERIN, E. THOUIN, G. TRAVAILLE, B. BOUSQUET, L. CANIONI, and B. POKRZYWKA: 'Thomson scattering from laser induced plasma in air'. *J. Phys. Conf. Ser.* (2010), vol. 227: p. 012029. DOI: 10.1088/1742-6596/227/1/012029 (cit. on pp. 28, 29).

[Edw14] EDWARDS, M. R., V. T. PLATONENKO, and J. M. MIKHAILOVA: 'Enhanced attosecond bursts of relativistic high-order harmonics driven by two-color fields'. *Opt. Lett.* (2014), vol. 39(24): pp. 6823–6826. DOI: 10.1364/OL.39.006823 (cit. on p. 2).

[Edw20] EDWARDS, M. R. and J. M. MIKHAILOVA: 'The X-Ray Emission Effectiveness of Plasma Mirrors: Reexamining Power-Law Scaling for Relativistic High-Order Harmonic Generation'. *Sci. Rep.* (2020), vol. 10(1): p. 5154. DOI: 10.1038/s41598-020-61255-0 (cit. on p. 2).

[Esa09] ESAREY, E., C. B. SCHROEDER, and W. P. LEEMANS: 'Physics of laser-driven plasma-based electron accelerators'. *Rev. Mod. Phys.* (2009),

vol. 81(3): pp. 1229–1285. DOI: 10.1103/RevModPhys.81.1229 (cit. on p. 2).

[Fab15] Fabris, D., W. Holgado, F. Silva, T. Witting, J. W. G. Tisch, and H. Crespo: 'Single-shot implementation of dispersion-scan for the characterization of ultrashort laser pulses'. *Opt. Express* (2015), vol. 23(25): pp. 32803–32808. DOI: 10.1364/OE.23.032803 (cit. on p. 51).

[Fac05] Faccio, D., A. Matijosius, A. Dubietis, R. Piskarskas, A. Varanavičius, E. Gaizauskas, A. Piskarskas, A. Couairon, and P. Di Trapani: 'Near- and far-field evolution of laser pulse filaments in Kerr media'. *Phys. Rev. E* (2005), vol. 72(3): p. 037601. DOI: 10.1103/PhysRevE.72.037601 (cit. on p. 3).

[Fac06] Faccio, D., M. A. Porras, A. Dubietis, F. Bragheri, A. Couairon, and P. Di Trapani: 'Conical Emission, Pulse Splitting, and X-Wave Parametric Amplification in Nonlinear Dynamics of Ultrashort Light Pulses'. *Phys. Rev. Lett.* (2006), vol. 96(19): p. 193901. DOI: 10.1103/PhysRevLett.96.193901 (cit. on p. 11).

[Fac08] Faccio, D., A. Averchi, A. Lotti, P. Di Trapani, A. Couairon, D. Papazoglou, and S. Tzortzakis: 'Ultrashort laser pulse filamentation from spontaneous X Wave formation in air'. *Opt. Express* (2008), vol. 16(3): pp. 1565–1570. DOI: 10.1364/OE.16.001565 (cit. on p. 122).

[Fau18] Faure, J., D. Gustas, D. Guénot, A. Vernier, F. Böhle, M. Ouillé, S. Haessler, R. Lopez-Martens, and A. Lifschitz: 'A review of recent progress on laser-plasma acceleration at kHz repetition rate'. *Plasma Phys. Control. Fusion* (2018), vol. 61(1): p. 014012. DOI: 10.1088/1361-6587/aae047 (cit. on p. 2).

[Fay01] Faye, G., J. Kasparian, and R. Sauerbrey: 'Modifications to the lidar equation due to nonlinear propagation in air'. *Appl. Phys. B* (2001), vol. 73(2): pp. 157–163. DOI: 10.1007/s003400100621 (cit. on p. 69).

[Fen01] Feng, S. and H. G. Winful: 'Physical origin of the Gouy phase shift'. *Opt. Lett.* (2001), vol. 26(8): pp. 485–487. doi: 10.1364/OL.26.000485 (cit. on p. 37).

[Fib04] Fibich, G., S. Eisenmann, B. Ilan, and A. Zigler: 'Control of multiple filamentation in air'. *Opt. Lett.* (2004), vol. 29(15): pp. 1772–1774. doi: 10.1364/OL.29.001772 (cit. on p. 12).

[Fli10] Fliessbach, T.: *Statistische Physik*. Fifth Edition. Springer Spektrum, Heidelberg, 2010. doi: 10.1007/978-3-8274-2528-7 (cit. on p. 23).

[Fon99a] La Fontaine, B., F. Vidal, Z. Jiang, C. Y. Chien, D. Comtois, A. Desparois, T. W. Johnston, J.-C. Kieffer, H. Pépin, and H. P. Mercure: 'Filamentation of ultrashort pulse laser beams resulting from their propagation over long distances in air'. *Phys. Plasmas* (1999), vol. 6(5): pp. 1615–1621. doi: 10.1063/1.873715 (cit. on pp. 3, 8, 9, 87).

[Fou10] Fourcade Dutin, C., A. Dubrouil, S. Petit, E. Mével, E. Constant, and D. Descamps: 'Post-compression of high-energy femtosecond pulses using gas ionization'. *Opt. Lett.* (2010), vol. 35(2): pp. 253–255. doi: 10.1364/OL.35.000253 (cit. on p. 2).

[Fri11] Fridman, A. F. and L. A. Kennedy: *Plasma Physics and Engineering*. Second. Taylor & Francis, New York, 2011. doi: 10.1201/b11728 (cit. on pp. 26, 27, 75).

[Gaa09] Gaarde, M. B. and A. Couairon: 'Intensity Spikes in Laser Filamentation: Diagnostics and Application'. *Phys. Rev. Lett.* (2009), vol. 103(4): p. 043901. doi: 10.1103/PhysRevLett.103.043901 (cit. on pp. 35, 36, 121).

[Gal14] Gallet, V.: 'Dispositifs expérimentaux pur la caractérisation spatio-temporelle de chaînes laser femtosecondes haute-puissance'. PhD thesis. Université Paris XI, 2014 (cit. on pp. 5, 43).

[Gal99] Gallmann, L., D. H. Sutter, N. Matuschek, G. Steinmeyer, U. Keller, C. Iaconis, and I. A. Walmsley: 'Characterization of sub-6-fs optical pulses with spectral phase interferometry for direct electric-field reconstruction'. *Opt. Lett.* (1999), vol. 24(18): pp. 1314–1316. doi: 10.1364/OL.24.001314 (cit. on p. 50).

[Gam02] Gamaly, E. G., A. V. Rode, B. Luther-Davies, and V. T. Tikhonchuk: 'Ablation of solids by femtosecond lasers: Ablation mechanism and ablation thresholds for metals and dielectrics'. *Phys. Plasmas* (2002), vol. 9(3): pp. 949–957. doi: 10.1063/1.1447555 (cit. on pp. 1, 33).

[Gia10] De Giacomo, A., R. Gaudiuso, M. Dell'Aglio, and A. Santagata: 'The role of continuum radiation in laser induced plasma spectroscopy'. *Spectrochim. Acta B* (2010), vol. 65(5): pp. 385–394. doi: 10.1016/j.sab.2010.03.016 (cit. on p. 26).

[Gia14] De Giacomo, A., M. Dell'Aglio, O. De Pascale, R. Gaudiuso, V. Palleschi, C. Parigger, and A. Woods: 'Plasma processes and emission spectra in laser induced plasmas: A point of view'. *Spectrochim. Acta B* (2014), vol. 100: pp. 180–188. doi: 10.1016/j.sab.2014.08.013 (cit. on p. 74).

[Gia17] De Giacomo, A. and J. Hermann: 'Laser-induced plasma emission: from atomic to molecular spectra'. *J. Phys. D: Appl. Phys.* (2017), vol. 50(18): p. 183002. doi: 10.1088/1361-6463/aa6585 (cit. on pp. 19, 22, 23, 26–28, 84, 85).

[Gio67] Giordmaine, J. A., P. M. Rentzepis, S. L. Shapiro, and K. W. Wecht: 'Two-photon excitation of fluorescence by picosecond light pulses'. *Appl. Phys. Lett.* (1967), vol. 11(7): pp. 216–218. doi: 10.1063/1.1755105 (cit. on p. 50).

[Gol90] Golub, I.: 'Optical characteristics of supercontinuum generation'. *Opt. Lett.* (1990), vol. 15(6): pp. 305–307. doi: 10.1364/OL.15.000305 (cit. on p. 11).

[Gry17] Grynko, R. I., D. L. Weerawarne, and B. Shim: 'Effects of higher-order nonlinear processes on harmonic-generation phase matching'. *Phys. Rev. A* (2017), vol. 96(1): p. 013816. doi: 10.1103/PhysRevA.96.013816 (cit. on pp. 38, 59).

[Har08] Hartinger, K. and R. A. Bartels: 'Enhancement of third harmonic generation by a laser-induced plasma'. *Appl. Phys. Lett.* (2008), vol. 93(15): p. 151102. doi: 10.1063/1.2993222 (cit. on p. 2).

[Hau04] Hauri, C. P., W. Kornelis, F. W. Helbing, A. Heinrich, A. Couairon, A. Mysyrowicz, J. Biegert, and U. Keller: 'Generation of intense, carrier-envelope phase-locked few-cycle laser pulses through filamentation'. *Appl. Phys. B* (2004), vol. 79(6): pp. 673–677. doi: 10.1007/s00340-004-1650-z (cit. on pp. 34, 35).

[Hee79] Heer, F. J. de, R. H. J. Jansen, and W. van der Kaay: 'Total cross sections for electron scattering by Ne, Ar, Kr and Xe'. *J. Phys. B: At. Mol. Opt. Phys* (1979), vol. 12(6): pp. 979–1002. doi: 10.1088/0022-3700/12/6/016 (cit. on p. 75).

[Hen00] Hentschel, M., Z. Cheng, F. Krausz, and Ch. Spielmann: 'Generation of 0.1-TW optical pulses with a single-stage Ti:sapphire amplifier at a 1-kHz repetition rate'. *Appl. Phys. B* (2000), vol. 70(1): S161–S164. doi: 10.1007/s003400000327 (cit. on p. 1).

[Hen01] Hentschel, M., R. Kienberger, Ch. Spielmann, G. A. Reider, N. Milosevic, T. Brabec, P. Corkum, U. Heinzmann, M. Drescher, and F. Krausz: 'Attosecond metrology'. *Nature* (2001), vol. 414(6863): pp. 509–513. doi: 10.1038/35107000 (cit. on p. 1).

[Her09] Herrmann, D., L. Veisz, R. Tautz, F. Tavella, K. Schmid, V. Pervak, and F. Krausz: 'Generation of sub-three-cycle, 16 TW light pulses by using noncollinear optical parametric chirped-pulse amplification'. *Opt. Lett.* (2009), vol. 34(16): pp. 2459–2461. doi: 10.1364/OL.34.002459 (cit. on p. 1).

[Hey16] Heyl, C. M., H. Coudert-Alteirac, M. Miranda, M. Louisy, K. Kovacs, V. Tosa, E. Balogh, K. Varjú, A. L'Huillier, A. Couairon, and C. L. Arnold: 'Scale-invariant nonlinear optics in gases'. *Optica* (2016), vol. 3(1): pp. 75–81. doi: 10.1364/OPTICA.3.000075 (cit. on pp. 13, 120).

[Hof14] Hoffmann, M., T. Nagy, T. Willemsen, M. Jupé, D. Ristau, and U. Morgner: 'Pulse characterization by THG d-scan in absorbing nonlinear media'. *Opt. Express* (2014), vol. 22(5): pp. 5234–5240. doi: 10.1364/OE.22.005234 (cit. on p. 51).

[Iac98] Iaconis, C. and I. A. Walmsley: 'Spectral phase interferometry for direct electric-field reconstruction of ultrashort optical pulses'. *Opt. Lett.* (1998), vol. 23(10): pp. 792–794. doi: 10.1364/OL.23.000792 (cit. on p. 50).

[Ion15] Ionin, A. A., L. V. Seleznev, and E. S. Sunchugasheva: 'Formation of plasma channels in air under filamentation of focused ultrashort laser pulses'. *Laser Phys.* (2015), vol. 25(3): p. 033001. doi: 10.1088/1054-660x/25/3/033001 (cit. on p. 19).

[Jar14] Jarnac, A., M. Durand, Y. Liu, B. Prade, A. Houard, V. Tikhonchuk, and A. Mysyrowicz: 'Study of laser induced plasma grating dynamics in gases'. *Opt. Commun.* (2014), vol. 312: pp. 35–42. doi: 10.1016/j.optcom.2013.07.082 (cit. on pp. 22, 26, 28, 30, 60).

[Jol20] Jolly, S. W., O. Gobert, and F. Quéré: 'Spatio-temporal characterization of ultrashort laser beams: a tutorial'. *J. Opt.* (2020), vol. 22(10): p. 103501. doi: 10.1088/2040-8986/abad08 (cit. on pp. 41, 43, 46, 47).

[Jür19] Jürgens, P., Vrakking M. J. J., A. Husakou, R. Stoian, and A. Mermillod-Blondin: 'Plasma formation and relaxation dynamics in fused silica driven by femtosecond short-wavelength infrared laser pulses'. *Appl. Phys. Lett.* (2019), vol. 115(19): p. 191903. doi: 10.1063/1.5117837 (cit. on p. 84).

[Jus19] Jusko, C., A. Sridhar, E. Appi, L. Shi, U. Morgner, and M. Kovacev: 'Filamentation-assisted plasma lifetime measurements in atomic and molecular gases via third-harmonic enhancement'. *J. Opt. Soc. Am. B* (2019), vol. 36(12): pp. 3505–3513. doi: 10.1364/JOSAB.36.003505 (cit. on pp. 37, 57, 59–61, 70–72).

[Jus20] Jusko, C., A. Sridhar, E. Appi, L. Shi, U. Morgner, and M. Kovacev: 'Femtosecond laser-induced plasma evolution studies via third-harmonic enhancement in atomic and molecular gases'. *OSA High-brightness Sources and Light-driven Interactions Congress 2020 (EUVXRAY, HILAS, MICS)*. 2020: JW1A.15. doi: 10.1364/EUVXRAY.2020.JW1A.15 (cit. on p. 78).

[Kan03] Kandidov, V. P., O. G. Kosareva, I. S. Golubtsov, W. Liu, A. Becker, N. Akozbek, C. M. Bowden, and S. L. Chin: 'Self-transformation of a powerful femtosecond laser pulse into a white-light laser pulse in bulk optical media (or supercontinuum generation)'. *Appl. Phys. B* (2003), vol. 77(2): pp. 149–165. doi: 10.1007/s00340-003-1214-7 (cit. on pp. 20, 22).

[Kan93a] Kane, D. J. and R. Trebino: 'Characterization of arbitrary femtosecond pulses using frequency-resolved optical gating'. *IEEE J. Quantum Electron.* (1993), vol. 29(2): pp. 571–579. doi: 10.1109/3.199311 (cit. on pp. 50, 51).

[Kan93b] Kane, D. J. and R. Trebino: 'Single-shot measurement of the intensity and phase of an arbitrary ultrashort pulse by using frequency-resolved optical gating'. *Opt. Lett.* (1993), vol. 18(10): pp. 823–825. doi: 10.1364/OL.18.000823 (cit. on pp. 50, 51).

[Kap91] Kapteyn, H. C., M. M. Murnane, A. Szoke, and R. W. Falcone: 'Prepulse energy suppression for high-energy ultrashort pulses using self-induced plasma shuttering'. *Opt. Lett.* (1991), vol. 16(7): pp. 490–492. doi: 10.1364/OL.16.000490 (cit. on p. 2).

[Kar15] Kartashov, D., S. Ališauskas, A. Pugžlys, M. N. Shneider, and A. Baltuška: 'Theory of a filament initiated nitrogen laser'. *J. Phys. B: At. Mol. Opt. Phys* (2015), vol. 48(9): p. 094016. doi: 10.1088/0953-4075/48/9/094016 (cit. on pp. 22, 26, 75).

[Kas00] Kasparian, J., R. Sauerbrey, and S. L. Chin: 'The critical laser intensity of self-guided light filaments in air'. *Appl. Phys. B* (2000), vol. 71(6): pp. 877–879. doi: 10.1007/s003400000463 (cit. on pp. 3, 9, 69).

[Kas03] Kasparian, J., M. Rodriguez, G. Méjean, J. Yu, E. Salmon, H. Wille, R. Bourayou, S. Frey, Y.-B. André, A. Mysyrowicz, R. Sauerbrey, J.-P. Wolf, and L. Wöste: 'White-Light Filaments for Atmospheric Analysis'. *Science* (2003), vol. 301(5629): pp. 61–64. doi: 10.1126/science.1085020 (cit. on p. 3).

[Kas08] Kasparian, J., R. Ackermann, Y.-B. André, G. Méchain, G. Méjean, B. Prade, P. Rohwetter, E. Salmon, K. Stelmaszczyk, J. Yu, A. Mysyrowicz, R. Sauerbrey, L. Wöste, and J.-P. Wolf: 'Electric events synchronized with laser filaments in thunderclouds'. *Opt. Express* (2008), vol. 16(8): pp. 5757–5763. doi: 10.1364/OE.16.005757 (cit. on p. 3).

[Kat09] Katzir, Y., S. Eisenmann, Y. Ferber, A. Zigler, and R. F. Hubbard: 'A plasma microlens for ultrashort high power lasers'. *Appl. Phys. Lett.* (2009), vol. 95(3): p. 031101. doi: 10.1063/1.3184788 (cit. on p. 2).

[Kel65] Keldysh, L. V.: 'Ionization in the field of a strong electromagnetic wave'. *Sov. Phys. JETP* (1965), vol. 20(5): pp. 1307–1314 (cit. on p. 24).

[Kol02] Kolesik, M., J. V. Moloney, and M. Mlejnek: 'Unidirectional Optical Pulse Propagation Equation'. *Phys. Rev. Lett.* (2002), vol. 89(28): p. 283902. doi: 10.1103/PhysRevLett.89.283902 (cit. on p. 99).

[Kos97] Kosareva, O. G., V. P. Kandidov, A. Brodeur, C. Y. Chien, and S. L. Chin: 'Conical emission from laser–plasma interactions in the filamentation of powerful ultrashort laser pulses in air'. *Opt. Lett.* (1997),

vol. 22(17): pp. 1332–1334. DOI: 10.1364/OL.22.001332 (cit. on pp. 11, 87).

[Kou20] KOULOUKLIDIS, A. D., C. GOLLNER, V. SHUMAKOVA, V. YU. FEDOROV, A. PUGŽLYS, A. BALTUŠKA, and S. TZORTZAKIS: 'Observation of extremely efficient terahertz generation from mid-infrared two-color laser filaments'. *Nat. Commun.* (2020), vol. 11(1): p. 292. DOI: 10.1038/s41467-019-14206-x (cit. on p. 121).

[Kra09] KRAUSZ, F. and M. IVANOV: 'Attosecond physics'. *Rev. Mod. Phys.* (2009), vol. 81(1): pp. 163–234. DOI: 10.1103/RevModPhys.81.163 (cit. on p. 1).

[Kre14] KRETSCHMAR, M., C. BRÉE, T. NAGY, A. DEMIRCAN, H. G. KURZ, U. MORGNER, and M. KOVAČEV: 'Direct observation of pulse dynamics and self-compression along a femtosecond filament'. *Opt. Express* (2014), vol. 22(19): pp. 22905–22916. DOI: 10.1364/OE.22.022905 (cit. on pp. 34, 35, 87).

[Kre16] KRETSCHMAR, M.: 'Extreme Nonlinear Dynamics in the Filamentation Regime'. PhD thesis. Leibniz Universität Hannover, 2016. DOI: 10.15488/8721 (cit. on pp. 25, 32, 35).

[Kre93] KREYE, W. C., J. W. HEMSKY, and M. L. ANDREWS: 'A simple numerical method for a modified Abel inversion in which the density can be approximated by elliptical symmetry'. *J. Phys. D: Appl. Phys* (1993), vol. 26(11): pp. 1836–1842. DOI: 10.1088/0022-3727/26/11/003 (cit. on p. 29).

[Kum03] KUMAGAI, H., S.-H. CHO, K. ISHIKAWA, K. MIDORIKAWA, M. FUJIMOTO, S.-I. AOSHIMA, and Y. TSUCHIYA: 'Observation of the complex propagation of a femtosecond laser pulse in a dispersive transparent bulk material'. *J. Opt. Soc. Am. B* (2003), vol. 20(3): pp. 597–602. DOI: 10.1364/JOSAB.20.000597 (cit. on p. 87).

[Kur13] Kurz, H. G.: 'High-Order Harmonic Spectroscopy with Water Droplets'. PhD thesis. Leibniz Universität Hannover, 2013. DOI: 10.15488/8309 (cit. on p. 24).

[Lan98] Lange, H. R., A. Chiron, J.-F. Ripoche, A. Mysyrowicz, P. Breger, and P. Agostini: 'High-Order Harmonic Generation and Quasiphase Matching in Xenon Using Self-Guided Femtosecond Pulses'. *Phys. Rev. Lett.* (1998), vol. 81(8): pp. 1611–1613. DOI: 10.1103/PhysRevLett.81.1611 (cit. on p. 35).

[Lea10] Leahy-Hoppa, M. R., J. Miragliotta, R. Osiander, J. Burnett, Y. Dikmelik, C. McEnnis, and J. B. Spicer: 'Ultrafast Laser-Based Spectroscopy and Sensing: Applications in LIBS, CARS, and THz Spectroscopy'. *Sensors* (2010), vol. 10(5): pp. 4342–4372. DOI: 10.3390/s100504342 (cit. on p. 1).

[Leb17] Leblanc, A., A. Denoeud, L. Chopineau, G. Mennerat, Ph. Martin, and F. Quéré: 'Plasma holograms for ultrahigh-intensity optics'. *Nat. Phys.* (2017), vol. 13(5): pp. 440–443. DOI: 10.1038/nphys4007 (cit. on p. 2).

[Lee09] Lee, J.-H., Y. S. Lee, J. Park, J. J. Park, D. S. Kim, T. J. Yu, and C. H. Nam: 'Implementation of the direct locking method for long-term carrier-envelope-phase stabilization of a grating-based kHz femtosecond laser'. *Appl. Phys. B* (2009), vol. 96(2): pp. 287–291. DOI: 10.1007/s00340-009-3489-9 (cit. on p. 35).

[LHu91] L'Huillier, A., K. J. Schafer, and K. C. Kulander: 'Theoretical aspects of intense field harmonic generation'. *J. Phys. B: At. Mol. Opt. Phys* (1991), vol. 24(15): pp. 3315–3341. DOI: 10.1088/0953-4075/24/15/004 (cit. on p. 21).

[Lis04] Lister, G. G., J. E. Lawler, W. P. Lapatovich, and V. A. Godyak: 'The physics of discharge lamps'. *Rev. Mod. Phys.* (2004), vol. 76(2): pp. 541–598. DOI: 10.1103/RevModPhys.76.541 (cit. on p. 19).

[Liu03] Liu, W., S. L Chin, O. Kosareva, I. S. Golubtsov, and V. P. Kandidov: 'Multiple refocusing of a femtosecond laser pulse in a dispersive liquid (methanol)'. *Opt. Commun.* (2003), vol. 225(1): pp. 193–209. doi: 10.1016/j.optcom.2003.07.024 (cit. on p. 8).

[Liu05a] Liu, W., F. Théberge, E. Arévalo, J.-F. Gravel, A. Becker, and S. L. Chin: 'Experiment and simulations on the energy reservoir effect in femtosecond light filaments'. *Opt. Lett.* (2005), vol. 30(19): pp. 2602–2604. doi: 10.1364/OL.30.002602 (cit. on pp. 10, 32).

[Liu05b] Liu, W., J.-F. Gravel, F. Théberge, A. Becker, and S. L. Chin: 'Background reservoir: its crucial role for long-distance propagation of femtosecond laser pulses in air'. *Appl. Phys. B* (2005), vol. 80(7): pp. 857–860. doi: 10.1007/s00340-005-1805-6 (cit. on p. 10).

[Liu07] Liu, W. and S. L. Chin: 'Abnormal wavelength dependence of the self-cleaning phenomenon during femtosecond-laser-pulse filamentation'. *Phys. Rev. A* (2007), vol. 76(1): p. 013826. doi: 10.1103/PhysRevA.76.013826 (cit. on p. 12).

[Liu10] Liu, Y., M. Durand, S. Chen, A. Houard, B. Prade, B. Forestier, and A. Mysyrowicz: 'Energy Exchange between Femtosecond Laser Filaments in Air'. *Phys. Rev. Lett.* (2010), vol. 105(5): p. 055003. doi: 10.1103/PhysRevLett.105.055003 (cit. on p. 2).

[Liu11] Liu, Y., M. Durand, A. Houard, B. Forestier, A. Couairon, and A. Mysyrowicz: 'Efficient generation of third harmonic radiation in air filaments: A revisit'. *Opt. Commun.* (2011), vol. 284(19): pp. 4706–4713. doi: 10.1016/j.optcom.2011.05.050 (cit. on pp. 3, 37–39, 59).

[Liu15] Liu, X.-L., X. Lu, Z.-G. Du, J.-L. Ma, Y.-T. Li, and J. Zhang: 'Enhancement of third harmonic generation in air filamentation using obstacles'. *Chin. Phys. B* (2015), vol. 24(3): p. 034207. doi: 10.1088/1674-1056/24/3/034207 (cit. on p. 4).

[Liu19] Liu, Y., C. Kou, A. Houard, and A. Mysyrowicz: 'Optimizing the third harmonic generated from air plasma filaments pumped by femtosecond laser pulses'. *J. Opt. Soc. Am. B* (Oct. 2019), vol. 36(10): G13–G18. doi: 10.1364/JOSAB.36.000G13 (cit. on pp. 3, 38, 39).

[Lor13] Loriot, V., G. Gitzinger, and N. Forget: 'Self-referenced characterization of femtosecond laser pulses by chirp scan'. *Opt. Express* (2013), vol. 21(21): pp. 24879–24893. doi: 10.1364/OE.21.024879 (cit. on p. 50).

[Lou17] Louisy, M., C. Guo, L. Neoričić, S. Zhong, A. L'Huillier, C. L. Arnold, and M. Miranda: 'Compact single-shot d-scan setup for the characterization of few-cycle laser pulses'. *Appl. Opt.* (2017), vol. 56(32): pp. 9084–9089. doi: 10.1364/AO.56.009084 (cit. on p. 51).

[Loz04] Lozovoy, V. V., I. Pastirk, and M. Dantus: 'Multiphoton intrapulse interference. IV. Ultrashort laser pulse spectral phase characterization and compensation'. *Opt. Lett.* (2004), vol. 29(7): pp. 775–777. doi: 10.1364/OL.29.000775 (cit. on p. 50).

[Lu14] Lu, C.-H., Y.-J. Tsou, H.-Y. Chen, B.-H. Chen, Y.-C. Cheng, S.-D. Yang, M.-C. Chen, C.-C. Hsu, and A. H. Kung: 'Generation of intense supercontinuum in condensed media'. *Optica* (2014), vol. 1(6): pp. 400–406. doi: 10.1364/OPTICA.1.000400 (cit. on p. 3).

[Lug68] Lugovoi, V. N. and A. M. Prokhorov: 'Possible explanation of small-scale filaments of self-focusing filaments'. *JETP Lett.* (1968), vol. 7: pp. 117–119 (cit. on p. 30).

[Lut94] Luther, G. G., A. C. Newell, J. V. Moloney, and E. M. Wright: 'Short-pulse conical emission and spectral broadening in normally dispersive media'. *Opt. Lett.* (1994), vol. 19(11): pp. 789–791. doi: 10.1364/OL.19.000789 (cit. on p. 11).

[Ma08] Ma, S., H. Gao, and L. Wu: 'Modified Fourier-Hankel method based on analysis of errors in Abel inversion using Fourier transform techniques'. *Appl. Opt.* (2008), vol. 47(9): pp. 1350–1357. doi: 10.1364/AO.47.001350 (cit. on p. 29).

[Mah15] Mahieu, B., D. Gauthier, G. De Ninno, H. Dacasa, M. Lozano, J.-P. Rousseau, P. Zeitoun, D. Garzella, and H. Merdji: 'Spectral-phase interferometry for direct electric-field reconstruction applied to seeded extreme-ultraviolet free-electron lasers'. *Opt. Express* (2015), vol. 23(14): pp. 17665–17674. doi: 10.1364/OE.23.017665 (cit. on p. 50).

[Mah83] Mahajan, V. N.: 'Strehl ratio for primary aberrations in terms of their aberration variance'. *J. Opt. Soc. Am.* (1983), vol. 73(6): pp. 860–861. doi: 10.1364/JOSA.73.000860 (cit. on p. 109).

[Mai05] Mairesse, Y., O. Gobert, P. Breger, H. Merdji, P. Meynadier, P. Monchicourt, M. Perdrix, P. Salières, and B. Carré: 'High Harmonic XUV Spectral Phase Interferometry for Direct Electric-Field Reconstruction'. *Phys. Rev. Lett.* (2005), vol. 94(17): p. 173903. doi: 10.1103/PhysRevLett.94.173903 (cit. on p. 50).

[Mai66] Maier, M., W. Kaiser, and J. A. Giordmaine: 'Intense Light Bursts in the Stimulated Raman Effect'. *Phys. Rev. Lett.* (1966), vol. 17(26): pp. 1275–1277. doi: 10.1103/PhysRevLett.17.1275 (cit. on p. 50).

[Mai88] Maine, P., D. Strickland, P. Bado, M. Pessot, and G. Mourou: 'Generation of ultrahigh peak power pulses by chirped pulse amplification'. *IEEE J. Quantum Electron.* (1988), vol. 24(2): pp. 398–403. doi: 10.1109/3.137 (cit. on p. 1).

[Maj11] Majus, D., V. Jukna, G. Valiulis, D. Faccio, and A. Dubietis: 'Spatiotemporal rogue events in femtosecond filamentation'. *Phys. Rev. A* (2011), vol. 83(2): p. 025802. doi: 10.1103/PhysRevA.83.025802 (cit. on p. 122).

[Mal09] Malone, C. P., P. V. Johnson, J. A. Young, X. Liu, B. Ajdari, M. A. Khakoo, and I. Kanik: 'Integral cross sections for electron-impact excitation of the $C^3\Pi_u$, $E^3\Sigma_g^+$ and a" $^1\Sigma_g^+$ states of N_2'. *J. Phys. B: At. Mol. Opt. Phys.* (2009), vol. 42: p. 225202. doi: 10.1088/0953-4075/42/22/225202 (cit. on p. 75).

[Mar68] Marburger, J. H. and E. Dawes: 'Dynamical Formation of a Small-Scale Filament'. *Phys. Rev. Lett.* (1968), vol. 21(8): pp. 556–558. doi: 10.1103/PhysRevLett.21.556 (cit. on p. 17).

[Mar75] Marburger, J. H.: 'Self-focusing: Theory'. *Prog. Quantum Electron.* (1975), vol. 4: pp. 35–110. doi: 10.1016/0079-6727(75)90003-8 (cit. on p. 17).

[Mat04] Matijošius, A., J. Trull, P. Di Trapani, A. Dubietis, R. Piskarskas, A. Varanavičius, and A. Piskarskas: 'Nonlinear space–time dynamics of ultrashort wave packets in water'. *Opt. Lett.* (2004), vol. 29(10): pp. 1123–1125. doi: 10.1364/OL.29.001123 (cit. on p. 87).

[Mat18] Matthews, M., F. Morales, A. Patas, A. Lindinger, J. Gateau, N. Berti, S. Hermelin, J. Kasparian, M. Richter, T. Bredtmann, O. Smirnova, J.-P. Wolf, and M. Ivanov: 'Amplification of intense light fields by nearly free electrons'. *Nat. Phys.* (2018), vol. 14(7): pp. 695–700. doi: 10.1038/s41567-018-0105-0 (cit. on p. 8).

[Méc04] Méchain, G., A. Couairon, Y.-B. André, C. D'Amico, M. Franco, B. Prade, S. Tzortzakis, A. Mysyrowicz, and R. Sauerbrey: 'Long-range self-channeling of infrared laser pulses in air: a new propagation regime without ionization'. *Appl. Phys. B* (2004), vol. 79(3): pp. 379–382. doi: 10.1007/s00340-004-1557-8 (cit. on pp. 9, 12).

[Mic14] Michel, P., L. Divol, D. Turnbull, and J. D. Moody: 'Dynamic Control of the Polarization of Intense Laser Beams via Optical Wave Mixing in Plasmas'. *Phys. Rev. Lett.* (2014), vol. 113(20): p. 205001. doi: 10.1103/PhysRevLett.113.205001 (cit. on p. 2).

[Mir12a] Miranda, M., T. Fordell, C. Arnold, A. L'Huillier, and H. Crespo: 'Simultaneous compression and characterization of ultrashort laser pulses using chirped mirrors and glass wedges'. *Opt. Express* (2012), vol. 20(1): pp. 688–697. doi: 10.1364/OE.20.000688 (cit. on pp. 5, 50, 51).

[Mir12b] Miranda, M., C. L. Arnold, T. Fordell, F. Silva, B. Alonso, R. Weigand, A. L'Huillier, and H. Crespo: 'Characterization of broadband few-cycle laser pulses with the d-scan technique'. *Opt. Express* (2012), vol. 20(17): pp. 18732–18743. doi: 10.1364/OE.20.018732 (cit. on pp. 5, 50, 51).

[Mir14] Miranda, M., M. Kotur, P. Rudawski, C. Guo, A. Harth, A. L'Huillier, and C. L. Arnold: 'Spatiotemporal characterization of ultrashort laser pulses using spatially resolved Fourier transform spectrometry'. *Opt. Lett.* (2014), vol. 39(17): pp. 5142–5145. doi: 10.1364/OL.39.005142 (cit. on pp. 5, 43–45).

[Mle98] Mlejnek, M., E. M. Wright, and J. V. Moloney: 'Dynamic spatial replenishment of femtosecond pulses propagating in air'. *Opt. Lett.* (1998), vol. 23(5): pp. 382–384. doi: 10.1364/OL.23.000382 (cit. on p. 32).

[Mle99] Mlejnek, M., E. M. Wright, and J. V. Moloney: 'Moving-focus versus self-waveguiding model for long-distance propagation of femtosecond pulses in air'. *IEEE J. Quantum Electron.* (1999), vol. 35(12): pp. 1771–1776. doi: 10.1109/3.806580 (cit. on p. 32).

[Mul10] Mulser, P. and D. Bauer: *High Power Laser-Matter Interaction*. Springer-Verlag, Berlin/Heidelberg, 2010. doi: 10.1007/978-3-540-46065-7 (cit. on p. 24).

[Nai16] Naidoo, D., F. S. Roux, A. Dudley, I. Litvin, B. Piccirillo, L. Marrucci, and A. Forbes: 'Controlled generation of higher-order Poincaré sphere beams from a laser'. *Nat. Photonics* (2016), vol. 10(5): pp. 327–332. doi: 10.1038/nphoton.2016.37 (cit. on p. 120).

[Neo22] Neoričić, L., C. Jusko, S. Mikaelsson, C. Guo, M. Miranda, S. Zhong, F. Garmirian, B. Major, J. M. Brown, M. B. Gaarde, A. Couairon, U. Morgner, M. Kovačev, and C. L. Arnold: '4D spatio-temporal electric field characterization of ultrashort light pulses undergoing filamentation'. *Opt. Express* (2022), vol. 30(15): pp. 27938–

27950. DOI: 10.1364/OE.461388 (cit. on pp. 52, 88–90, 101, 102, 104, 106–108, 110).

[Nib96] NIBBERING, E. T. J., P. F. CURLEY, G. GRILLON, B. S. PRADE, M. A. FRANCO, F. SALIN, and A. MYSYROWICZ: 'Conical emission from self-guided femtosecond pulses in air'. *Opt. Lett.* (1996), vol. 21(1): pp. 62–64. DOI: 10.1364/OL.21.000062 (cit. on pp. 11, 32).

[Nie18] NIE, Z., C.-H. PAI, J. HUA, C. ZHANG, Y. WU, Y. WAN, F. LI, J. ZHANG, Z. CHENG, Q. SU, S. LIU, Y. MA, X. NING, Y. HE, W. LU, H.-H. CHU, J. WANG, W. B. MORI, and C. JOSHI: 'Relativistic single-cycle tunable infrared pulses generated from a tailored plasma density structure'. *Nat. Photonics* (2018), vol. 12(8): pp. 489–494. DOI: 10.1038/s41566-018-0190-8 (cit. on p. 2).

[Nis96] NISOLI, M., S. DE SILVESTRI, and O. SVELTO: 'Generation of high energy 10 fs pulses by a new pulse compression technique'. *Appl. Phys. Lett.* (1996), vol. 68(20): pp. 2793–2795. DOI: 10.1063/1.116609 (cit. on p. 3).

[O'S01] O'SHEA, P., M. KIMMEL, X. GU, and R. TREBINO: 'Highly simplified device for ultrashort-pulse measurement'. *Opt. Lett.* (2001), vol. 26(12): pp. 932–934. DOI: 10.1364/OL.26.000932 (cit. on p. 50).

[Oks10] OKSENHENDLER, T., S. COUDREAU, N. FORGET, V. CROZATIER, S. GRABIELLE, R. HERZOG, O. GOBERT, and D. KAPLAN: 'Self-referenced spectral interferometry'. *Appl. Phys. B* (2010), vol. 99(1): pp. 7–12. DOI: 10.1007/s00340-010-3916-y (cit. on p. 50).

[Pap01] PAPADOGIANNIS, N. A., C. KALPOUZOS, E. GOULIELMAKIS, G. NERSISYAN, D. CHARALAMBIDIS, F. AUGÉ, F. WEIHE, and PH. BALCOU: 'Kilohertz extreme-ultraviolet light source based on femtosecond high-order harmonic generation from noble gases'. *Appl. Phys. B* (2001), vol. 73(7): pp. 687–692. DOI: 10.1007/s003400100734 (cit. on p. 3).

[Par16] Pariente, G., V. Gallet, A. Borot, O. Gobert, and F. Quéré: 'Space-time characterization of ultra-intense femtosecond laser beams'. *Nat. Photonics* (2016), vol. 10(8): pp. 547–553. doi: 10.1038/nphoton.2016.140 (cit. on p. 43).

[Per66] Perelomov, A. M., V. S. Popov, and M. V. Terent'ev: 'Ionization of Atoms in an Alternating Electric Field'. *Sov. Phys. JETP* (1966), vol. 23: p. 924 (cit. on pp. 25, 99).

[Pfe06] Pfeifer, T., Ch. Spielmann, and G. Gerber: 'Femtosecond x-ray science'. *Rep. Prog. Phys.* (2006), vol. 69(2): pp. 443–505. doi: 10.1088/0034-4885/69/2/r04 (cit. on p. 21).

[Phi05] Philip, J., C. D'Amico, G. Chériaux, A. Couairon, B. Prade, and A. Mysyrowicz: 'Amplification of Femtosecond Laser Filaments in Ti:Sapphire'. *Phys. Rev. Lett.* (2005), vol. 95(16): p. 163901. doi: 10.1103/PhysRevLett.95.163901 (cit. on p. 10).

[Pre10] Prem Kiran, P., S. Bagchi, C. L. Arnold, S. R. Krishnan, G. Ravindra Kumar, and A. Couairon: 'Filamentation without intensity clamping'. *Opt. Express* (2010), vol. 18(20): pp. 21504–21510. doi: 10.1364/OE.18.021504 (cit. on p. 36).

[Pro21] Produit, T., P. Walch, C. Herkommer, A. Mostajabi, M. Moret, U. Andral, A. Sunjerga, M. Azadifar, Y.-B. André, B. Mahieu, W. Haas, B. Esmiller, G. Fournier, P. Krötz, T. Metzger, K. Michel, A. Mysyrowicz, M. Rubinstein, F. Rachidi, J. Kasparian, J.-P. Wolf, and A. Houard: 'The laser lightning rod project'. *Eur. Phys. J. Appl. Phys.* (2021), vol. 93(1): p. 10504. doi: 10.1051/epjap/2020200243 (cit. on p. 121).

[Pus19] Pushkarev, D., E. Mitina, D. Shipilo, N. Panov, D. Uryupina, A. Ushakov, R. Volkov, A. Karabutov, I. Babushkin, A. Demircan, U. Morgner, O. Kosareva, and A. Savel'ev: 'Transverse structure and energy deposition by a subTW femtosecond laser in air: from single

filament to superfilament'. *New J. Phys.* (2019), vol. 21(3): p. 033027. DOI: 10.1088/1367-2630/ab043f (cit. on p. 87).

[Rad07] Radunsky, Aleksander S., Ian A. Walmsley, Simon-Pierre Gorza, and Piotr Wasylczyk: 'Compact spectral shearing interferometer for ultrashort pulse characterization'. *Opt. Lett.* (2007), vol. 32(2): pp. 181–183. DOI: 10.1364/OL.32.000181 (cit. on p. 50).

[Rai00] Rairoux, P., H. Schillinger, S. Niedermeier, M. Rodriguez, F. Ronneberger, R. Sauerbrey, B. Stein, D. Waite, C. Wedekind, H. Wille, L. Wöste, and C. Ziener: 'Remote sensing of the atmosphere using ultrashort laser pulses'. *Appl. Phys. B* (2000), vol. 71(4): pp. 573–580. DOI: 10.1007/s003400000375 (cit. on p. 3).

[Rey18] Reyes, D., M. Baudelet, M. Richardson, and S. Rostami Fairchild: 'Transition from linear- to nonlinear-focusing regime of laser filament plasma dynamics'. *J. Appl. Phys.* (2018), vol. 124(5): p. 053103. DOI: 10.1063/1.5027573 (cit. on pp. 22, 28, 29).

[Rho17] Rhodes, M., Z. Guang, J. Pease, and R. Trebino: 'Visualizing spatiotemporal pulse propagation: first-order spatiotemporal couplings in laser pulses'. *Appl. Opt.* (2017), vol. 56(11): pp. 3024–3034. DOI: 10.1364/AO.56.003024 (cit. on p. 42).

[Ros97] Ross, I. N., P. Matousek, M. Towrie, A. J. Langley, and J. L. Collier: 'The prospects for ultrashort pulse duration and ultrahigh intensity using optical parametric chirped pulse amplifiers'. *Opt. Commun.* (1997), vol. 144(1): pp. 125–133. DOI: 10.1016/S0030-4018(97)00399-4 (cit. on p. 1).

[Rot09] Rothhardt, J., S. Hädrich, T. Gottschall, T. Clausnitzer, J. Limpert, and A. Tünnermann: 'Compact fiber amplifier pumped OPCPA system delivering Gigawatt peak power 35 fs pulses'. *Opt. Express* (2009), vol. 17(26): pp. 24130–24136. DOI: 10.1364/OE.17.024130 (cit. on p. 1).

[Run98] Rundquist, A., C. G. Durfee, Z. Chang, C. Herne, S. Backus, M. M. Murnane, and H. C. Kapteyn: 'Phase-Matched Generation of Coherent Soft X-rays'. *Science* (1998), vol. 280(5368): pp. 1412–1415. doi: 10.1126/science.280.5368.1412 (cit. on p. 3).

[Sal97] Salières, P., A. L'Huillier, P. Antoine, and M. Lewenstein: 'Study of the spatial and temporal coherence of high order harmonics'. *arXiv e-prints* (1997), vol., quant-ph/9710060. doi: 10.48550/arXiv.quant-ph/9710060 (cit. on p. 3).

[Sch09] Schulz, E., T. Binhammer, D. S. Steingrube, S. Rausch, M. Kovacev, and U. Morgner: 'Intense few-cycle laser pulses from self-compression in a self-guiding filament'. *Appl. Phys. B* (2009), vol. 95(2): p. 269. doi: 10.1007/s00340-009-3456-5 (cit. on p. 87).

[Sch11a] Schulz, E., D. S. Steingrube, T. Binhammer, M. B. Gaarde, A. Couairon, U. Morgner, and M. Kovačev: 'Tracking spectral shapes and temporal dynamics along a femtosecond filament'. *Opt. Express* (2011), vol. 19(20): pp. 19495–19507. doi: 10.1364/OE.19.019495 (cit. on pp. 87, 88).

[Sch11b] Schulz, E., D. S. Steingrube, T. Vockerodt, T. Binhammer, U. Morgner, and M. Kovačev: 'Gradient enhanced third harmonic generation in a femtosecond filament'. *Opt. Lett.* (2011), vol. 36(22): pp. 4389–4391. doi: 10.1364/OL.36.004389 (cit. on p. 38).

[Sch12] Schulz, E.: 'Ultrakurze Laserpulse aus einem Filament'. PhD thesis. Leibniz Universität Hannover, 2012. doi: 10.15488/7973 (cit. on pp. 9, 11).

[Sch16] Schulte, J., T. Sartorius, J. Weitenberg, A. Vernaleken, and P. Russbueldt: 'Nonlinear pulse compression in a multi-pass cell'. *Opt. Lett.* (2016), vol. 41(19): pp. 4511–4514. doi: 10.1364/OL.41.004511 (cit. on p. 3).

[Sch99] Schillinger, H. and R. Sauerbrey: 'Electrical conductivity of long plasma channels in air generated by self-guided femtosecond laser pulses.' *Appl. Phys. B* (1999), vol. 68(4). doi: 10.1007/s003400050699 (cit. on p. 23).

[Sha77] Shapiro, S. L.: *Ultrashort Light Pulses - Picosecond Techniques and Applications*. First Edition. Springer-Verlag, Berlin/Heidelberg, 1977. doi: 10.1007/978-3-662-22574-5 (cit. on p. 50).

[She71] Shen, Y. R. and Michael M. T. Loy: 'Theoretical Interpretation of Small-Scale Filaments of Light Originating from Moving Focal Spots'. *Phys. Rev. A* (1971), vol. 3(6): pp. 2099–2105. doi: 10.1103/PhysRevA.3.2099 (cit. on p. 18).

[She84] Shen, Y. R.: *The Principles of Nonlinear Optics*. Wiley-Interscience, New York, 1984 (cit. on pp. 30, 31).

[She90] Shelton, D. P.: 'Nonlinear-optical susceptibilities of gases measured at 1064 and 1319 nm'. *Phys. Rev. A* (5 Sept. 1990), vol. 42: pp. 2578–2592. doi: 10.1103/PhysRevA.42.2578 (cit. on p. 99).

[Sil13] Silva, F., M. Miranda, S. Teichmann, M. Baudisch, M. Massicotte, F. Koppens, J. Biegert, and H. Crespo: 'Near to mid-IR ultra-broadband third harmonic generation in multilayer graphene: Few-cycle pulse measurement using THG dispersion-scan'. *CLEO: 2013*. 2013: pp. 1–2. doi: 10.1364/CLEO_SI.2013.CW1H.5 (cit. on p. 51).

[Sil17] Silva, F., I. J. Sola, H. Crespo, R. Romero, M. Miranda, C. L. Arnold, A. L'Huillier, J. Trull, and C. Cojocaru: 'Monolithic single-shot dispersion-scan: a new tool for real-time measurement and optimization of femtosecond pulses'. *CLEO/Europe-EQEC*. 2017: CF 11.3. doi: 10.1109/CLEOE-EQEC.2017.8086681 (cit. on p. 51).

[Sil19] Silva, C. L. da, R. G. Sonnenfeld, H. E. Edens, P. R. Krehbiel, M. G. Quick, and W. J. Koshak: 'The Plasma Nature of Lightning Channels and the Resulting Nonlinear Resistance'. *J. Geophys. Res.*

Atmos. (2019), vol. 124(16): pp. 9442–9463. DOI: 10.1029/2019JD030693 (cit. on p. 19).

[Sku06] Skupin, S., G. Stibenz, L. Bergé, F. Lederer, T. Sokollik, M. Schnürer, N. Zhavoronkov, and G. Steinmeyer: 'Self-compression by femtosecond pulse filamentation: Experiments versus numerical simulations'. *Phys. Rev. E* (2006), vol. 74(5): p. 056604. DOI: 10.1103/PhysRevE.74.056604 (cit. on pp. 33, 87).

[Sme12] Smetanina, E. O., A. E. Dormidonov, and V. P. Kandidov: 'Spatio-temporal evolution scenarios of femtosecond laser pulse filamentation in fused silica'. *Laser Phys.* (2012), vol. 22(7): pp. 1189–1198. DOI: 10.1134/S1054660X12070122 (cit. on p. 9).

[Smo00] Smolorz, S. and F. Wise: 'Femtosecond two-beam coupling energy transfer from Raman and electronic nonlinearities'. *J. Opt. Soc. Am. B* (Sept. 2000), vol. 17(9): pp. 1636–1644. DOI: 10.1364/JOSAB.17.001636 (cit. on p. 84).

[Ste09a] Steingrube, D. S., T. Vockerodt, E. Schulz, U. Morgner, and M. Kovačev: 'Phase matching of high-order harmonics in a semi-infinite gas cell'. *Phys. Rev. A* (2009), vol. 80(4): p. 043819. DOI: 10.1103/PhysRevA.80.043819 (cit. on p. 3).

[Ste09b] Steingrube, D. S., E. Schulz, T. Binhammer, T. Vockerodt, U. Morgner, and M. Kovačev: 'Generation of high-order harmonics with ultra-short pulses from filamentation'. *Opt. Express* (2009), vol. 17(18): pp. 16177–16182. DOI: 10.1364/OE.17.016177 (cit. on p. 35).

[Ste11a] Steingrube, D. S.: 'High-order harmonic generation with ultra-short pulses from filamentation'. PhD thesis. Leibniz Universität Hannover, 2011. DOI: 10.15488/7762 (cit. on pp. 8, 25, 35, 36).

[Ste11b] Steingrube, D. S., E. Schulz, T. Binhammer, M. B. Gaarde, A. Couairon, U. Morgner, and M. Kovačev: 'High-order harmonic generation directly from a filament'. *New J. Phys.* (2011), vol. 13(4):

p. 043022. DOI: 10.1088/1367-2630/13/4/043022 (cit. on pp. 3, 35, 36).

[Ste12] STEINGRUBE, D. S., M. KRETSCHMAR, D. HOFF, E. SCHULZ, T. BINHAMMER, P. HANSINGER, G. G. PAULUS, U. MORGNER, and M. KOVAČEV: 'Sub-1.5-cycle pulses from a single filament'. *Opt. Express* (2012), vol. 20(21): pp. 24049–24058. DOI: 10.1364/OE.20.024049 (cit. on pp. 3, 19, 36).

[Sti06] STIBENZ, G., N. ZHAVORONKOV, and G. STEINMEYER: 'Self-compression of millijoule pulses to 7.8 fs duration in a white-light filament'. *Opt. Lett.* (2006), vol. 31(2): pp. 274–276. DOI: 10.1364/OL.31.000274 (cit. on p. 87).

[Sto92] STOCK, G. and W. DOMCKE: 'Detection of ultrafast molecular-excited-state dynamics with time- and frequency-resolved pump-probe spectroscopy'. *Phys. Rev. A* (1992), vol. 45(5): pp. 3032–3040. DOI: 10.1103/PhysRevA.45.3032 (cit. on p. 1).

[Str85] STRICKLAND, D. and G. MOUROU: 'Compression of amplified chirped optical pulses'. *Opt. Commun.* (1985), vol. 55(6): pp. 447–449. DOI: 10.1016/0030-4018(85)90151-8 (cit. on p. 1).

[Sun09] SUNTSOV, S., D. ABDOLLAHPOUR, D. G. PAPAZOGLOU, and S. TZORTZAKIS: 'Efficient third-harmonic generation through tailored IR femtosecond laser pulse filamentation in air'. *Opt. Express* (2009), vol. 17(5): pp. 3190–3195. DOI: 10.1364/OE.17.003190 (cit. on pp. 3, 4, 38, 59, 60, 83).

[Sun10] SUNTSOV, S., D. ABDOLLAHPOUR, D. G. PAPAZOGLOU, and S. TZORTZAKIS: 'Filamentation-induced third-harmonic generation in air via plasma-enhanced third-order susceptibility'. *Phys. Rev. A* (2010), vol. 81(3): p. 033817. DOI: 10.1103/PhysRevA.81.033817 (cit. on pp. 4, 38, 59, 83, 85).

[Swe97] SWEETSER, J. N., D. N. FITTINGHOFF, and R. TREBINO: 'Transient-grating frequency-resolved optical gating'. *Opt. Lett.* (1997), vol. 22(8): pp. 519–521. DOI: 10.1364/OL.22.000519 (cit. on p. 51).

[Syt21] Sytcevich, I., C. Guo, S. Mikaelsson, J. Vogelsang, A.-L. Viotti, B. Alonso, R. Romero, P. T. Guerreiro, Í. J. Sola, A. L'Huillier, H. Crespo, M. Miranda, and C. L. Arnold: 'Characterizing ultrashort laser pulses with second harmonic dispersion scans'. *J. Opt. Soc. Am. B* (2021), vol. 38(5): pp. 1546–1555. doi: 10.1364/JOSAB.412535 (cit. on p. 50).

[Taj16] Tajalli, A., B. Chanteau, M. Kretschmar, H. G. Kurz, D. Zuber, M. Kovacev, U. Morgner, and T. Nagy: 'Few-cycle optical pulse characterization via cross-polarized wave generation dispersion scan technique'. *Opt. Lett.* (2016), vol. 41(22): pp. 5246–5249. doi: 10.1364/OL.41.005246 (cit. on p. 51).

[Taj79] Tajima, T. and J. M. Dawson: 'Laser Electron Accelerator'. *Phys. Rev. Lett.* (1979), vol. 43(4): pp. 267–270. doi: 10.1103/PhysRevLett.43.267 (cit. on p. 2).

[Tak02] Takahashi, E., Y. Nabekawa, T. Otsuka, M. Obara, and K. Midorikawa: 'Generation of highly coherent submicrojoule soft x rays by high-order harmonics'. *Phys. Rev. A* (2002), vol. 66(2): p. 021802. doi: 10.1103/PhysRevA.66.021802 (cit. on p. 3).

[Tak06] Takada, H. and K. Torizuka: 'Design and construction of a TW-class 12-fs Ti:Sapphire chirped-pulse amplification system'. *IEEE J. Sel. Top. Quantum Electron.* (2006), vol. 12(2): pp. 201–212. doi: 10.1109/JSTQE.2006.871958 (cit. on p. 1).

[Thé05] Théberge, F., N. Aközbek, W. Liu, J.-F. Gravel, and S.L. Chin: 'Third harmonic beam profile generated in atmospheric air using femtosecond laser pulses'. *Opt. Commun.* (2005), vol. 245(1): pp. 399–405. doi: 10.1016/j.optcom.2004.10.020 (cit. on pp. 37, 38).

[Thé06] Théberge, F., W. Liu, P. Tr. Simard, A. Becker, and S. L. Chin: 'Plasma density inside a femtosecond laser filament in air: Strong dependence on external focusing'. *Phys. Rev. E* (2006), vol. 74(3): p. 036406. doi: 10.1103/PhysRevE.74.036406 (cit. on pp. 9, 74).

[Thé08] Théberge, F., M. Châteauneuf, V. Ross, P. Mathieu, and J. Dubois: 'Ultrabroadband conical emission generated from the ultraviolet up to the far-infrared during the optical filamentation in air'. *Opt. Lett.* (2008), vol. 33(21): pp. 2515–2517. doi: 10.1364/OL.33.002515 (cit. on p. 11).

[Toc19] Tochitsky, S., E. Welch, M. Polyanskiy, I. Pogorelsky, P. Panagiotopoulos, M. Kolesik, E. M. Wright, S. W. Koch, J. V. Moloney, J. Pigeon, and C. Joshi: 'Megafilament in air formed by self-guided terawatt long-wavelength infrared laser'. *Nat. Photonics* (2019), vol. 13(1): pp. 41–46. doi: 10.1038/s41566-018-0315-0 (cit. on p. 8).

[Tra03] Di Trapani, P., G. Valiulis, A. Piskarskas, O. Jedrkiewicz, J. Trull, C. Conti, and S. Trillo: 'Spontaneously Generated X-Shaped Light Bullets'. *Phys. Rev. Lett.* (2003), vol. 91(9): p. 093904. doi: 10.1103/PhysRevLett.91.093904 (cit. on p. 11).

[Tre00] Trebino, R.: *Frequency-Resolved Optical Gating: The Measurement of Ultrashort Laser Pulses*. First Edition. Kluwer Academic, Boston, MA, 2000. doi: 10.1007/978-1-4615-1181-6 (cit. on p. 51).

[Tre93] Trebino, R. and D. J. Kane: 'Using phase retrieval to measure the intensity and phase of ultrashort pulses: frequency-resolved optical gating'. *J. Opt. Soc. Am. A* (1993), vol. 10(5): pp. 1101–1111. doi: 10.1364/JOSAA.10.001101 (cit. on p. 51).

[Tre97] Trebino, R., K. W. DeLong, D. N. Fittinghoff, J. N. Sweetser, M. A. Krumbügel, B. A. Richman, and D. J. Kane: 'Measuring ultrashort laser pulses in the time-frequency domain using frequency-resolved optical gating'. *Rev. Sci. Instrum.* (1997), vol. 68(9): pp. 3277–3295. doi: 10.1063/1.1148286 (cit. on p. 50).

[Tsa96] Tsang, T., M. A. Krumbügel, K. W. DeLong, D. N. Fittinghoff, and R. Trebino: 'Frequency-resolved optical-gating measurements of ultrashort pulses using surface third-harmonic generation'. *Opt. Lett.*

(1996), vol. 21(17): pp. 1381–1383. DOI: 10.1364/OL.21.001381 (cit. on p. 51).

[Tur16] TURNBULL, D., P. MICHEL, T. CHAPMAN, E. TUBMAN, B. B. POLLOCK, C. Y. CHEN, C. GOYON, J. S. ROSS, L. DIVOL, N. WOOLSEY, and J. D. MOODY: 'High Power Dynamic Polarization Control Using Plasma Photonics'. *Phys. Rev. Lett.* (2016), vol. 116(20): p. 205001. DOI: 10.1103/PhysRevLett.116.205001 (cit. on p. 2).

[Tzo01a] TZORTZAKIS, S., B. LAMOUROUX, A. CHIRON, S.D. MOUSTAIZIS, D. ANGLOS, M. FRANCO, B. PRADE, and A. MYSYROWICZ: 'Femtosecond and picosecond ultraviolet laser filaments in air: experiments and simulations'. *Opt. Commun.* (2001), vol. 197(1): pp. 131–143. DOI: 10.1016/S0030-4018(01)01443-2 (cit. on p. 87).

[Tzo01b] TZORTZAKIS, S., B. PRADE, M. FRANCO, A. MYSYROWICZ, S. HÜLLER, and P. MORA: 'Femtosecond laser-guided electric discharge in air'. *Phys. Rev. E* (2001), vol. 64(5): p. 057401. DOI: 10.1103/PhysRevE.64.057401 (cit. on p. 3).

[Tzo01c] TZORTZAKIS, S., L. SUDRIE, M. FRANCO, B. PRADE, A. MYSYROWICZ, A. COUAIRON, and L. BERGÉ: 'Self-Guided Propagation of Ultrashort IR Laser Pulses in Fused Silica'. *Phys. Rev. Lett.* (2001), vol. 87(21): p. 213902. DOI: 10.1103/PhysRevLett.87.213902 (cit. on p. 9).

[Tzo99] TZORTZAKIS, S., M. A. FRANCO, Y.-B. ANDRÉ, A. CHIRON, B. LAMOUROUX, B. S. PRADE, and A. MYSYROWICZ: 'Formation of a conducting channel in air by self-guided femtosecond laser pulses'. *Phys. Rev. E* (1999), vol. 60(4): R3505–R3507. DOI: 10.1103/PhysRevE.60.R3505 (cit. on p. 23).

[Voc12] VOCKERODT, T., D. S. STEINGRUBE, E. SCHULZ, M. KRETSCHMAR, U. MORGNER, and M. KOVAČEV: 'Low- and high-order harmonic generation inside an air filament'. *Appl. Phys. B* (2012), vol. 106(3): pp. 529–532. DOI: 10.1007/s00340-011-4858-8 (cit. on p. 35).

[Wah12] Wahlstrand, J. K., Y.-H. Cheng, and H. M. Milchberg: 'Absolute measurement of the transient optical nonlinearity in N_2, O_2, N_2O, and Ar'. *Phys. Rev. A* (2012), vol. 85(4): p. 043820. doi: 10.1103/PhysRevA.85.043820 (cit. on p. 20).

[Wah13] Wahlstrand, J. K., J. H. Odhner, E. T. McCole, Y.-H. Cheng, J. P. Palastro, R. J. Levis, and H. M. Milchberg: 'Effect of two-beam coupling in strong-field optical pump-probe experiments'. *Phys. Rev. A* (2013), vol. 87(5): p. 053801. doi: 10.1103/PhysRevA.87.053801 (cit. on p. 84).

[Wil20] Wills, S.: 'ELI: Open for Business'. *Opt. Photon. News* (2020), vol. 31(1): pp. 30–37. doi: 10.1364/OPN.31.1.000030 (cit. on p. 1).

[Xi09] Xi, T.-T., X. Lu, and J. Zhang: 'Enhancement of third harmonic emission by interaction of two colored filament with droplet in air'. *Opt. Commun.* (2009), vol. 282(15): pp. 3140–3143. doi: 10.1016/j.optcom.2009.04.038 (cit. on pp. 38, 39).

[Xin93] Xing, Q., K. M. Yoo, and R. R. Alfano: 'Conical emission by four-photon parametric generation by using femtosecond laser pulses'. *Appl. Opt.* (1993), vol. 32(12): pp. 2087–2089. doi: 10.1364/AO.32.002087 (cit. on p. 11).

[Xu06] Xu, B., Y. Coello, V. V. Lozovoy, D. Ahmasi Harris, and M. Dantus: 'Pulse shaping of octave spanning femtosecond laser pulses'. *Opt. Express* (2006), vol. 14(22): pp. 10939–10944. doi: 10.1364/OE.14.010939 (cit. on p. 50).

[Yam02] Yamanouchi, K.: 'The Next Frontier'. *Science* (2002), vol. 295(5560): pp. 1659–1660. doi: 10.1126/science.1068449 (cit. on p. 1).

[Yam11] Yamanouchi, K.: *Lectures on Ultrafast Intense Laser Science 1*. First Edition. Springer-Verlag, Berlin/Heidelberg, 2011. doi: 10.1007/978-3-540-95944-1 (cit. on p. 74).

[Yao12] Yao, J., B. Zeng, W. Chu, J. Ni, and Y. Cheng: 'Enhancement of third harmonic generation in femtosecond laser induced filamentation – comparison of results obtained with plasma and a pair of glass plates'. *J. Mod. Opt.* (2012), vol. 59(3): pp. 245–249. doi: 10.1080/09500340.2011.624202 (cit. on pp. 38, 60, 83).

[Yua13] Yuan, S., T. Wang, Y. Teranishi, A. Sridharan, S. Hsien Lin, H. Zeng, and S. L. Chin: 'Lasing action in water vapor induced by ultrashort laser filamentation'. *Applied Physics Letters* (2013), vol. 102(22): p. 224102. doi: 10.1063/1.4809585 (cit. on pp. 3, 8).

[Zaï07] Zaïr, A., A. Guandalini, F. Schapper, M. Holler, J. Biegert, L. Gallmann, A. Couairon, M. Franco, A. Mysyrowicz, and U. Keller: 'Spatio-temporal characterization of few-cycle pulses obtained by filamentation'. *Opt. Express* (2007), vol. 15(9): pp. 5394–5405. doi: 10.1364/OE.15.005394 (cit. on p. 35).

[Zew00] Zewail, A. H.: 'Femtochemistry: Atomic-Scale Dynamics of the Chemical Bond'. *J. Phys. Chem. A* (2000), vol. 104(24): pp. 5660–5694. doi: 10.1021/jp001460h (cit. on p. 1).

[Zha09] Zhan, Q.: 'Cylindrical vector beams: from mathematical concepts to applications'. *Adv. Opt. Photon.* (2009), vol. 1(1): pp. 1–57. doi: 10.1364/AOP.1.000001 (cit. on p. 120).

[Zha10] Zhang, Z., X. Lu, Y. Zhang, M. Zhou, T. Xi, Z. Wang, and J. Zhang: 'Enhancement of third-harmonic emission from femtosecond laser filament screened partially by a thin fiber'. *Opt. Lett.* (2010), vol. 35(7): pp. 974–976. doi: 10.1364/OL.35.000974 (cit. on pp. 38, 39).

[Zho14] Zhokhov, P. A. and A. M. Zheltikov: 'Scaling laws for laser-induced filamentation'. *Phys. Rev. A* (4 Apr. 2014), vol. 89: p. 043816. doi: 10.1103/PhysRevA.89.043816 (cit. on p. 13).

A Parameter study

In this appendix, the complementary figures of the parameter study of Sec. 3.2.1 for the parameters pulse energy, polarization, and pulse duration are shown. These particular figures were not implemented into Sec. 3.2.1, as the respective parameter scans showed no significant influence on the temporal plasma evolution illustrated in them.

A.1 Pulse energy

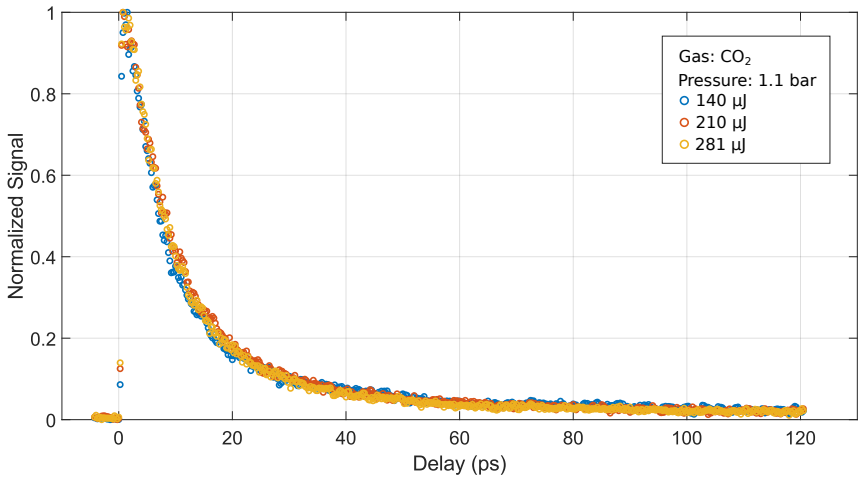

Figure A.1: Normalized temporal TH evolution signal for different pump pulse energies in carbon dioxide measured at 1.1 bar.

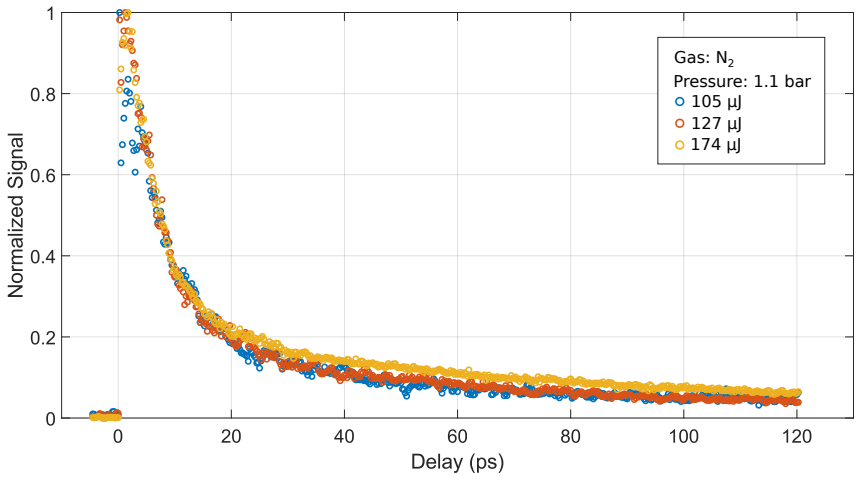

Figure A.2: Normalized temporal TH evolution signal for different pump pulse energies in nitrogen measured at 1.1 bar.

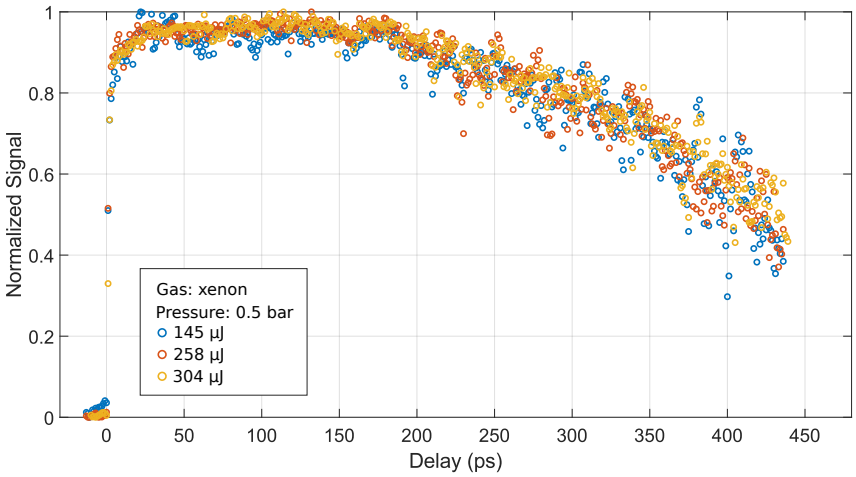

Figure A.3: Normalized temporal TH evolution signal for different pump pulse energies in xenon measured at 0.5 bar.

A.2 Polarization

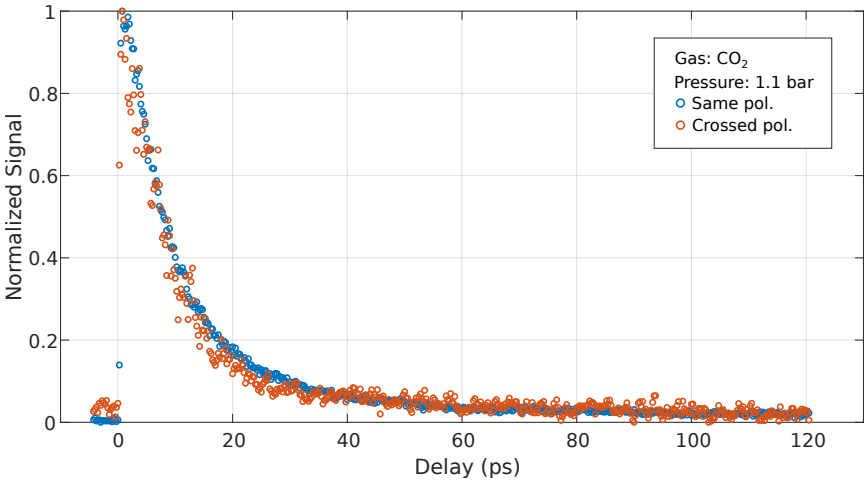

Figure A.4: Normalized temporal TH evolution signal for different pump beam polarization states with respect to the probe beam in carbon dioxide measured at 1.1 bar.

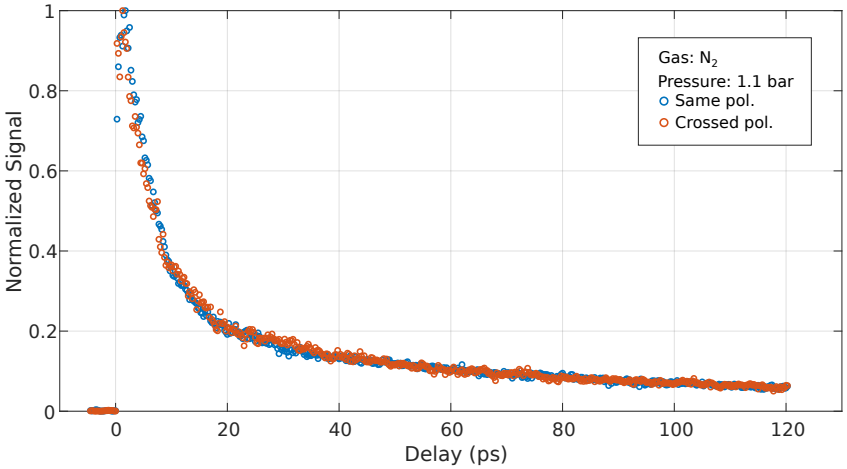

Figure A.5: Normalized temporal TH evolution signal for different pump beam polarization states with respect to the probe beam in nitrogen measured at 1.1 bar.

A.3 Pulse duration

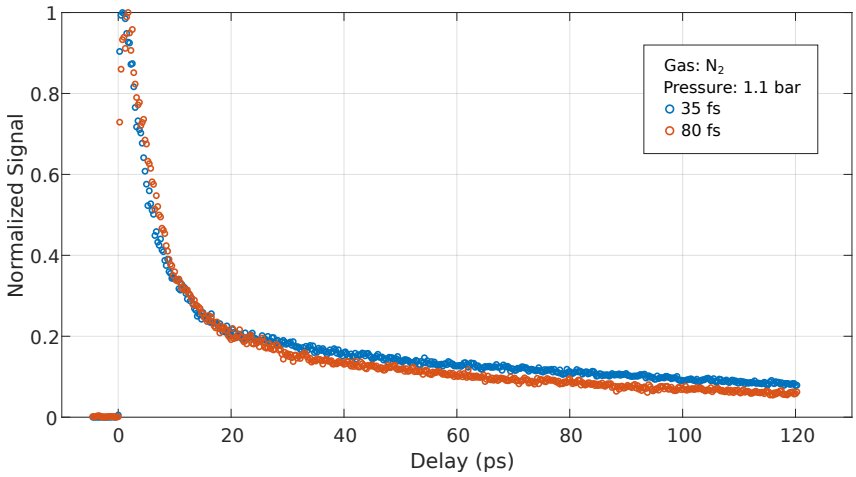

Figure A.6: Normalized temporal TH evolution signal for different pump pulse durations in nitrogen measured at 1.1 bar. The traces are normalized to the maxima of the signals.

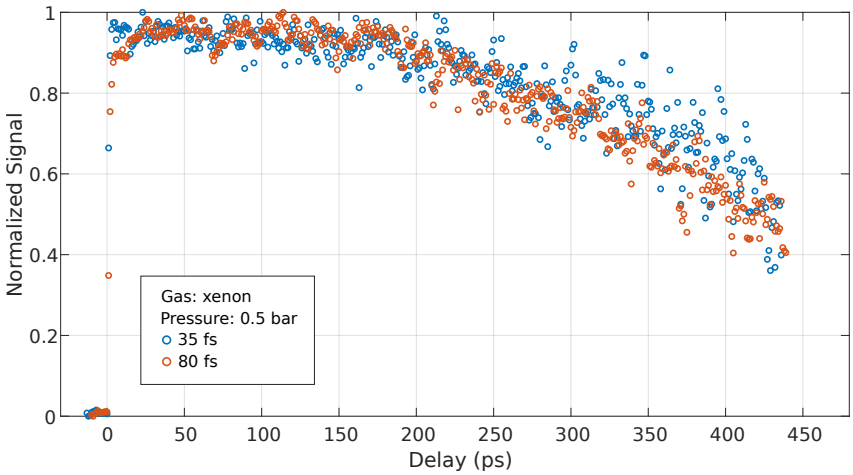

Figure A.7: Normalized temporal TH evolution signal for different pump pulse durations in xenon measured at 0.5 bar. The traces are normalized to the maxima of the signals.

Publications

Scientific publications

1. **Jusko, C.**, A. Sridhar, E. Appi, L. Shi, U. Morgner, and M. Kovacev: 'Filamentation-assisted plasma lifetime measurements in atomic and molecular gases via third-harmonic enhancement'. *Journal of the Optical Society of America B* (2019), vol. 36(12): pp. 3505–3513. doi: 10.1364/JOSAB.36.003505.

2. Appi, E., C. C. Papadopoulou, J. L. Mapa, N. Wesavkar, **C. Jusko**, P. Mosel, S. Ališauskas, T. Lang, C. M. Heyl, B. Manschwetus, M. Brachmanski, M. Braune, H. Lindenblatt, F. Trost, S. Meister, P. Schoch, R. Treusch, R. Moshammer, I. Hartl, U. Morgner, and M. Kovacev: 'A synchronized VUV light source based on high-order harmonic generation at FLASH'. *Scientific Reports* (2020), vol. 10(1): p. 6867. doi: 10.1038/s41598-020-63019-2.

3. Appi, E., C. C. Papadopoulou, J. L. Mapa, **C. Jusko**, P. Mosel, A. Schoenberg, J. Stock, T. Feigl, S. Ališauskas, T. Lang, C. M. Heyl, B. Manschwetus, M. Brachmanski, M. Braune, H. Lindenblatt, F. Trost, S. Meister, P. Schoch, A. Trabattoni, F. Calegari, R. Treusch, R. Moshammer, I. Hartl, U. Morgner, and M. Kovacev: 'Synchronized beamline at FLASH2 based on high-order harmonic generation for two-color dynamics studies'. *Review of Scientific Instruments* (2021), vol. 92(12): p. 123004. doi: 10.1063/5.0063225.

4. Neoričić, L., **C. Jusko**, S. Mikaelsson, C. Guo, M. Miranda, S. Zhong, F. Garmirian, B. Major, J. M. Brown, M. B. Gaarde, A. Couairon, U. Morgner, M. Kovačev, and C. L. Arnold: '4D spatio-temporal electric field characterization of ultrashort light pulses undergoing filamentation'. *Optics Express* (2022), vol. 30(15): pp. 27938–27950. doi: 10.1364/OE.461388.

Submissions to international conferences

1. **Jusko, C.**, L. Shi, A. Sridhar, E. Appi, U. Morgner, and M. Kovacev: 'Filamentation-Based Transient Dynamic Studies via Third-Harmonic Generation in Gases'. *2019 Conference on Lasers and Electro-Optics Europe European Quantum Electronics Conference (CLEO/Europe-EQEC)*. 2019: pp. 1–1. DOI: 10.1109/CLEOE-EQEC.2019.8873191.

2. Appi, E., C. C. Papadopoulou, J. Mapa, N. Wesavkar, **C. Jusko**, P. Mosel, S. Alisauskas, T. Lang, C. M. Heyl, B. Manschwetus, M. Braune, M. Brachmanski, H. Lindenblatt, F. Trost, S. Meister, P. Schoch, R. Treusch, R. Moshammer, I. Hartl, U. Morgner, and M. Kovacev: 'A synchronized VUV beamline for time domain two-color dynamic studies at FLASH2'. *Conference on Lasers and Electro-Optics*. Optical Society of America, 2020: FW4D.2. DOI: 10.1364/CLEO_QELS.2020.FW4D.2.

3. Appi, E., C. C. Papadopoulou, J. Mapa, N. Wesavkar, **C. Jusko**, P. Mosel, S. Alisauskas, T. Lang, C. M. Heyl, B. Manschwetus, M. Braune, M. Brachmanski, H. Lindenblatt, F. Trost, S. Meister, P. Schoch, R. Treusch, R. Moshammer, I. Hartl, U. Morgner, and M. Kovacev: 'Synchronized HHG based source at FLASH'. *OSA High-brightness Sources and Light-driven Interactions Congress 2020 (EUVXRAY, HILAS, MICS)*. Optical Society of America, 2020: HTh1B.3. DOI: 10.1364/HILAS.2020.HTh1B.3.

4. **Jusko, C.**, L. Neoričić, S. Mikaelsson, F. Garmirian, C. Guo, S. Zhong, B. Major, M. Miranda, U. Morgner, A. L'Huillier, A. Couairon, M. Kovačev, and C. L. Arnold: 'Spatio-temporal characterization of a femtosecond filament along its length'. *OSA High-brightness Sources and Light-driven Interactions Congress 2020 (EUVXRAY, HILAS, MICS)*. Optical Society of America, 2020: HM1B.4. DOI: 10.1364/HILAS.2020.HM1B.4.

5. **Jusko, C.**, A. Sridhar, E. Appi, L. Shi, U. Morgner, and M. Kovacev: 'Femtosecond laser-induced plasma evolution studies via third-harmonic enhancement in atomic and molecular gases'. *OSA High-brightness Sources and Light-driven Interactions Congress 2020 (EUVXRAY, HILAS, MICS)*. Optical Society of America, 2020: JW1A.15. DOI: 10.1364/EUVXRAY.2020.JW1A.15.

Acknowledgments

Here and now, and in my opinion way too late in this thesis, I want to thank all the people, who helped and supported so much during my PhD. “PhD”, three letters for experiences that could fill books. Trying to summarize this time in a little bit more than one page by expressing my gratitude to you all seems impossible but let me try.

Special thanks go to Milutin Kovačev for being my supervisor, who always encouraged me to go on and to tackle any issue on the way. I really appreciate your confidence in me for always finding a solution. My deep gratitude goes to both Milutin Kovačev and Uwe Morgner for giving me the opportunity to work on my project and for always welcoming me in their group since my bachelor time! At this point I also have to express my thanks to Cord Arnold for all the great assistance and support in finishing the analysis for our Lund-Hannover project despite living in two different countries and a worldwide pandemic taking place. Thank you to both of you, Milutin and Cord, for giving me this wonderful opportunity to perform a part of my research in Lund. I really appreciated my time there!

Big thanks also go to Lana Neoričić, for our congenial cooperation in performing all the measurements for the Lund-Hannover project and our countless great conversations about the project and so much more. We shared the effort and now we can also share the great outcome!

I am truly thankful for the super nice and inspiring atmosphere provided by all members of AG Morgner over my time in the group. I am more than happy to have been a part of you! Robin, keep going with your astrophotography projects! Limitless thanks go to the people from “downstairs labs”, to José Louise Mapa for great conversations about everything and above all to Philip Mosel and Elisa Appi. Some people would be happy if they tamed a dragon once in their lifetime. We sometimes tamed a dragon multiple times a day among other tasks and thought it

would be the most normal thing to do. Simply and truly thank you for the great time! Elisa, you deserve way more credit than I can possibly give you here. You have been the best lab buddy of the world! Thank you for your indescribable support over all these years from the beginning till the end. Mille grazie, my friend!

My deepest and greatest gratitude goes to my friends and family, who always supported and accompanied through all the ups and downs of these past years. You motivated me to always keep going. Thank you Laura, Tobi and Marcus for all the great distraction from work. You are the best! Immeasurable thanks go to my family. Mama, Papa, Thomas, Steffen, Oma und Opa, diese Arbeit ist auch eure Arbeit! Danke für alles!

My final credit is reserved for you, Christine. Thank you for your unlimited support and encouragement. I cannot express how happy I am to know you.

Danke schön!